MODELING OF INTERRILL SEDIMENT GENERATION AND SOIL MICROTOPOGRAPHY DYNAMICS UNDER VARIABLE SIMULATED RAINFALL EROSIVITY

(降雨侵食による微地形動態とインターリル土壌堆積のモデル化)

Thesis

By

MOHAMED ABD ELBASIT MOHAMED AHMED

Submitted to the United Graduate School of Agricultural Sciences, Tottori University in partial fulfillment of the requirements for the degree of Doctor of Philosophy in Bio-environmental Sciences

March, 2009

DEDICATION

I would like to dedicate this humble thesis to:

My beloved wife Marreia El Amin Ugool and my daughter Hibatallah

My family: Abd Elbasit, Widad, Rasha, Rau'a, Raghda, Ahmed, and Yaseen

For their generous love and support

ABSTRACT

Deformation of soil surface due to raindrop impact involve several processes have not yet been well understood. This study was attempted to measure, evaluate, and model two important processes: (1) soil microtopography change and (2) soil particle detachment due to raindrop impact. In order to understand these processes, robust techniques must be used to quantify each factor affects these two processes.

Firstly, the potential use of a piezoelectric transducer to measure the rainfall impact energy under simulated rainfall conditions was investigated. The simulated rainfall kinetic energy (*KE*) and drop size distribution (*DSD*) were measured using piezoelectric transducers, modified from the Vaisala RAINCAP® rainfall sensor. The direct measurement of the kinetic energy was significantly correlated with the estimated kinetic energy using the drop size distribution data and empirical fall velocity relationships ($r > 0.84$, $P=0.005$). The effect of the rainfall characteristics produced by dripper-type rainfall simulator on splash soil erosion (D_s) was also assessed. The relationship between the rainfall intensity (*I*) and *KE* was found to be different from natural rainfall and the *I*-D_s relationship followed the same trend. This result emphasizes the importance of the *I-KE* relationship in determination of the *I*-D_s relationship, which can differ from one rainfall simulator to another. Accordingly, to improve the soil splash estimation by simulated rainfall the characteristics of the simulated rainfall have to be taken into account.

Secondly, the potential consumer-grade cameras and close-range photogrammetry procedures to quantify soil microtopography at plot-scale level (≤ 1 m^2) were assessed using simulated soil surface. The surfaces' digital elevation model (*DEM*) was generated using the photogrammetry system (*PHM*) involving a consumer-grade camera, and pin-microrelief meter (*PM*). The *DEM* generated using the *PHM* was assessed for accuracy, roughness indices, depression area percentage, depression storage capacity, and micro-rills delineation in comparison with the *PM*. Our results suggest that a consumer-grade camera and close-range photogrammetry have high potential to quantify the soil microtopography. The method was also assessed to quantify the soil microtopography changes during rainfall. A reference surface rectification method (*RSM*) was developed to detect and eliminate the *DEM* errors prior to interpolation. The second method used was the parametric statistical method (*PSM*), which was used to detect and rectify the *DEM* errors after interpolation. The automated digital photogrammetric system with the rectification methods accurately generated three dimensional (*3D*) visions of the soil microtopography during rainfall.

Thirdly, two modeling approaches, empirical and physically-based, were assessed to evaluate the capability of each approach to estimate the sediment yield under hillslope condition. The empirical models tested in this study used a combination of factors which influence the sediment yield, particularly rainfall intensity, slope and runoff. The physically-based model on the other hand, used the kinematic wave method to estimate runoff and the sediment mass balance equation to estimate the sediment yield. A comparison between the empirical models and the physically-based model showed that the physically-based model, which uses the measurable soil parameters such as bulk density and hydraulic conductivity, estimates the sediment yield and runoff effectively.

ACKNOWLEDGEMENTS

First and foremost, I thank ALLAH the almighty for giving me a power, support, patience and people's help to pursue this study.

"He who does not thank people does not thank Allah"

I would like to express my gratitude to all those who gave me the moral and actual possibility to complete this study, and they are so many.

I am deeply indebted to the Government of Japan, Ministry of Education, Culture, Sports, Science, and Technology (MEXT) for their financial support of my PhD study in Japan; and also I would like to thank the Ministry of Science and Technology (MOST), The National Center for Research (NCR), Sudan for their encouragement during my long study period.

It is difficult for me to find words suitable to express my deep gratitude to my PhD major supervisor Prof. Dr. Hisao Anyoji, Water Resources Laboratory, Arid Land Research Center, Tottori University for his generous support, inspiration, and encouragement.

Also, it is difficult to express my appreciation to my PhD first co-supervisor Associate Prof. Dr. Hiroshi Yasuda, Water Resources Laboratory, Arid Land Research Center, Tottori University for his guidance, help, enthusiasm, and comments.

I would like also to thank my co-supervisor Emirate Prof. Dr. Soichi Nishiyama, Faculty of Agriculture, Yamaguchi University for his great help and comments; and I will never forget his advice: "Mohamed san; discuss before experiment; discussion after experiment is useless".

Also, I appreciate the deep discussion, great encouragement, and nice comments of my co-supervisor Prof. Dr. Mitsuo Fukoda, Faculty of Agriculture, Yamaguchi University, although we met for short time.

I would like to express my sincere gratitude to my applied physics advisor Mr. Atte salmi, Vaisala Oyj, Helsinki, Finland, who taught me how to listen to raindrops and understand their codes; I really appreciate his help, support, and comments. It is a pleasure here to thank Mr. Salmi who supports my PhD's research by providing two piezoelectric transducers used for the rainfall characterization (erosivity) studies.

I am indebted to many people and administrations in Tottori University; I would like to thank the academic, technical, and administrational staff of the Arid land Research Center, staff of Tottori University Library, staff of the Graduate School, and staff of the International Student Affair.

I am grateful to Prof. Dr. Ahmed E. Osman, visiting professor at the Arid Land Research Center; Associate Prof. Dr. Reiji Kimura and Associate Prof. Dr. Mitsuru Tsubu, and Prof. Dr. Mitsuhiro Inoue Arid Land Research Center; Prof. Dr. Velu Rasiah, Department of Natural Resources and Mines, Queensland Government, Australia for their immense help and advice.

Also, I would like to express my thanks to Dr. Ghazi H. Badawi, University of Khartoum, Sudan and Dr. Esamedeen E. Elgorashi, University of Pretoria, South Africa for their generous help and encouragement.

I wish to thank Prof. Dr. Mohan Saxana, Prof. Dr. Thomas Richard and Dr. Izzat Tahir, visiting professors at the Arid Land Research Center; and Dr. Elsadig A. Elhadi, the National Center for Research, Desertification Research Institute, Sudan for their editorial help in manuscripts and their valuable comments.

I would like to thank the entire current and past members of the Water Resources Laboratory, and friends in Tottori University, Japan, and Sudan who supported me in various ways.

I owe my loving thanks to my father (Abd Elbasit Mohamed Ahmed) and my mother (Widad Atta). They raised me, helped me, encouraged me, loved me, and I am sure they prayed to ALLAH the almighty for me.

Lastly, and most importantly, I would like to give my special thanks to my beloved wife Marreia Elamin Ugool whose patient love, support, help, discussion and encouragements enabled me to do this work and also for her real contribution in data entering and exploration analysis, and her help in rainfall simulator experiments.

My sweet thanks to my little daughter (Hibatallah) who her chaos was enlightened my mind and arranged my ideas; many thanks to Allah's "Hiba" for her lovely signature on most of my documents, when ever she get a chance.

Finally, despite the generous guidance and immense assistance from all above mentioned, errors and misconception, if any, are solely fall under my responsibility.

TABLE OF CONTENTS

CHAPTER 6

CHAPTER 7

LIST OF FIGURES

LIST OF TABLES

CHAPTER 1:
General Introduction

1.1. Introduction

World human population has been estimated to approach 8 billions by 2020 (UNPD, 2004). The annual peak increase rate for the population was achieved in 1963 which was more than two percent of the total population. On the other hand, there is no increase in the natural resources which are securing food and fiber for the mankind. Moreover, human still lose the productivity of these resources due to different causes of "land degradation". Land degradation is defined as: the temporary or permanent lowering of the productivity of land (UNEP, 1992). The land degradation can be classified in six major types are: soil water erosion, wind erosion, soil fertility decline, salinization, waterlogging , and deterioration of the ground water (FAO, 1994). Within these types, soil water erosion alone had accounted for about 55% of the degraded soils worldwide (El-Swaify, 1994). The soil water erosion has been divided into interrill, rill, and gully soil erosion (Laflen and Roose, 1998). The main reason behind this demarcation is to make the mathematical modeling easier than the lumped condition.

The interrill soil erosion represents the first stage of the soil erosion processes, which occur with the first raindrop strike the soil surface. Also, this type of soil erosion is the main source for sediment generation. The main processes involve during the interrill soil erosion are the detachment of soil particles by the raindrop impact energy and the transport by very shallow water flow. Because of these dominant processes at the interrill areas, the interrill soil erosion can be considered as a sediment generation stage more than soil loss stage (soil erosion). Sediment is the eroded soil which reduces the storage capacities of reservoirs and carrying capacities of natural and artificial waterways, and it also carries the absorbed pollutants (chemicals, nutrients, pesticides, and heavy metals) (Ghadiri and rose, 1992). The generated sediment has several environmental impacts which can be considered "in-site" on the land health and productivity and "off-site" on the streams and water bodies. The rate of the interrill sediment generation remains constant over a slope under constant soil surface properties (Young and Wiersma, 1973). However, under any circumstances the soil surface properties are not constant. The major factors that affect the interrill sediment generation rate are the rainfall intensity (rainfall erosivity), and interrill flow rate. These

two factors are adjusted for different soil surface factors including the interrill slope angle, soil type and cover, sealing formation, soil microtopography, etc. These factors are used as interrill sediment generation drivers in several models in order to estimate the amount of sediment that will be delivered to rills or directly to streams and water bodies. The main reason of constructing models is to enhance the communication between human and natural life processes. There are several types of models used to estimate the interrill sediment generation. The factors-multiplication model type was developed earlier by Zingg (1940) to study the effect of slope angle and length on soil erosion. The most widely used soil erosion model is the Universal Soil Loss Equation (USLE) (Wischmeier and Smith, 1965). However, the USLE does not discriminate clearly between the interrill and rill sediment generation in its calculation.

1. 2. Interrill sediment generation

The process of soil erosion by water starts with the detachment and transport of soil particles by impact force of raindrops and drag force of overland flow (Ellison, 1947). The soil water erosion process can be detachment limited (low rainfall impact energy or high soil strength) or transport limited (Foster, 1982). The general definition of the interrill soil erosion is the erosion that occurs at the area between the rills. However, for better understand of this definition, the domain of the rill erosion must be elaborated. Rill erosion occurs when the overland flow tends to concentrate in numerous small channels (Sharma, 1996). The rill can be defined as continuous depressions of the sloping lands where the water concentrate and travel downslope. Usually the rill can be generated by two processes; erosion or tillage. In this regard, any erosion occurred due to the flow of water in these channels is called rill erosion.

1. 2.1. Processes of interrill erosion

The major processes that work in the interrill area are four; 1) detachment by raindrop, 2) detachment by water flow, 3) transport by raindrop, and 4) transport by water flow (Ellison, 1947; Rowlison and Martin, 1971). However, raindrop-induce detachment and flow transport are the two dominant processes (Sharma, 1996). These processes were well compiled in the conceptual water erosion model of Meyer and Wischmeier (1969). This model is the base for the rill and interrill erosion models **(Fig. 1.1)**. Kinnell (2005) has also classified the erosion processes in four categories based on the mechanism of the detachment and transport of the soil particles. These four

categories can be lumped together to describe the interrill soil erosion processes which are called the "raindrop-impact-induce erosion" (*RIIE*). The *RIIE* is the rainfall erosion resulted from the expenditure of falling raindrop and flowing water when these two agents either act singly or together (Kinnell, 2005). The *RIIE* is the major detachment agent in interrill and sheet erosion. Within the *RIIE*, four categories of detachments and transport mechanism have been identified (**Fig. 1.2**):

1) Rainfall detachment with transport by raindrop splash (*RD-ST*).

2) Raindrop detachment with transport by raindrop-induced flow transport (*RD-RIFT*)

3) Raindrop detachment with transport by flow (*RD-FT*)

4) Flow detachment with transport by flow (*FD-FT*)

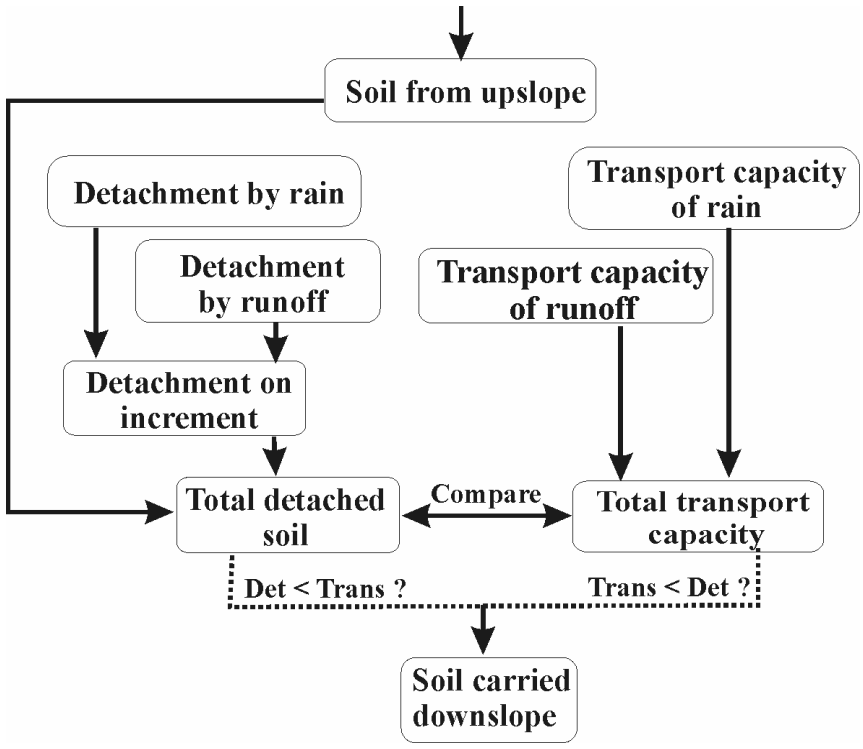

Fig. 1.1. Conceptual water erosion model of Meyer and Wischmeier (1969) (From: Sharma (1996)).

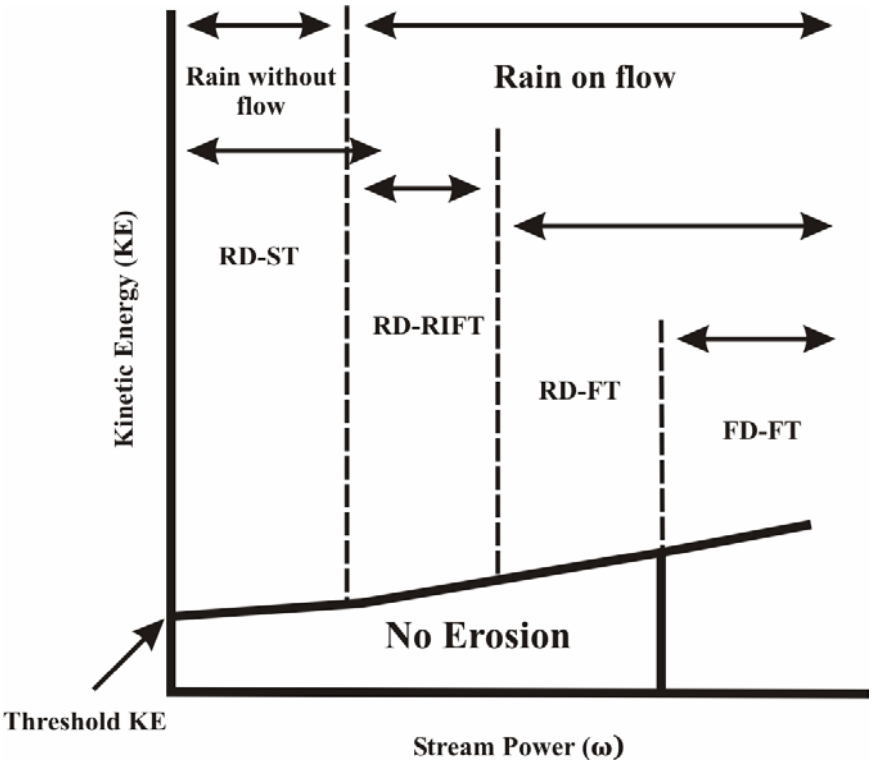

Fig. 1.2. Detachment and transport processes; simplified from Kinnell (2005).

1.2.1.1. Raindrop detachment and transport

There are two agents detach the soil particles from the soil matrix which are the raindrop and runoff flow. However, under interrill soil erosion the dominant detachment process is due to the raindrop impact. The mechanism of the rainfall detachment involves the raindrop energy used to overcome the bonds that hold particles in the soil surface and also used to transport the detached particles away. The aforementioned condition is before the start of surface runoff. However, under water flow conditions, the raindrops can penetrate through the flow depth to detach the soil particles that may then splashed or transported by water flow. In some cases, when the water flow depth is rather large, the raindrops are not able to penetrate the flow depth but it will enhance the capacity of the sediment transportation (Jayawardena and Razur, 1998). The detachment due to single raindrop impact has been well studied by several researchers (Ghadiri and Payne, 1981; Al-Durrah and Bradford, 1982; Gantzer et al., 1985; Nearing et al., 1986). The detachment due to multiple raindrops has also been studied by numerous researchers (Kinnell, 1974; Poesen and Torri, 1988; Bradford and Huange, 1993) and different relationships developed by single-drop experiments were upheld in multiple-drop experiments. The techniques used to evaluate the detachment under

multiple-drop were variable in terms of scale and applied rainfall, which generate different results.

The splash (*RD-ST*, also can be considered as raindrop detachment and transport) process begins when water droplets strike the soil surface. The splash processes can be characterized as two subprocesses; the detachment of soil particles from the surface mass and the transport in random directions (Mouzai and Bouhadef, 2003). These processes are the result of the water-soil elastic or inelastic collision. The effect of water drop on soil detachment is related to the drop's diameter, mass, shape, fall height, drop force, and impact pressure (Mouzai and Bouhadef, 2003). On the other hand the soil also has an impact on the mass of the detached soil. This impact can be related to the soil surface properties and soil matrix properties **(Fig. 1.3)**.

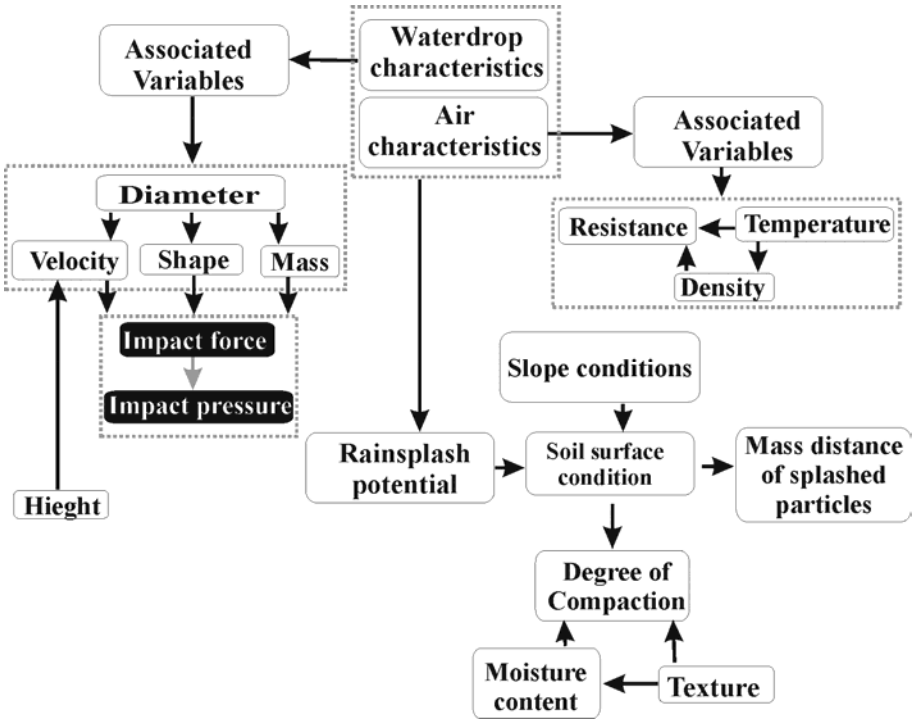

Fig. 1.3. Raindrop detachment and transport processes as described by Mouzai and Bouhadef (2003).

Before the runoff starts, the soil detachment and transport is mainly due to the impact of raindrop on the soil surface resulting in soil detachment and sediment splash. When the raindrop strike on a saturated soil surface, a hemispheric cavity is formed on the surface

due to the impulsive load of the spherical drop. The vertical compressive stress of the drop is then transformed into lateral shear stress of radial flow of water jetting away from the center of the cavity (Sharma, 1996). Al-Durrh and Bradford (1982) monitored these steps using high-speed camera and presented them as high and low-strength soil level **(Fig.1.4)**. Park et al. (1982) described the mechanism of drop detachment and splash as a case of fluid movement by process of impingement and Rayleigh jet in a drop-liquid-solid domain.

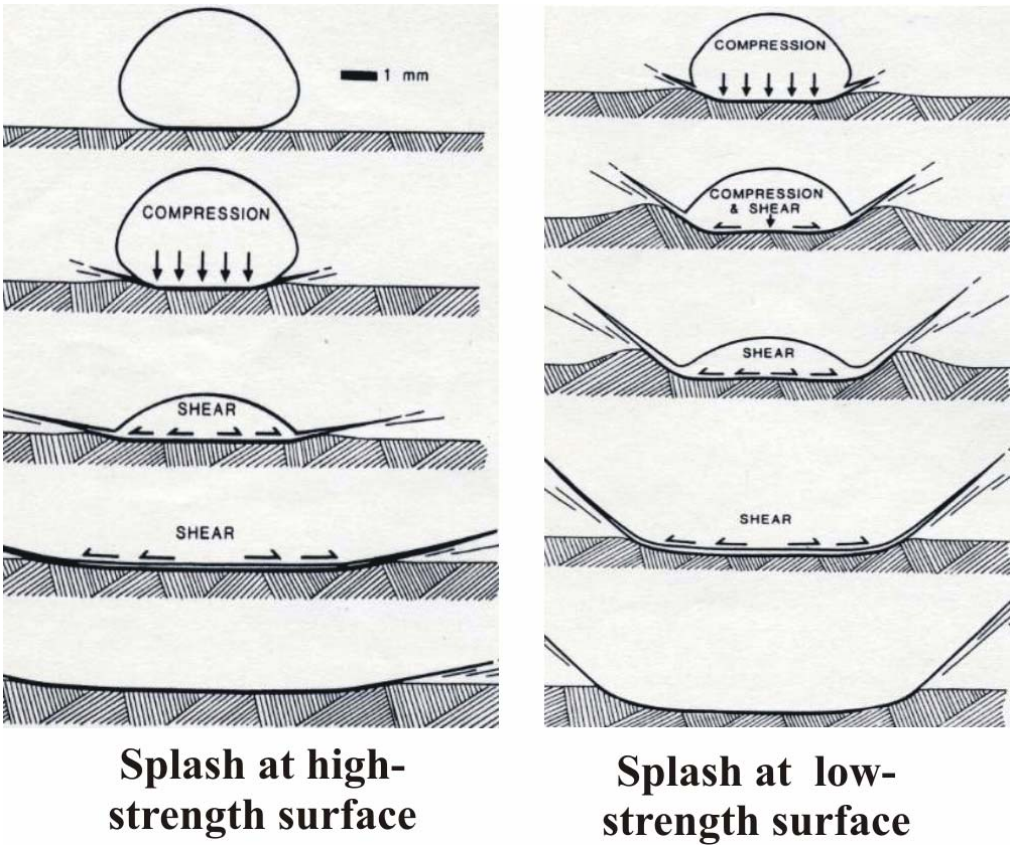

Fig. 1.4. Splash mechanisms under high- and low-strength conditions (Al-Durrah and Bradford, 1982)

1.2.1.2. Flow detachment and transport

Detachment by surface flow or flow entrainment of sediments is primarily considered in the domain of rill erosion processes (Sharma, 1996). For interrill erosion prediction the detachment of soil by shallow overland flow alone is assumed negligible (Foster, 1982). The processes of the soil detachment and transport under the presence of overland flow are very complicated processes. After the soil particles are detached and lifted from the

soil matrix they (a) remain suspended in the flow for sufficient time to pass out of the eroding area without returning to the bed, or (b) return to the bed but the flow has sufficient power to move them downstream without aid from raindrop impact (Kinnell, 2005). Moss (1988) attributed most of the sediment at the outlet to the combined action of raindrop and flow. The solid load of flow transportation is splited into suspended and bedloads portions. The bedload particles that can not be transported by the flow alone remain on the bed until lifted back in the flow by force of raindrops impacting the shallow overland flow (Kinnell, 1988).

1.2.1.3. Deposition

When the stream power of the overland flow is obstructed due to surface roughness, plant stalks, and stubble mulches, or when flow turbulence is lowered due to decrease in slope steepness or frequency of rainfall impact, the sediments in bedload and some suspended load settle on the surface (Sharma, 1996). The erosional transport of material through the landscape is rarely continuous. Instead, the particles may undergo repeated cycles of entrainment, transport, and deposition (Pidwirny and Draggan, 2008). Transport depends on an appropriate balance of forces within the transporting medium. A reduction in the velocity of the medium, or an increase in the resistance of the particles may upset this balance and cause deposition **(Fig. 1.5)**. Reductions in competence can occur in a variety of ways. Velocity can be reduced locally by the sheltering effect of large rocks, hills, and stands of vegetation or other obstructions. Normally, competence changes occur because of large-scale reductions in the velocity of flowing medium (Pidwirny and Draggan, 2008). In micro-scale, the deposition of the particle depends on particle size, drop size, and depth and velocity of flow (Kinnell, 1988).

1.2.2. Factors affecting interrill erosion

The interrill soil erosion can be divided to subprocesses, and each process is affected by a group of factors. However, generally these subprocesses are affected by (a) rainfall properties, (b) soil properties, and (c) surface properties (Park et al., 1982). The rainfall properties determine the erosivity of raindrops and flow (Sharma. 1996). These factors can be summarized as shown on **Fig. (1.6)**.

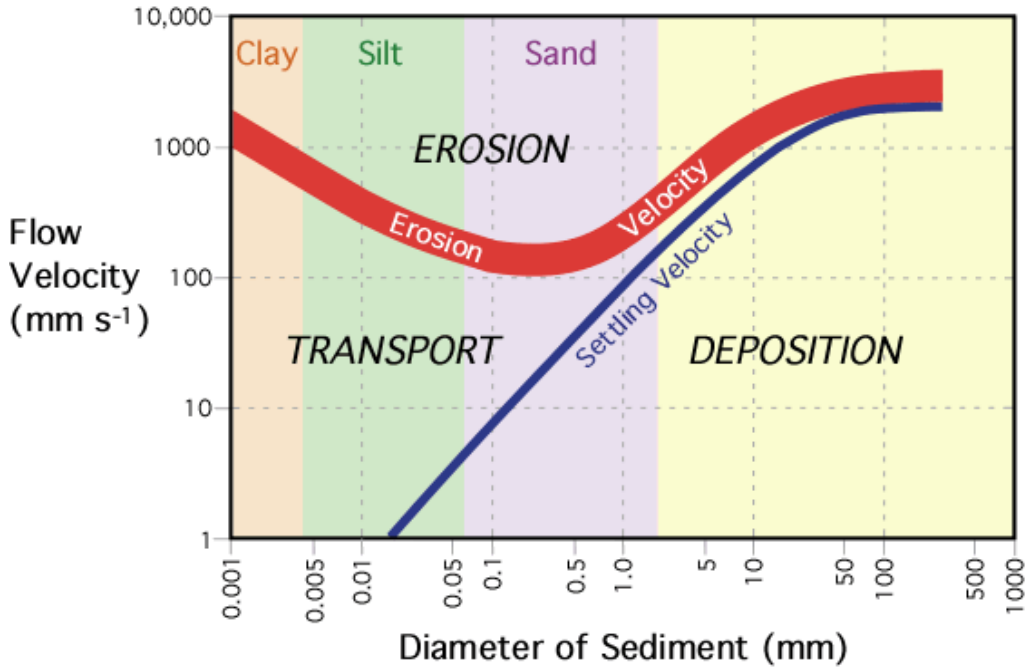

Fig. 1.5. Relationship between stream flow velocity and particle erosion, transport, and deposition (Source: www.physicalgeography.net).

1.3. Rainfall erosivity measurement and evaluation

Rainfall erosivity can be defined as the ability of rainfall to cause soil erosion. Previous studies indicated that the amount of detached soil by a depth of rain is directly related to the intensity at which rain falls (Van Dijk et al., 2001). Soil particles detach when the incident raindrop generates a stress grater than the soil strength. Single water drops with different size and fall from different heights have been used to examine the relationship between the drop properties and the detached mass (Ghadiri and Payne, 1977; Sharma and Gupta, 1989). However, these studies ignored the rainfall microstructure that the rainfall is consisting of spectrum of drop sizes. The erosivity of the rainfall is dependent upon the nature of the distribution of those drop sizes.

The current erosion models such as RUSLE and WEPP are based upon models of the distribution of raindrop sizes that date back to the 1940s; developed by Law and Parsons (1943) and Marshall and Palmer (1948). These studies are based on small samples collected using flour pellet or plotting paper methods (Fox, 2004). However, most of the recent studies indicated that the small sampling will cause a big uncertainty on the relationship between the different rainfall variables.

The common suggested descriptors of erosivity are kinetic energy (KE, half the product of the mass and the velocity squared of the falling drops), and momentum (the product of mass and velocity). Generally, the developed erosivity indices are based on the raindrop mass and velocity. In this regards, the most of the methods used to measure the rainfall erosivity attempted to measure the mass and fall velocity of each raindrop.

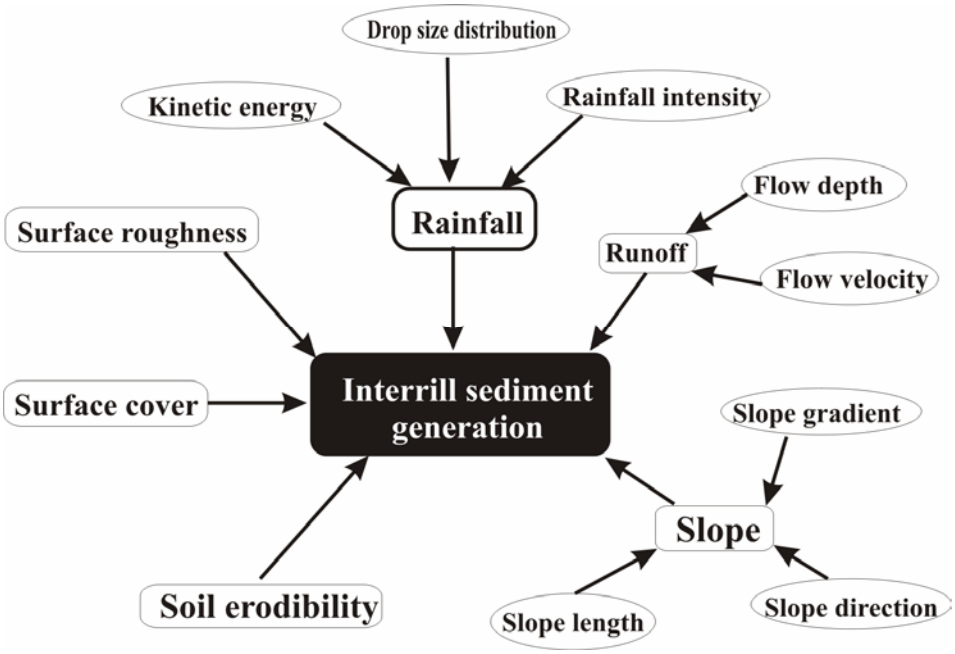

Fig. 1.6. Diagram shows the major factors affect the sediment generation at interrill area.

1.3.1. Measurement methods

1.3.1.1. Direct measurement of kinetic energy (KE)

The direct measurement of rainfall KE is not widely used. This measurement involves the use of pressure, force, and acoustic piezoelectric transducers. When these transducers are strained by an external force, displaced electrical charge accumulates on opposing surfaces **(Fig. 1.7)**. The transducers are, generally, produced from crystalline quartz either in its natural or high-quality reproduced form. Different types of the piezoelectric materials can be used to construct piezoelectric sensors. The signals produced by these sensors must be conditioned and amplified prior to being analyzed by the oscilloscope, analyzer, recorder or other read out devices **(Fig. 1.7)**. The piezoelectric sensors usually include built-in microelectronic or external sensor microelectronic circuit (charge mode).

Accordingly, the piezoelectric sensors offer unique capabilities which are typically not found in other sensing technologies. Several studies have applied the force piezoelectric sensors for rainfall measurement such as KE (Nearing and Bradford, 1986; Jayawardena and Rezaur, 2000). However, the acoustic transducer are rarely been used in the field of rainfall energy measurement.

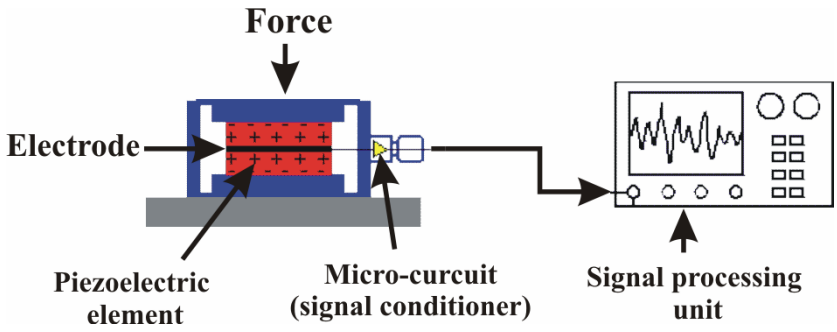

Fig. 1.7. Schematic draw illustrating the piezoelectric transducer approach (Modified from: www.davidson.com.au).

1.3.1.2. Kinetic energy from drop size distribution (DSD)

Trials on raindrops measurements are being done since 1892, which described observations of splash patterns on slates (Campos, 1999). This method consists of exposing sheets of filter-papers, dusted with a water-soluble dye, to rain for brief interval (a few seconds). After striking the paper, the drops cause spots that are rendered permanent by the dye. The diameter of the spot is then assumed to depend only on the diameter of the drop. However, the spot diameter, actually, is also a function of the effective thickness of the paper, which depends on the drop size and drop fall-velocity. The humidity in the paper also affects the relationship between the actual and spot diameter. An empirical relationship between the drop diameter and the spot diameter is then used to obtain the raindrop size. The major problem of this method is the large drops splatter when striking the filter paper and the precise determination of their size is not possible.

Another direct method for DSD measurement is the flour pellet method, originally developed by Bentley (1940) and modified by Laws and Parsons (1943). The procedure consists of allowing the raindrop to fall into a layer 2-3 cm deep of fine un-compacted flour; the smooth flour surface is held in a shallow container about 10 cm in diameter, which is generally exposed for rain for few seconds. The raindrops remain in the flour

until they form dough-pellet when the drops become dry and hard. These pellets are then separated by a set of standard into group of several sizes. However, the limit of the drop sizes cannot be found from the dimensions of the sieve-openings because of the flattening the drop undergoes in becoming a pallet (Campos, 1999). For this reason, the mass of average pellets is used to define the size-groups.

These two methods are major direct measurement methods for the drop size beside other methods such as, heavier fluid, super-cooled liquid, and photograph methods. There are some other continuous measuring methods such as; Joss-Waldvogel disdrometer, radar methods. The Joss-Waldvogel is the most widely used disdrometer; it is an electromechanical sensor that transforms the momentum of the raindrops, falling on area of 50 cm^2, into electrical pulses **(Fig. 1.8)**.

For the calculation of the rainfall erosivity indices (KE), the velocity of the raindrop must be determined. Usually, the empirical relationships between the drop size and the fall terminal velocity are used to determine the KE and momentum (M) base on the following equations:

$$KE = \tfrac{1}{2} m v^2 \qquad (1.1)$$

$$M = mv \qquad (1.2)$$

where KE is the kinetic energy, M is the momentum, m is the drop mass, and v is the drop velocity. The development of their empirical relationships is based on laboratory measurements. The most common relationship is Gunn and Kinzer (1949) based on equation (Eq. 1.3, 1.4, and 1.5).

$$F = \tfrac{1}{2} \rho v^2 Sc \qquad (1.3)$$

$$G = \tfrac{1}{6} g \pi d^3 (\rho s - \rho) \qquad (1.4)$$

Equation 1.3 and 1.4 can be combined as fallow

$$V^2 = \tfrac{4}{3} g d (\rho s - \rho) / \rho c \qquad (1.5)$$

where F is the force acting on the sphere in the direction opposite to its motion, ρ is the density of the surrounding fluid, v is the velocity of sphere, S is the projected area of the sphere, G is the gravitational force acting downward, g is the acceleration due to gravity, d is the diameter of the sphere, and V is the terminal velocity. Various relations have been developed based on Gunn and Kinzer (1949) experimental data.

Other relations also exist and still in use such as; Laws (1941), Laws and Parsons, (1943), Bread (1976), Bread and Pruppacher (1969), and Atlas and Ulbrich (1977).

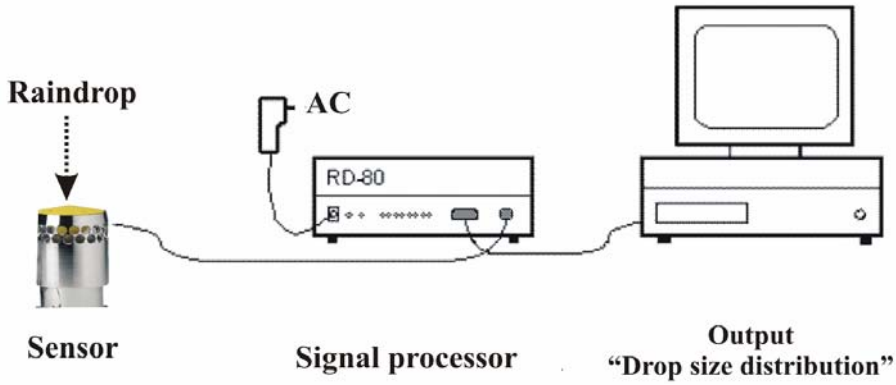

Fig. 1.8. Joss-Waldvogel disdrometer (Modified from: www.distromet.com).

1.3.1.3. Measurement of raindrop diameter and velocity

These types of measurement method are generally based on the spectral and optical approaches. The optical spectro-pluviometers are based on the shadowgraph principles to assess the DSD **(Fig. 1.9)**. The principle of the shadowgraph is simple; the infrared light (0.9 μm) is transmitted by a diode illuminates a 60 cm^3 cuboid beam of parallel light shaped by a pair of converging lenses and rectangular mask (Salles et al., 1999). The total light intensity transmitted through the beam is monitored by a single receiving photodiode, which deliver an electric signal proportional to the receiving light intensity. When a drop fall across the beam, the light intensity received by the photodiode decreases. The amplitude and the duration of the signal variation are proportional to the cross-section of the drop and to residence time in the beam, respectively. The residence time can be converted to a fall velocity assuming the drop crosses the two horizontal faces of the beam separated by known height. The signals from the photodiode are processed and stored in microcomputer or data logger. The rainfall erosivity can be then calculated directly from the individual drop size and velocity.

Another example of the optical sensors is the drop-sizing gauge (Nanko et al., 2007). This device includes a paired laser transmitter and receiver. When the raindrop passes though the laser sheet, the output voltage from the receiver is reduced proportional to the intercepted area. The raindrop sizes are then calculated from the relationship between the interception rate and the output voltage (Eq. 1.6, and 1.7). The optical sensors are usually calibrated at laboratory using sphere glasses and known waterdrop size. The drop velocity can be calculated fro the residence time and the laser sheet width (Eq. 1.8).

$$\frac{b}{a} = 1 \quad (D \le 1mm) \tag{1.6}$$

$$\frac{b}{a} = 1.05 - 0.0655D \quad (D > 1mm) \tag{1.7}$$

where a is the major axis of an oblate spheroid (mm), b is the minor axis of an oblate spheroid (mm), and D is the equivalent spheroid diameter (mm) calculated from drop volume assuming the drop had a sphere shape.

$$v = \frac{b + L - d'}{T} \tag{1.8}$$

where b is the minor axis of a raindrop oblate spheroid, L is the laser sheet width, T is the intercepted time, d' the necessary distance to detect a raindrop (distance required to produce voltage).

Although the optical sensor produces sufficient data to calculate the erosivity indices, their measurements are highly dependent on single drop shape assumption. This point will increase the uncertainty of the outputs from the sensor.

Fig. 1.9. Optical drop size and velocity measurement; Parsivel laser disdrometer (Source: http://gpm.gsfc.nasa.gov).

1.3.2. Erosivity evaluation

Rainfall kinetic energy represents the most common rainfall erosivity indicators; although some studies have presented other rainfall indices preformed better under

certain experimental conditions. The expenditure of rainfall kinetic energy at the ground surface can be expressed in two ways, either as rate (energy flux density), KE_t, with units of energy per unit area per unit time (J m^{-2} s^{-1}), or as the energy density per unit of rain, KE_c, with units of energy per unit area per unit quantity of rain (J m^{-2} mm^{-1}) (Kinnell, 1987).

1.4. Soil microtopography

Soil microtopography/roughness or microrelief is generally a function of soil tillage-induce clod size, clod distribution, and plant stubble distribution (Sharma, 1996). However, the rainfall impact also has a great influence on determining the soil surface roughness (Wesemael et al., 1996). The soil microtopography influences the extent of sediment generation and redistribution, seal formation and soil loss (Sharma, 2006). The soil microtopography is classified as dynamic soil property which changes rapidly with time and space.

The soil microtopography determines, to some extend, several processes involved in soil surface and water. The soil microtopography has impact on the surface runoff initiation and water flow mainly by two factors; the depressions which store water and delay the runoff and enhance the infiltration, and increase surface flow resistance (Gover et al., 2000; Darboux et al., 2002; Darboux and Huang, 2005).

1.4.1. Methods of measurement

The quantification of soil surface microtopography consists of two steps: (i) the collection of surface-elevation data, and (ii) the analysis of elevation data sets (Huange and Bradford, 1992). The measurement methods of the surface-elevation can be classified into two categories: contact and non-contact methods.

1.4.1.1. Contact methods

The methods belonged to this category are direct measurement methods and it is prerequisite to touch the soil surface in order to measure the surface-elevations. There are two major methods in this category; the pin method (Kuipers, 1957; Allmaras et al., 1966) and the chain method (Saleh, 1993). The pin meter **(Fig.10)** consists of an aluminum frame carrying a bar with 1 mm diameter steel pins positioned at a spacing of 5 mm. The bar is inserted into drill-holes and can be shifted in 25 mm intervals. When

lowered onto the soil surface, the tops of the pins form a nearly continuous line which is traced onto a 1 mm graph paper. The pin meter was always set parallel to the soil surface. Chain length as well as pin meter readings are immediately typed into a computer and are directly available for analyses (Jester and Klik, 2005). The chain method can be described as a chain with given length, L1, is placed across the soil surface with the horizontal distance covered, L2, this L2 decreases as the roughness increases (Saleh, 1993; Govers et al. 2000). The major disadvantage of contact elevation measurement devices is the deformation of the original soil surface profile, especially on loose grains or wet soils, and limited resolution (Jester and Klik, 2005).

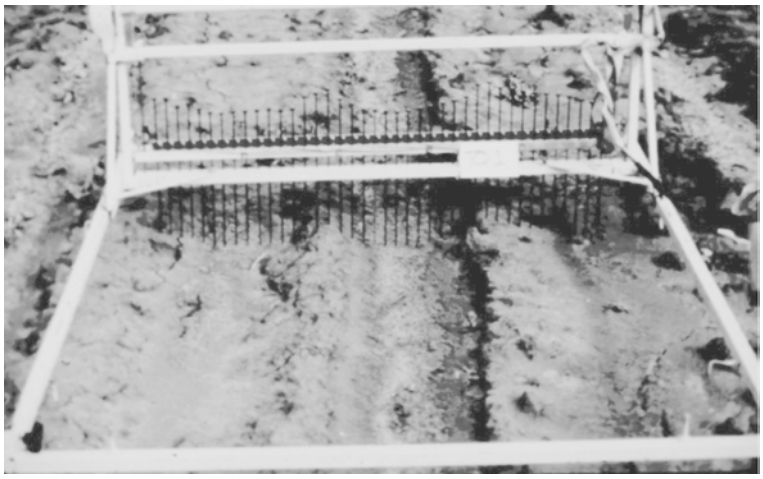

Fig. 1.10. Pin-reliefmeter (Source: www.weru.ksu.edu).

1.4.1.2. Non-contact methods

The non-contact methods are indirect methods, which include the photogrammetry (Welch et al, 1984) and Laser (Huange and Bradford, 1992) methods as major methods in this category.

The laser scanner is used for automated measurement of surface elevations by optical triangulation technique with the help of a laser beam **(Fig. 11)**. Jester and Klik (2005) described their laser device that consisted of three major parts: a) an optical transducer for the detection of surface elevation, b) a computer-controlled, motor-driven two-dimensional traversing frame, and c) a set of interface circuitry and a PC to control the motion of the camera-laser carriage and to record elevation data. A low power HeNe laser is used to project a laser spot onto the soil surface. The reflected laser light is focused by a conventional 35 mm camera onto a 512-element photodiode array mounted

at the back of the camera. The position of the signal on the diode array is related to surface elevation by trigonometric rules. The elevation range depends on the laser camera distance and angle, the focal length of the lens and the size of the photodiode array. The maximum range of detectable elevation differences are approximately 500 mm. Surface relief is measured point by point in a regularly spaced grid. The maximum scanning area is 1.0 x 1.0 m. Laser data stored in an x–y matrix form had to be prepared for further analyses. For quick data processing FORTRAN routines have been developed. First, the data rows had to be mirrored because the last point in a row is stored as the first value. Then every second row was shifted because of a systematic shift in horizontal position depending on the scan direction. The edge regions with high system noise are cut and the desired grid (2x2 mm) is extracted. Outliers in elevation data are defined as points which differ in height by at least 5 mm from each of their eight neighbors. Missing values (error readings and removed outliers) are interpolated using an inverse distance method (weighting power; nearest neighbors; variable search radius) (Jester and Klik, 2005).

The photogrammetry system allows for more rapid data acquisition as compared to the laser scanner. This method employs a more flexible camera-to-object distance, and ultimately allows for a wider vertical range of the DEM. In addition to that, a camera is easier to handle, and a photogrammetric system can be scaled according to the project requirements (Rieke-Zapp and Nearing, 2005). Automated digital photogrammetry allows DEMs to be generated with sufficient resolution for microtopography analysis. Previous studies have shown the application of correlation matching to soft copy of images for soil microtopography analysis. Recent advances in digital image processing and camera calibration techniques allow the use of digitized images taken with consumer-grade analogue cameras for automated DEM generation (Rieke-Zapp and Nearing, 2005).

1.4.2. Microtopography evaluation

The second step of the soil surface microtopography quantification is the analysis of elevation data sets acquired by the different devices. Several indices have been developed in order to describe the soil microtopography numerically **(Table 1.1)**. The roughness indices can be classified into two groups; first group assume that the surface has a random roughness with no spatial correlation, and the second group assumes that there is spatial correlation on the surface elevations. However, the facts say that there is

no index able to describe the variation and the correlation at the same time (Huange and Bradford, 1992).

Other types of information can also be extracted from the elevation data sets, like depression area and storage and micro-rills delineation. These surface features have a great impact of the on the water and sediment flow in the interrill areas.

Table 1.1. Some major roughness indices used to evaluate soil microtopography.

Index	Name	Formula[§]	Reference
RR	Random roughness	$\left[\frac{1}{k}\sum_{i=1}^{k}(Z_i - \overline{Z})\right]^{1/2}$	Allmars et al. (1966)
LD	Limiting elevation difference	$\frac{1}{a}$	Linden and Van Doren (1986)
LS	Limiting slope	$\frac{1}{b}$	Linden and Van Doren (1986)
MIF	Microrelief index x peak frequency	$MI \times F$	Römkens and Wang (1985)
T3D	Tortuosity index	$\frac{TSA}{TMA}$	Helming et al. (1992)

[§] Z_i is the elevation reading at i point; $\overline{Z}$ is the mean of the elevation readings; k is number of readings; a and b are regression parameters in $1/\Delta Z_h = a + b(1/h)$; ΔZ_h is first-order variance, h is distance lag; *MI* is area per unit length between a measured surface profile and the regression line though it; *F* is number of elevation maxima per unit transect length; *TSA* and *TMA* are total surface area and total map area, respectively.

1.5. Modeling of soil deformation due to raindrop impact

With the increased computing powers during the last 20 to 30 years, there has been a rapid increase in the exploration of erosion and sediment transport through the use of computer models (Merritt et al., 2003). The detachment, transport, and deposition occur simultaneously in interrill areas. The interrill soil erosion can be modeled as single-drop kinetic energy dissipation or considering the interrill area as a sediment pool and the total detachment is the amount of sediment transported out of the reference area. However, most of the models did not include the amount of rainfall energy that dissipates for soil sealing and aggregates breakdown.

Fig. 1.11. Laser scanner measuring microtopography in wind tunnel (Source: www.weru.ksu.edu).

1.5.1. Sediment generation modeling approaches

A wide range of models exists for use in simulating sediment transport and associated pollutant transport. These models differ in terms of complexity, processes considered, and the data required for model calibration and model use. In general there is no 'best' model for all applications. The most appropriate model will depend on the intended use and the characteristics of the catchment being considered. Generally, the models fall in three categories; empirical or statistical, conceptual, and physically-based models.

Empirical models are generally the simplest of all three model types. They are based primarily on the analysis of observations and seek to characterize response from these data. The Conceptual models are typically based on the representation of a catchment as a series of internal storages. They usually incorporate the underlying transfer mechanisms of sediment and runoff generation in their structure, representing flow paths in the catchment as a series of storages, each requiring some characterization of its dynamic behavior. Where the Physically-based models are based on the solution of fundamental physical equations describing stream flow and sediment and associated nutrient generation in a catchment. Standard equations used in such models are the equations of conservation of mass and momentum for flow and the equation of conservation of mass for sediment (Merritt, et al., 2003).

1.5.2. Modeling of soil microtopography changes

Most of the models aimed to predict the soil erosion, generally, do not consider the changes occurred on the soil surface due to the rainfall impact energy. The raindrop

disturb the soil surface by causing aggregates break down into smaller fragments, fragment transportation by splash, structural-crust formation, and sedimentary-crust formation after the initiation of runoff. Some equations were developed to simulate the changes in the soil roughness indices as a function of the cumulative rainfall depth (Onstad et al., 1984). The random roughness index was used in this equation as follow:

$$RR = RR_0 + \beta_r [CR/(1+CR)] \quad (1.9)$$

where RR is random roughness index, RR_0 is initial random roughness, CR is cumulative rainfall and β_r is a regression coefficient. However, this types of equations act differently at different soil types and conditions (Wesemael et al., 1996). New approaches are also available using sophisticated techniques such as cellular automata and self organize dynamics approaches.

1.6. Objectives

Deformation of soil surface due to raindrop impact involve several processes are not well understood yet. When the raindrop strikes the soil surface several subsequent deformations occur on the soil surface. These deformations include soil detachment, surface sealing formation, clod destruction, and soil surface smoothing. The research on the interrill soil erosion was started in 1940s by monitoring the effect of a single drop on soil detachment under non-cohesive soil conditions. However, the successive studies failed, to some extend, to extrapolate these single-drop studies to the large scale. Good understanding of rainfall-impact on soil surface processes is necessary. Most of the current process-based erosion models do not represent all the rainfall-impact factors and processes; such as rainfall characteristics and their effect on sediment generation, the reaction of soil matrix to the raindrop, and the changes on soil microtopography. Based on the aforementioned assumptions and concepts, the objectives of this research were:

1. Measurement and evaluation of rainfall microstructure properties that affect the rainfall erosivity and their effect on the sediment generation under simulated rainfall (multiple-drops simulation system) using piezoelectric transducers.
2. Quantification of soil microtopography parameters that influence the water and sediment flow under interrill area conditions using a low cost close-range photogrammetry system.

3. Estimation of the interrill sediment generation using various modeling approaches.

In order to fulfill these objectives a series of simulated rainfall experiments were performed.

CHAPTER 2:
Rainfall Impact Energy: Measurement and Evaluation

2.1. Introduction

Rainfall impact energy represents the main driver for soil particle detachment, surface sealing and soil microtopography evolution. This energy causes the destruction of the soil aggregates to small soil particles susceptible for air/water transfer. Soil erosion by splash can be directly related to the soil properties (mass and surface properties) and raindrop properties (diameter, mass, velocity, shape, fall height, force, and impact pressure) (Mouzai and Bouhadef, 2003). Several studies have been done to determine the effect of the soil properties on soil erosion (Mouzai and Bouhadef, 2003). On the other hand, the rainfall properties were measured to evaluate the rainfall erosivity, i.e. the ability of rainfall to detach soil particles. Numerous erosivity indices were reported on the literature (Mouzai and Bouhadef, 2003). However, all these indices are based on the raindrop mass and fall velocity. The most used erosivity index in simulated and natural rainfall is the rainfall kinetic energy, which is half of the product of mass and squared fall velocity (Salles et al., 2000). The rainfall micro-properties, and for long time, have got less consideration in the fields of hydrology, geomorphology and soil science. Because it was difficult to obtain continuous measurements for raindrop properties. Piezoelectric transducer is a recent method able to provide continuous information about the rainfall depth and intensity with high accuracy relying on the drop impact measurement (Salmi and Ikonen, 2005). In this study, the piezoelectric transducer was used to measure the raindrop impact of the rainfall generated by a dripper-type rainfall simulator. The direct measurement of kinetic energy using the transducer was compared to estimated kinetic energy, which was calculated from the drop size distribution (*DSD*) and empirical terminal velocity relationships. Also, the impact of the rainfall micro-structure on the rainfall kinetic energy was assessed.

2.2. Materials and Methods

2.2.1. Rainfall simulator

A dripper-type rainfall simulator located at the Arid Land Research Center, Tottori University, Japan; was used to simulate rainfall with different rainfall intensities **(Fig.**

2.1). The rainfall simulator was 12 m in height, which is sufficient for more than 95% of the raindrops to reach their terminal velocity.

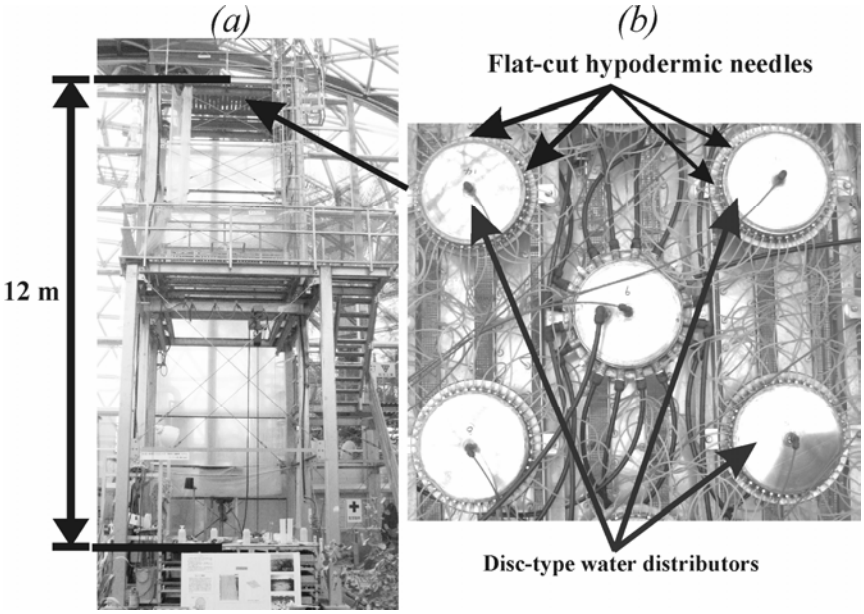

Fig. 2.1. Dripper type rainfall simulator; (a) is general view of the rainfall simulator and (b) is the drop simulation system.

The rainfall simulator was equipped with a computer system, which control the solenoid valves, pump flow rate, and an oscillating screen. The pump is positive displacement type and the flow rate was controlled by adjusting the pump rotational speed, which insured high control on the water flow rate. Air was removed from the pipe by priming system before running the rainfall simulator. The raindrops were generated using flat-cut hypodermic needles. These needles were fixed on a metallic frame organized in 18 rows. Each row included 50 needles, which were fixed on a disc-type water distributor. Below the needles, the oscillating screen was fixed to distribute the rainfall evenly. The rainfall simulator was calibrated for the rainfall spatial distribution on the experimental area (2.3 m^2), and to determine the relationship between the flow rate and rainfall intensity **(Appendix)**.

2.2.2. Rainfall characteristics and piezoelectric sensor

The rainfall erosivity was observed by the piezoelectric transducer method. This method depends on the ability of crystal plate to produce electric charge when it

receives force. Two sensors were used to measure the kinetic energy (*KE*, mJ) and drop size distribution (*DSD*, mm). The tow sensors were modified from the RAINCAP® precipitation sensor, manufactured by Vaisala, Finland **(Fig. 2.2)**.

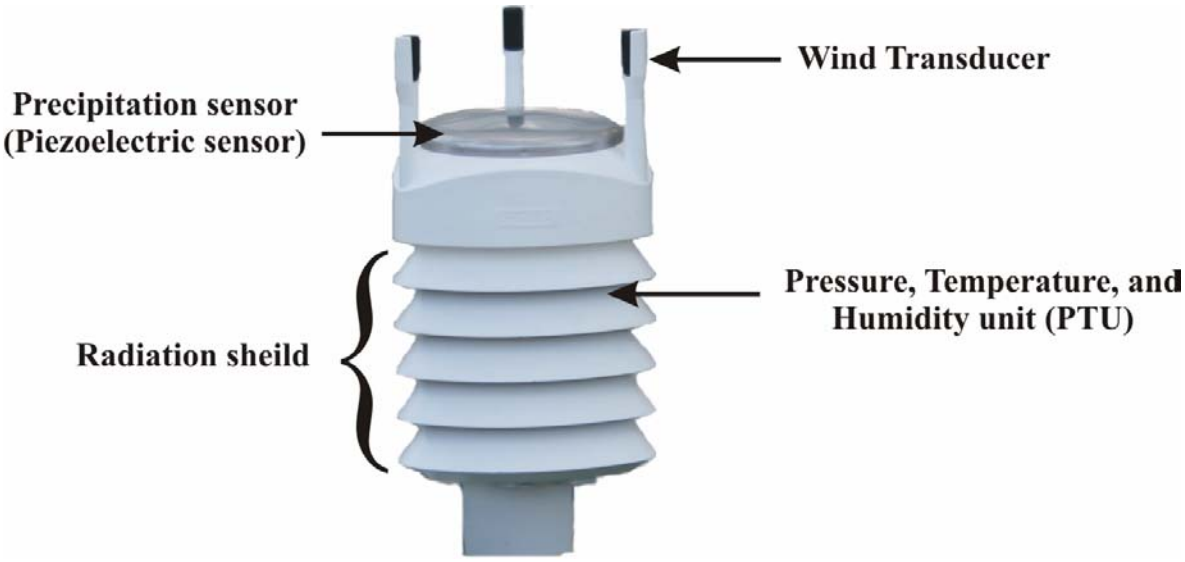

Fig. 2.2. RAINCAP® precipitation sensor and other WXT510 weather transmitter sensors (**Appendix**).

The precipitation sensor measurement was based on the acoustic detection of the impact of individual raindrops (Salmi and Ikonen, 2005). The signals from the impact are proportional to the raindrops' mass. The sensor was constructed from a piezoelectric detector (crystalline quartz) covered by a stainless steel shell used to protect the sensing element. A noise filtering technique was adopted to eliminate signals from sources other than the initial raindrop impact. Different electronics systems were used to filter, amplify, digitize, and analyze the signals produced by the sensing elements prior to the signals logging. The sensor consisted of piezoelectric disc fixed on a top of plastic body; below the plastic body there are electronics parts and both of them are covered by the stainless cover.

The sensors were calibrated using controlled drop size falling from 14 m height and the velocity of each drop size was measured using an optical method. The relationship between the drop size and the drops fall velocity was highly correlated with the Gunn

and Kinzer (1949) empirical equation (Salmi and Eloma, 2007). The sensors were also compared with Joss-Waldvogel RD-69 disdrometer under the natural rainfall conditions in Finland, and showed significant agreement for the raindrop size greater that 0.80 mm (Pohjola et al., 2008). The sensor's signal was divided to measure the raindrops' size and kinetic energy in eight size classes normalized to the mean drop diameter. In other words, each class gave the number of drops or kinetic energy received (depending on the sensor configurations) within the range of the eight drop size classes ranged between 1-5 mm. According to Pohjola *et al.* (2008), when the drop has a diameter higher than the mean it will give higher weight in number of drops and/or kinetic energy. The *KE* sensor was also validated under simulated rainfall and the sensor output was compared with the calculated *KE* using rainfall *DSD* and empirically estimated velocity, which gave statistically significant correlation under different rainfall intensities (Abd Elbasit et al., 2007). The signals from the two sensors were logged in two notebook computers using the RS-232 serial interface and data logging software to store the data in the computers used as a data logger.

The rainfall intensity was measured using a tipping-bucket rain gauge (Davis rain collector II, CA, USA) with 0.2-mm rainfall depth accuracy. The rain gauge was attached to event data logger (HOBO event; Onset Computer Corp., MA, USA) with 0.5-s time recording accuracy. The output from the two sensors was then used to calculate the rainfall erosivity parameters.

2.2.3 Rainfall impact energy (RIE) indices

Several indices were developed to quantify the *RIE* **(Table 1)**. These indices are based on the raindrop mass and fall velocity as a major drop parameters. However, the *KE* is widely used in field and laboratory studies. The Rainfall kinetic energy (*KE*) has two form; *KE* as a function of time (KE_t, J m^{-2} h^{-1}) and *KE* as a function of rainfall depth (*KE*, J m^{-2} mm^{-1}). The KE_t can be calculated from the direct measurement of the *KE* using Eq.(2.1).

$$KE_t = \left(\frac{\pi}{12}\right)\left(\frac{1}{10^6}\right)\left(\frac{3600}{t}\right)\left(\frac{10^4}{A}\right)\sum_{i=1}^{n} KE_i \qquad (2.1)$$

where KE_t is the rainfall kinetic energy as a function of time (J m^{-2} h^{-1}), t is the sampling time interval in seconds (was 10 sec), A is the piezoelectric sample area (60 cm^2), n is

the number of classes (8 drop size classes), and KE_i is the kinetic energy measured in each class.

Table 2.1. Some major rainfall impact energy (RIE) indices and their formulas.

Index	Symbol	Formula
Kinetic energy	*KE*	$\frac{1}{2} m v^2$
Momentum	*M*	$m v$
Drop force	*F*	$m v^2 D^{-1}$
Drop force/drop diameter	F_D	$m v^2 D^{-2}$
Eroding pressure	*Pe*	$4/\pi\, m v^2 D^{-3}$

The KE_c can be calculated from the KE_t and rainfall intensity using the following equation (Eq. 2.2):

$$KE_c = KE_t I^{-1} \qquad (2.2)$$

where KE_c is the rainfall kinetic energy as a function of the rainfall depth (J m^{-2} mm^{-1}), I is the rainfall intensity (mm h^{-1}).

The KE was directly measured using the piezoelectric sensor (KE_{mea}) and estimated from the *DSD* information and empirical velocity relationships (KE_{est}) as shown in Eq. (2.3). The drop velocity was estimated using Gun and Kinnzer (1949), Atlas *et al.* (1973), and Atlas and Ulbrich (1977).

$$KE_t = \left(\frac{\pi}{12}\right)\left(\frac{3.6}{10^3}\right)\left(\frac{10^4}{A\,t}\right) \sum_{i=1}^{n} N_i\, D_i^{\,3}\, v_{Di}^{\,2} \qquad (2.3)$$

where N_i is the number of drops in class i, D_i is the drop diameter of class i, and v_{Di} is the drop terminal velocity as a function of drop diameters.

The rainfall intensity (I) was measured using tipping-bucket sensor and also calculated from the *DSD* using Eq. (2.4).

$$I = \left(\frac{\pi}{6}\right)\left(\frac{3.6}{10^6}\right)\left(\frac{10^4}{A\,t}\right) \quad \sum_{i=1}^{n} N_i \; D_i{}^3 \qquad (2.4)$$

where I is the rainfall intensity (mm h^{-1}).

2.3. Results and discussion

2.3.1. Rainfall characteristics

The advantage of dripper-type rainfall simulator that it can produce rainfall with *DSD* similar to natural rainfall The relationship between the median drop size (D_{50}) and the rainfall intensity is shown in **Fig. 2.3.** This relationship was also compared with data obtained under the natural rainfall reported by Laws and Parsons (1943), Zanchi and Torri (1980), and Van Dijk *et al.* (2002).

The simulated rainfall had a D_{50} greater than the natural rainfall under these different rainfall intensities compared with the published relationships (**Fig. 2.3**). Van Dijk et al. (2002) reported that the relationship between the I and D50 can be described as a power relationship, as shown in Eq. (2.5).

$$D_{50} = \alpha\, I^{\beta} \qquad (2.5)$$

where I is the rainfall intensity (mm h^{-1}), α and β are empirical parameters ranging from 0.8 to 1.23 and from 0.123 to 0.292, respectively. The simulated rainfall followed the same relationship and the R^2 value was 0.74 (P=0.002), where α and β were 1.23 and 0.35, respectively. Under natural rainfall, the relationship between D_{50} and rainfall intensity takes different patterns depending on the geographical location. Several researchers have reported that D_{50} increases with the increase of the rainfall intensity until a certain rainfall intensity (threshold) and then stabilizes or decreases (e.g. Van Dijk *et al.* 2002; Hudson 1963).

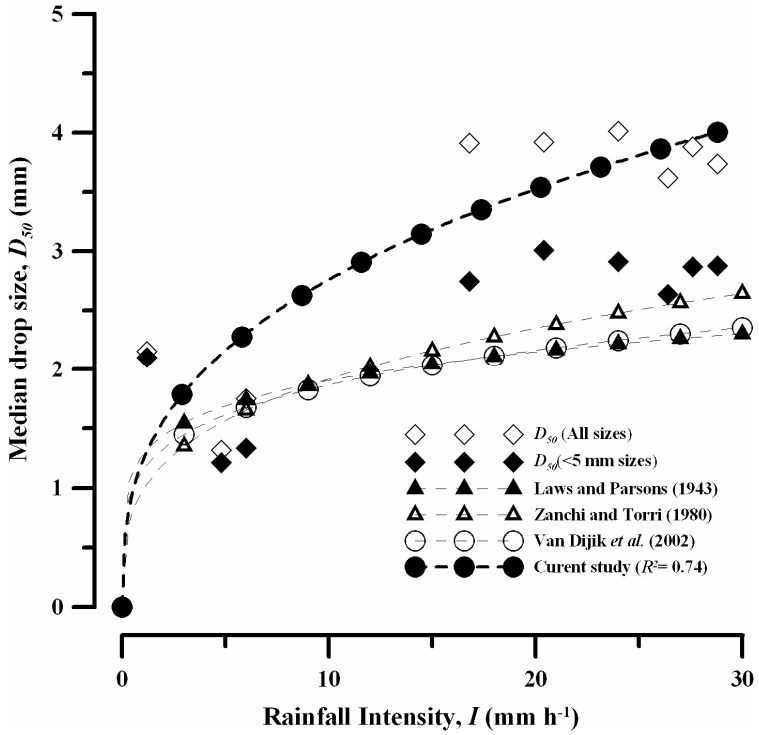

Fig. 2.3. Relationship between the median drop size and the rainfall intensity compared with natural rainfall.

2.3.2. Rainfall impact energy measurement

The *KE* was measured directly using the piezoelectric sensor. The relationship between the KE_{mea} and rainfall intensity was found to be similar to natural rainfall trend **(Fig. 2.4)**. This relationship was compared with relationships obtained under natural rainfall in different geographical locations. The KE_{mea} was higher than the natural rainfall under different rainfall intensities. This difference can be attributed to the increase of the numbers of the large drops (>3.2) with the rainfall intensity. Also, the D_{50} can be used as indicator for the increase of the large drops with the increase of the rainfall intensity. This result emphasizes the effect of the rainfall microstructure on the determination of the *RIE*. The drop volume (%) was compared to the *KE* (%) as a function of the drop size distribution and showed similar trend **(Fig. 2.5)**.

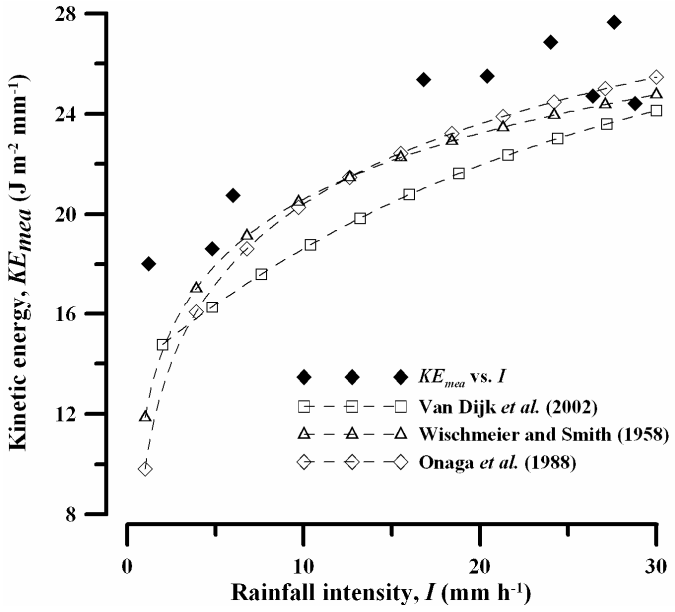

Fig. 2.4. Relationship between the simulated rainfall kinetic energy and the rainfall intensity compared with natural rainfall.

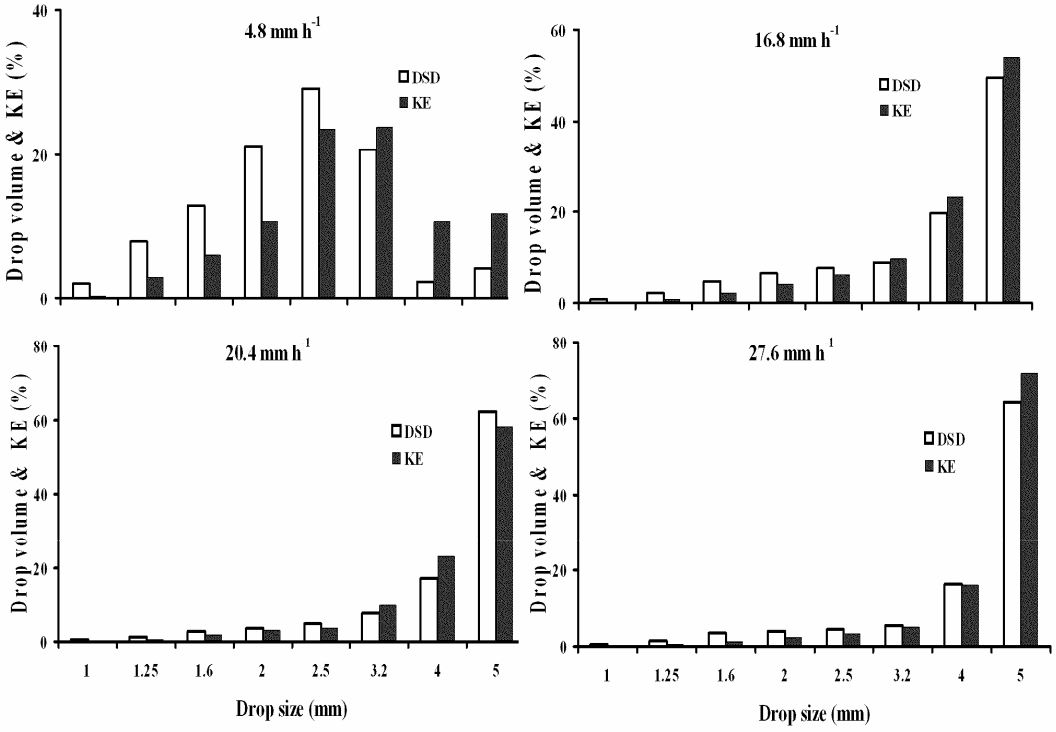

Fig. 2.5. Comparison between the drop volume and kinetic energy percent at four rainfall intensities.

The measured KE (KE_{mea}) was compared with the estimated *KE* using the *DSD* information and fall velocity empirical relations **(Fig. 2.6)**. The KE_{mea} was highly correlated with the estimated *KE* using Gunn and Kinzer (1949), Atlas et al. (1973), and Atlas and Ulbrich (1977) empirical relationships for velocity estimation, and the correlation coefficient was 0.84 (P= 0.005), 0.85 (P= 0.004), and 0.87 (P= 0.002), respectively.

The major source of the differences between the KE_{mea} and KE_{est} is that the fall velocity relationships assume that all raindrop fall by its' terminal velocity. However, the height of the rainfall simulator is only enough for small and medium drops to reach their terminal velocity while the large drops need more height to reach their terminal velocity.

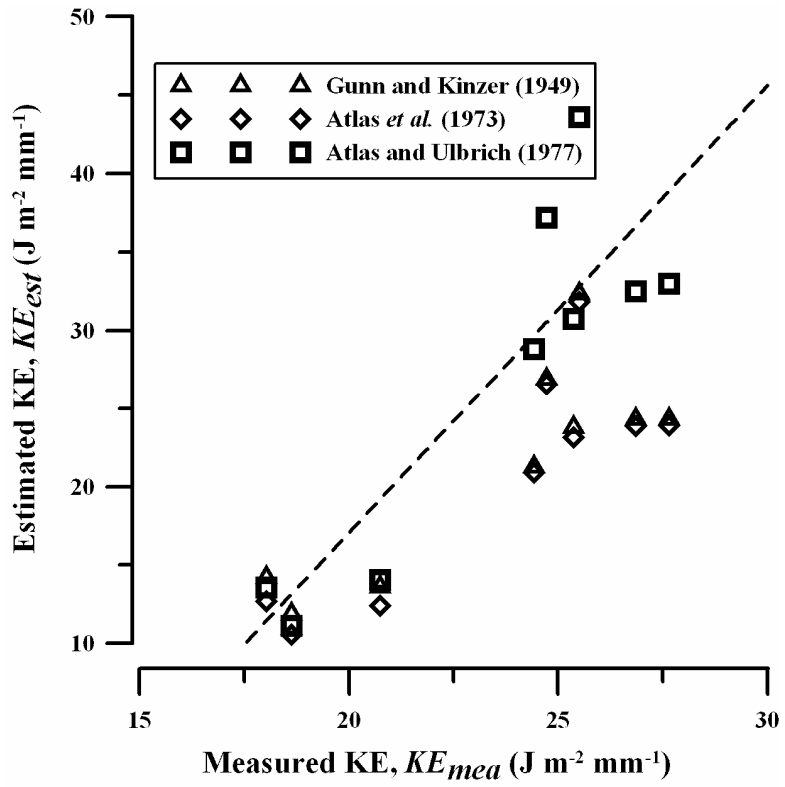

Fig. 2.6. Relationship between direct measured and estimated rainfall kinetic energy using empirically estimated raindrop terminal velocity.

2.4. Conclusions

Simulated rainfall produced by dripper-type rainfall simulator was characterized using piezoelectric transducers. The drop size distribution and kinetic energy were measured directly. The *KE* was selected as index to evaluate the rainfall impact energy.

The median drop size was higher than the reported natural rainfall relations. This result also affected the KE relationship with the rainfall intensity which showed also high *KE* under different rainfall intensities. The *KE* was showed significant association with the rainfall *DSD*. The direct measured *KE* was significantly correlated with the estimated *KE* using the *DSD* and empirical fall velocity relationships. This result emphasizes the potential use of the piezoelectric sensor to measure and evaluate the rainfall impact energy.

CHAPTER 3:

Characterization of rainfall generated by dripper-type rainfall simulator using piezoelectric transducers and its impact on splash soil erosion

3.1. Introduction

The rainfall impact energy represents the primary driver for soil particle detachment. The first stage of soil erosion can be considered from the first raindrop that strikes the soil surface, which cause the detachment of soil particles and the air transport as splash soil erosion. The splash process can be characterized as two sub-processes; the detachment of the particles from the surface mass and the transport of these particles in random directions (Mouzai and Bouhadef, 2003). The soil splash can be related to the soil properties (mass properties and surface properties) and raindrop properties. The raindrop properties include, drop diameter, mass, velocity, shape, fall height, force, and impact pressure (Mouzai and Bouhadef, 2003). Based on these raindrop properties, several erosivity indices have been suggested in order to estimate the detached soil particle mass under certain rainfall events **(Table 3.1)**.

The erosivity indices **(Table 3.1)** have been developed under natural and simulated rainfall, and under different soil types ranging between the cohesive and non-cohesive soil types. The simulated rainfall can be divided into two types; single drop simulator (SDS) and multiple-drop simulator (MDS). The single-drop simulator has been used to investigate the splash erosion processes as a function of a single drop with different sizes and fall heights (e.g. Al-Durrah and Bradford, 1982; Nearing et al., 1986; Sharma and Gupta, 1989; Mouzai and Bouhadef, 2003). Although the single drop studies have given good explanations about the splash process, they fail to extrapolate these explanations to field conditions. Multiple drop simulators produce a range of drop sizes similar to natural rainfall. There are several types of rainfall simulators basically categorized in three main groups; the drip-screens (dripper-type), sprays, and rotating sprays (Foster et al., 2000; Clarke and Walsh, 2007). The efficiency of a rainfall simulator can be measured by the ability of the rainfall simulator to produce rainfall similar to natural rainfall at a certain rainfall intensity level. However, this goal seems to be very difficult due to the temporal and spatial variability in natural rainfall itself that

corresponds to the actual the differences in the mechanisms generating natural rainfall (Van Dijk et al., 2002).

The soil mass properties, also, have a great impact on the splash mass determination. Several studies have used non-cohesive soil (sandy soil) due to its high erodibility and less susceptibility to compaction, which affect the relationship between the raindrop erosivity and the splash mass **(Table 3.1)**. On the other hand, splash erosion under cohesive soil has been described as inelastic collision, where the raindrop momentum is conserved while the energy is not (Styczen and Hogh-Schmidt, 2002). Generally, under cohesive soil conditions the raindrop energy is distributed between the splash generation (horizontal effects) and soil consolidation (vertical effects). In other words, some of the energy will be dissipated on the soil matrix, while the remaining energy can be directly correlated to splash mass. Moreover, Sharma and Gupta (1989) suggested that there is an erosivity threshold representing the minimum energy needed to overcome the inherent strength of soil. However, this threshold depends on the relationship between splash mass and erosivity parameters, which varies between soil types and conditions.

The rainfall erosivity parameters are determined by direct measurement using force transducers (Jayawardena and Rezaur, 2000), and optical methods (Salles and Poesen, 2000, Nanko et al., 2004). Other indirect methods can be conducted by measuring the rainfall drop size (DSD) by different methods such as filter paper and flour-pellet methods, and by assuming the drop velocity using empirical based relationships (Sharma and Gupta, 1989; Mouzai and Bouhadef, 2003) or physically-base equations (Kinnell, 2005)for drop fall in still air.

The piezoelectric transducer has been proved to be a good method for the measurement of rainfall properties, such as rainfall volume (Förster et al., 2004, Salmi and Ikonen, 2005) and kinetic energy and momentum (Madden et al., 1998; Jayawardena and Rezaur, 2000). The advantage of the piezoelectric transducer is that it relies on the drop impact (mass and velocity) for the measurements rather than the shape. A disadvantage can come from a water layer forming on the sensing surface, and the effect of this layer can be reduced by using convex sensing surfaces.

In previous studies, several rainfall simulator types have been used to study the relationship between rainfall properties and splash erosion. However, the measurement of rainfall properties using piezoelectric transducers combined with splash measurement has rarely been done. Accordingly, this study dealt with two problems; the problem of

the characteristics of the rainfall produced by a dripper-type rainfall simulator, and the splash estimation from cohesive soil types.

The objectives of this study were to assess the relationships between the rainfall intensity and the drop erosivity indices under a dripper type rainfall simulator using piezoelectric transducers, and to evaluate the effect of these relationships on the splash estimation under cohesive soil conditions.

Table 3.1. Major raindrop erosivity indices.

Index	Symbol	Formula	Rainfall [(a)]	Soil type[(b)]	References
Kinetic energy	KE	$½\ m\ v^2$	SDS, MDS, NR	CS, N-CS	Al-Durrah and Bradford, (1982); Riezebos and Epema, (1985); Kinnell, (2005)
Momentum	M	$m\ v$	SDS, MDS	CS, N-CS	Al-Durrah and Bradford, (1982); Salles et al., (2000)
Kinetic energy x drop circumference	KE_C	$KE \times (\pi D)$	SMS, MDS	CS, N-CS	Gilley and Finkner, (1985)
Momentum x drop diameter	MD	$M \times D$	SDS, NR	CS, N-CS	Salles et al., (2000); Nanko et al., (2008)
Drop force	F	$M\ v^2/D$	SDS	Aggregates	Ghadiri and Payne, (1977)
Drop force/ drop diameter	F_D	$M\ v^2/D^2$	SDS	Aggregates	Ghadiri and Payne, (1977)
Eroding pressure	P_e	$4M\ v^2/\pi\ D^3$	SDS	N-CS	Mouzai and Bouhadef, (2003)

[(a)]SDS, MDS, NR are single raindrop simulator, multiple raindrop simulator, and natural rainfall, respectively.
[(b)]CS, N-CS are cohesive and non-cohesive soil, respectively.

3.2. Materials and Methods

3.2.1. Rainfall simulator

A dripper-type rainfall simulator located at the Arid Land Research Center, Tottori University, Japan was used to simulate rainfall with different rainfall intensities **(Fig. 3.1)**. The rainfall simulator was 12 m in height, which is sufficient for more than 95% of the raindrops to reach their terminal velocity as reported by Sharma and Gupta, 1989. The rainfall simulator was equipped with a computer system in order to control the solenoid valves, pump flow rate, and an oscillating screen. The pump is positive displacement type and the flow rate was controlled by adjusting the pump rotational speed, which insured high control on the flow rate and the repeatability of the same

flow rate. Before running the rainfall simulator for the experiment, a priming system was used to remove all the air from the pipe system. The raindrops were generated using flat-cut hypodermic needles. These needles were fixed on a metallic frame organized in 18 rows. Each row included 50 needles, which were fixed on a disc-type water distributor. Below the needles, the oscillating screen was fixed to distribute the rainfall evenly **(Fig. 3.1)**. The rainfall simulator was calibrated for the rainfall spatial distribution on the experimental area (2.3 m^2), and to determine the relationship between the flow rate and rainfall intensity.

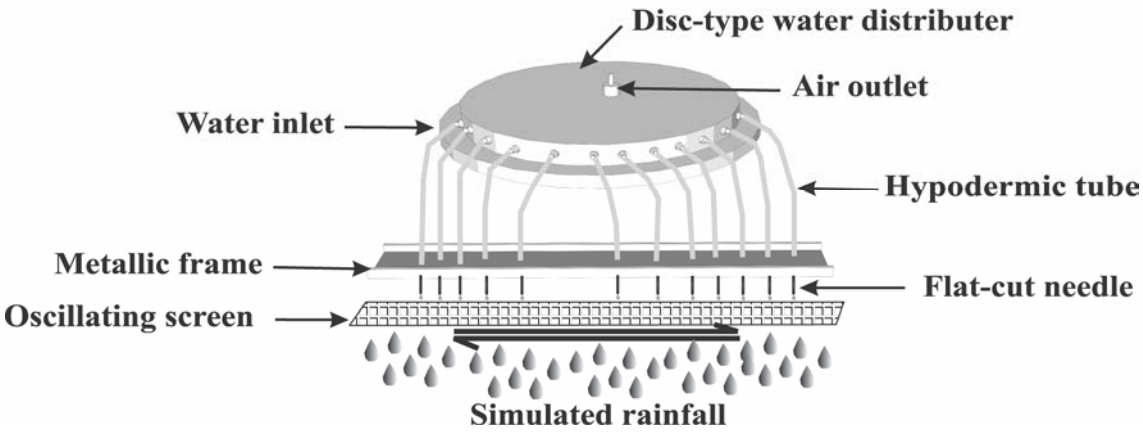

Fig. 3.1. Schematic view of the dripper-type rainfall simulator.

3.2.2. Rainfall characterization

The rainfall erosivity was observed using the piezoelectric force transducer method. This method depends on the ability of crystal plate to produce electric charge when it receives force. Two sensors were used to measure the kinetic energy (KE, mJ) and drop size distribution (DSD, mm). The two sensors were modified from the RAINCAP® precipitation sensor, manufactured by Vaisala, Finland **(Fig. 3.2)**. The precipitation sensor measurement was based on the acoustic detection of the impact of individual raindrops (Salmi and Ikonen, 2005). The signals from the impact are proportional the raindrops' mass. The sensor was constructed from a piezoelectric detector (crystalline quartz) covered by a stainless steel shell used to protect the sensing element. A noise filtering technique was adopted to eliminate signals from other sources than the initial

raindrop impact. Different electronics systems were used to filter, amplify, digitize, and analyze the signals produced by the sensing elements prior to the signals logging. The sensor consisted of piezoelectric disc fixed on a top of plastic body; below the plastic body there are electronics parts and both of them are covered by the stainless shell.

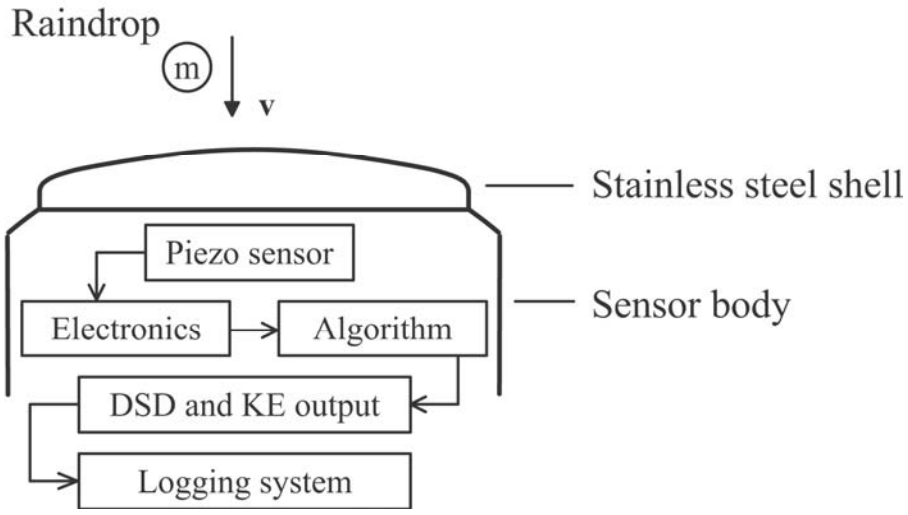

Fig. 3.2. Schematic view of the piezoelectric transducer components.

Two sensors were used to measure the drop size distribution (DSD*)* and the kinetic energy (KE*)* of the simulated rainfall. The sensors were calibrated using controlled drop size falling from a14 m height and the velocity of each drop size was measured using an optical method, was highly correlated with the Gunn and Kinzer (1949) function (Salmi and Elomaa, 2007). The sensors were also compared with Joss-Waldvogel RD-69 disdrometer to measure the DSD under the natural rainfall conditions in Finland, and showed significant agreement for the raindrop size greater that 0.80 mm (Pohjola et al., 2008). The sensor's signal was divided to measure the raindrops' size and kinetic energy in eight size classes normalized to the mean drop diameter **(Table 3.2)**. In other words, each class gave the number of drops or kinetic energy received (depending on the sensor configurations) within the range of the class size as shown on **Table 3.2**. According to Pohjola et al. (2008), when the drop has a diameter higher than the mean it will give higher weight in number of drops and/or kinetic energy. The KE sensor was also validated under simulated rainfall and the sensor output was compared with the calculated KE using rainfall DSD and empirically estimated velocity, which gave statistically significant correlation under different rainfall intensities. The signals from

the two sensors were logged in two notebook computers using the RS-232 serial interface and data logging software to store the data in the computers used as a data logger. The rainfall intensity was measured using a tipping-bucket rain gauge (Davis rain collector II, CA, USA) with 0.2-mm rainfall depth accuracy. The rain gauge was attached to event data logger (HOBO event; Onset Computer Corp., MA, USA) with 0.5-s time recording accuracy. The output from the two sensors **(Fig. 3.2)** was then used to calculate the rainfall erosivity parameters **(Table 3.1)**. The momentum (M) was calculated from the KE and raindrops' mass using the following equation:

$$M = \sqrt{KE \times 2m} \qquad (3.1)$$

where M is the momentum (kg m s^{-1}), KE is the kinetic energy (J), and m is the drop mass (kg), which was determined from the drop diameter (class mean size; **Table 3.2**) and the number of the raindrops in the class measured by the DSD sensor.

Table 3.2. Drop size classes of the piezoelectric sensor.

Class ID	Drop size range (mm)	Weighted drop size (mm)
1	0.80-1.12	1.00
2	1.12-1.40	1.25
3	1.40-1.79	1.60
4	1.79-2.24	2.00
5	2.24-2.89	2.50
6	2.89-3.59	3.20
7	3.59-4.49	4.00
8	> 4.49	5.00

3.2.3. Splash experiments

The splash-cups were prepared using PVC pipe-connectors with a diameter of 10 cm and height of 20 cm. At a height of 10 cm, a metal screen was fixed to the cup using rubber gum and then filter paper was placed on top of the screen and the cup was filled with silty clay loam soil **(Table 3.3)** collected from the Tohaku area, Tottori prefecture, Japan. The soil had been air dried in a greenhouse and then crushed and sieved through 2 mm mesh. Prior to the simulated rainfall experiments, the soil again dried, this time in

an oven at105ºC for 24 hours. The bulk density of all cups was 1.10 ± 0.01 g cm^{-3}. The cups were then exposed for the simulated rainfall to different durations depending on the rainfall intensity level. The rainfall durations ranged from 18 to 1.32 minute for 10 to 100 mm h^{-1} rainfall intensity level, respectively. The rainfall depth was kept at a minimum to avoid surface ponds, which work to reduce the rainfall energy striking the soil surface. The splash was measured by subtracting the total weight of the each splash cup before the application of the simulated rainfall and after the rainfall simulation and oven dried under 105ºC for 24 hours. The soil surface also examined for hardness due to the drop impact using a Push-cone penetrometer (Push-cone, DIK-5553, Daiki, Japan) before and after the rainfall simulation.

Table 3.3. Soil particle size distribution.

Size class	Particle diameter (mm)[a]	Weight (%)
Fine sand	0.2-0.02	8.24
Silt	0.02-0.002	61.78
Clay	< 0.002	29.98
D_{50}	0.0045	…

[a] The particle size analysis was performed using laser method.

3.3. Results and Discussion

3.3.1. Simulated rainfall characteristics

The characteristics of the simulated rainfall were measured using two piezoelectric sensors in order to measure the drop size distribution (*DSD*) and the kinetic energy at rainfall intensity (*I*) ranging from 10 to 100 mm h^{-1}. The relationship between the median drop size (D_{50}) and the rainfall intensity is shown in **Fig. 3.3** This relationship was also compared with data obtained under the natural rainfall reported by Laws and Parson (1943), Zanchi and Torri (1980), and Van Dijk et al., (2002). The simulated rainfall had a D_{50} that is greater than the natural rainfall under these different rainfall intensities compared with the published relationships **(Fig. 3.3)**. Van Dijik et al. (2002) reported that the relationship between the *I* and D_{50} can be described as a power relationship, as shown in equation (2).

$$D_{50} = \alpha \ I^{\beta} \qquad (3.2)$$

where I is the rainfall intensity (mm h^{-1}), α and β are empirical parameters ranging from 0.8 to 1.23 and from 0.123 to 0.292, respectively.

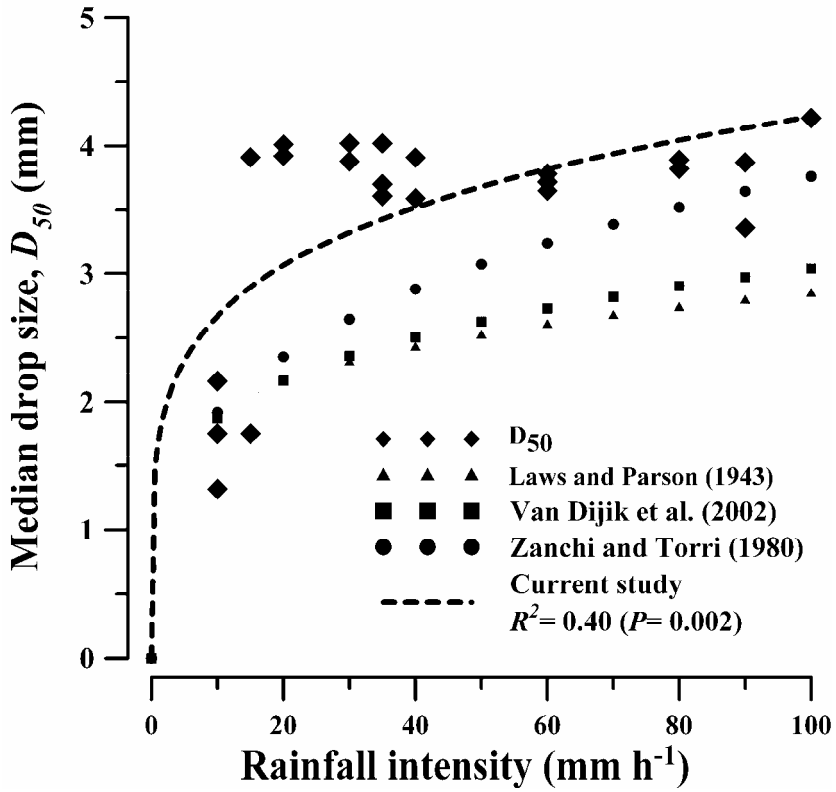

Fig. 3.3. Relationship between the median drop size and the rainfall intensity compare with the natural rainfall relationships.

The simulated rainfall followed the same relationship and the R^2 was 0.4 (P=0.002) where α and β were 1.67 and 0.20, respectively. Under natural rainfall, the relationship between the D_{50} and rainfall intensity takes on different patterns depending on the geographical location. Several researchers have reported that the D_{50} increases with the increase of the rainfall intensity until a certain rainfall intensity threshold and then stabilizes or decreases (Hudson, 1963; Van Dijk et al., 2002). The simulated rainfall seems to follow the increasing-stabilizing trend. However, the *DSD* information supported that there is an increase in the small drops (<2 mm) number as the rainfall increases **(Fig. 3.4)**. The *DSD* showed that the there is an increase in the large drop size (>2 mm) until the rainfall intensity approaches 30 mm h^{-1} and then a decrease with the increase of rainfall intensity. The first increase in the content of large drops is proportional to the increase of the flow rate applied to the dripper. However, with the

increase of the flow rate the water started to flow out of the dripper as a jet and formed droplets similar to a sprayer.

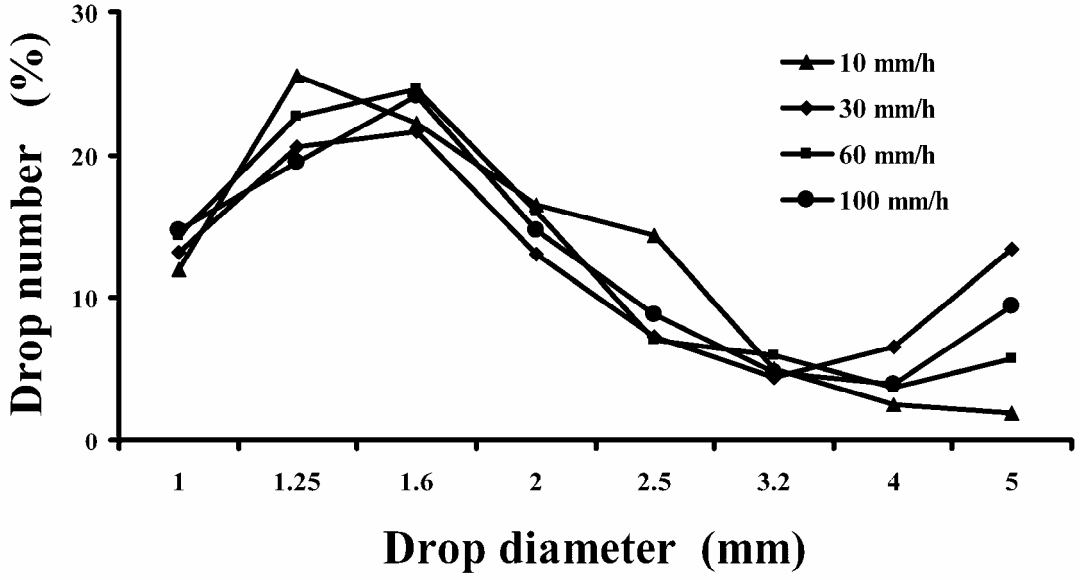

Fig. 3.4. Drop size distribution obtained under different rainfall intensities.

These results have determined the relationship between the rainfall intensity and the erosivity indices (KE, M). The KE (J m^{-2} mm^{-1}) tended to increase with the rainfall until it reached 30 mm h^{-1} and then started to decrease with the increase of the rainfall intensity **(Fig. 3.5)**. The same trend was found in the relationship between M, KE_C, and MD and the rainfall intensity. Rainfall kinetic energy is widely used for natural rainfall erosivity while the other indices are rarely used under the natural rainfall. The simulated rainfall *KE-I* relationship was compared with published relationships at different climate zones **(Fig. 3.5)**. The simulated rainfall *KE* was always less than the reported natural rainfall KE under different rainfall intensities. The rainfall erosivity indices depend on the raindrop mass and velocity. As was shown in **Fig. 3.3**, the D_{50} of the simulated rainfall was higher than the natural rainfall. This emphasizes the effect of the fall height on the simulated rainfall erosivity. The fall height is a major factor affecting *I- KE* relationships in the dripper type rainfall simulator, because the droplets produced fall only by the force of gravity. This condition is different from the nozzle-type rainfall simulator where the droplets gain speed from the pressure of the nozzle orifice (Salles and Poesen, 2000). Also, this result suggests that there is a certain threshold that must

be considered in order to simulate rainfall that has similar properties to natural rainfall or at least a similar *KE-I* pattern.

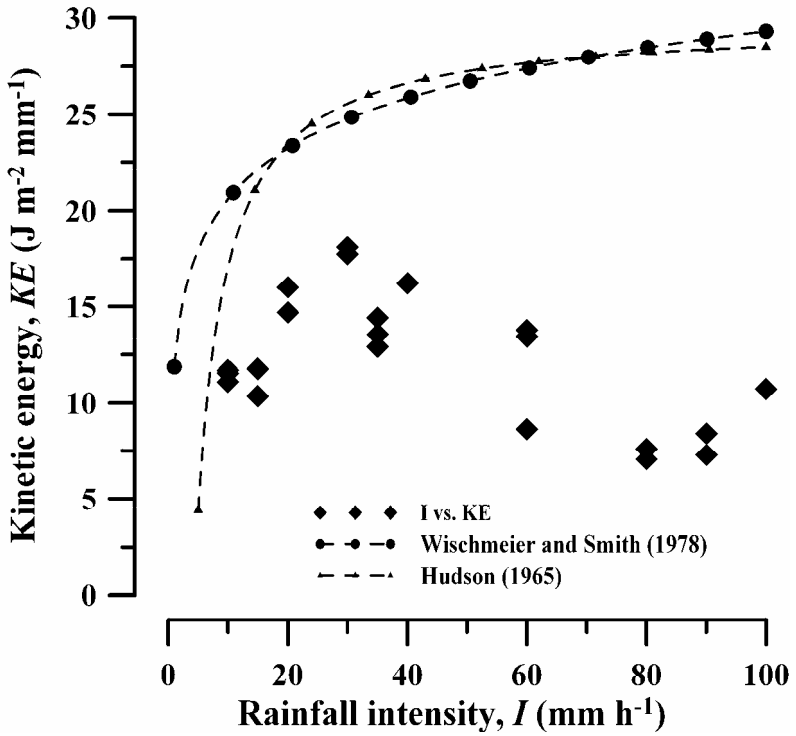

Fig. 3.5. Relationship between the rainfall energy and the rainfall intensity.

3.3.2. Impact of rainfall characteristics on soil splash

The relationship between kinetic energy and rainfall intensity (*KE-I* relationship) was compared with the relationship between soil splash and the rainfall intensity (D_s-*I* relationship) **(Fig. 3.6)**. The two relationships followed a similar trend, which emphasize the big role of the *KE-I* relationship in determining the D_s-*I* relationship. The rainfall intensity has been used as a rainfall erosivity indicator, especially under natural rainfall conditions, without regard to the relationship between the rainfall intensity and the *KE* and the other erosivity indices. In this sense, the *I-KE* relationship varies according to location and also due to rainfall simulation type. Subsequently, it can result in a misleading the D_s-*I* relationship and distort splash prediction. Particularly, the simulated rainfall in this study was recognized to have two phases; phase I, rainfall intensity up to 30 mm h^{-1}, and phase II, rainfall intensity higher than 30 mm h^{-1}. The relationship between the rainfall intensity, erosivity indices, and soil splash in the two phases are shown in **Table 3.4**. In phase I, the relationships between rainfall intensity

and the erosivity indices were statistically significant positive relationships, where in phase II there were negative relationships. These results indicate that there is a drop in the rainfall erosivity when the rainfall is higher than 30 mm h^{-1}. The decrease in natural rainfall energy with rainfall intensity increase was reported before by Hudson (1963). This indicates that this phenomenon can simulate natural rainfall condition. However, the dominant concept for the *KE-I* relationships that are follow a logarithmic relationship (Wischmeier and Smith, 1958; Zanchi and Torri, 1980; Kinnell, 1981). There are other relationships including the power and exponential relationships suggested by other researchers for different geographic locations (Van Dijk et al., 2002; Salles et al., 2002). In this regard, the *KE-I* relationship can also vary between rainfall simulators and the D_s-*I* relationship will be modified according to the *KE-I* relationship. The same relationship between the *KE* and *I* can be used in the other erosivity indices (KE_C, *M*, and *MD*) which follow the same two-phases trend.

The relationship between the soil splash and rainfall intensity was also varied with the different phases. In phase I the correlation coefficient between the *I* and D_s was 0.94 (P<0.001), indicating that the soil splash increased with the rainfall intensity increase. This result is in agreement with several reported results under the natural rainfall (Morgan, 1978; Sharifah Mastura et al., 2003) and simulated rainfall (Andrew et al., 1968). In phase II, the D_s was negatively correlated to the rainfall intensity where the correlation coefficient was -0.97 (P<0.001). This relationship can be attributed to the aforementioned decrease in the rainfall energy when the rainfall intensity approaches 30 mm h^{-1}.

3.3.3. Erosivity indices and soil splash relationship

Four raindrop erosivity indices (*KE*, KE_C, *M*, and *MD*) were related to the soil splash **(Fig. 3.7)**. The correlation coefficients for the four indices were statistically significant at the 0.01 level of probability **(Fig. 3.7)**. The soil splash was found to increase with the four indices of raindrop erosivity. The increasing functions of the soil splash varied between the different indices. The relationships between the soil splash and raindrop erosivity indices were investigated using four major functions; linear, power, logarithmic, and exponential functions **(Table 3.5)**. The most significant function was found to vary between indices; however, the exponential function has a higher coefficient of determination among the four raindrop indices. Generally, the relationship between soil splash and erosivity indices can be described as a power relationship

(Salles et al., 2000, Mouzai and Bouhadef, 2003). However, some researchers reported other relationships such as a linear relationship (Andrew et al., 1968) and exponential (Mouzai and Bouhadef, 2003) in order to describe the relationship between soil splash and raindrop erosivity indices.

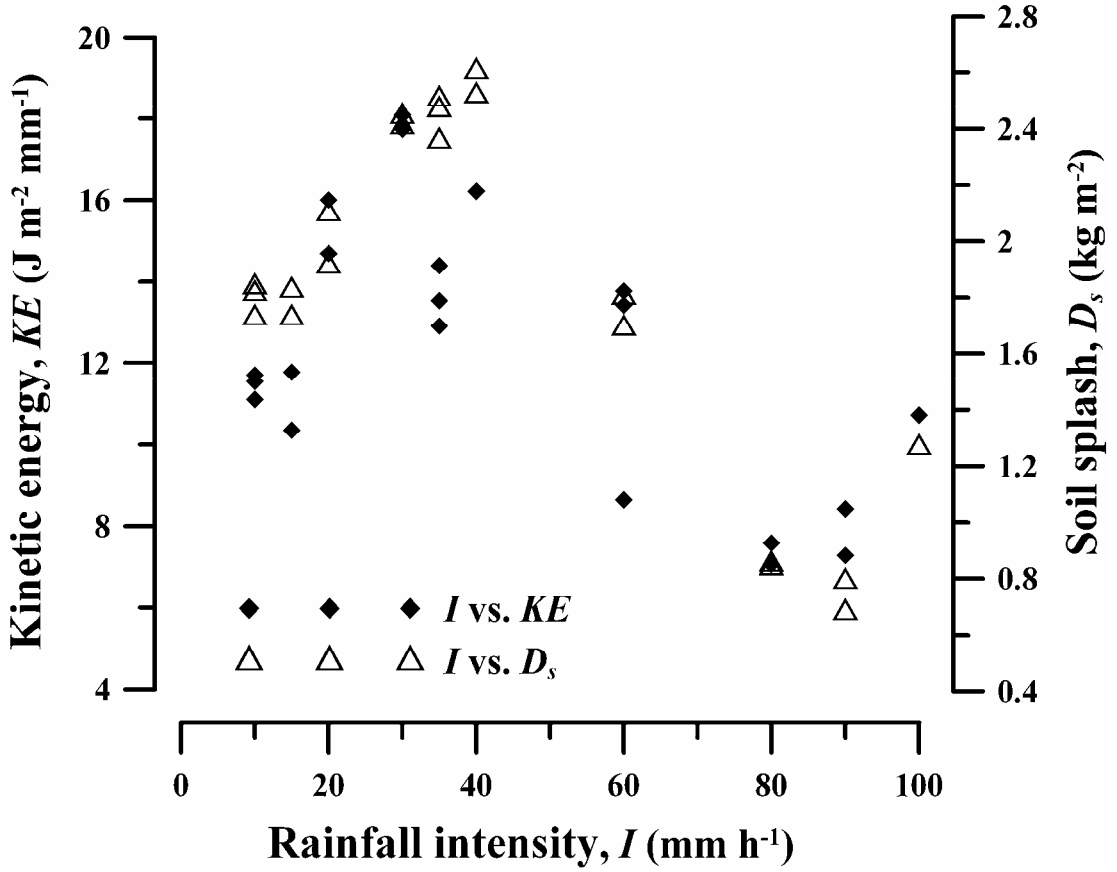

Fig. 3.6. Comparison between the rainfall intensity- kinetic energy relationship and the rainfall intensity-soil splash relationship.

Table 3.4. Correlation coefficient between rainfall intensity, erosivity indices and sediment generation under the two rainfall intensity phases.

	Phase I (rainfall intensity under 30 mm h^{-1})				Phase II (Rainfall intensity over 30 mm h^{-1})			
Erosivity Index	***KE***	***KE_C***	***M***	***MD***	***KE***	***KE_C***	***M***	***MD***
Rainfall Intensity (mm h^{-1})	$0.93_{(<0.001)}$	$0.97_{(<0.001)}$	$0.87_{(0.002)}$	$0.97_{(<0.001)}$	$-0.82_{(<0.001)}$	$-0.75_{(0.003)}$	$-0.84_{(<0.001)}$	$-0.76_{(0.002)}$
Soil splash (kg m^{-2})	$0.89_{(0.001)}$	$0.92_{(<0.001)}$	$0.85_{(0.003)}$	$0.92_{(<0.001)}$	$0.89_{(<0.001)}$	$0.85_{(<0.001)}$	$0.90_{(<0.001)}$	$0.86_{(<0.001)}$

§The subscript is the *P*-value.

Table 3.5. Coefficient of determination (R^2) between erosivity indices and splash erosion.

Erosivity indices	***I***	***KE***	***KE_C***	***M***	***MD***
Linear	$0.88_{(<0.001)}$	$0.80_{(0.001)}$	$0.85_{(<0.001)}$	$0.73_{(0.004)}$	$0.84_{(<0.001)}$
Power	$0.80_{(<0.001)}$	$0.78_{(0.002)}$	$0.81_{(0.001)}$	$0.72_{(0.004)}$	$0.81_{(<0.001)}$
Logarithmic	$0.78_{(0.002)}$	$0.76_{(0.002)}$	$0.79_{(0.001)}$	$0.69_{(0.005)}$	$0.79_{(0.001)}$
Exponential	$0.89_{(<0.001)}$	$0.81_{(<0.001)}$	$0.86_{(<0.001)}$	$0.75_{(0.003)}$	$0.86_{(<0.001)}$

§The subscript is the *P*-value.

3.3.4. Rainfall energy dissipation

The rainfall energy under cohesive soil conditions can be divided into horizontal effects (soil splash generation) and vertical effects (soil compaction), unlike non-cohesive soil such as sandy soil **(Fig 3.8)**. The changes in soil hardness (compaction ratio) were measured in this study in order to investigate the amount of energy that diverted into surface compaction. However, in this study no significant relationships between the raindrop erosivity indices and the surface compaction were obtained. This result can possibly be attributed to the methodology used for soil compaction measurement, and that the splash-cup was too small for several penetrometer samplings.

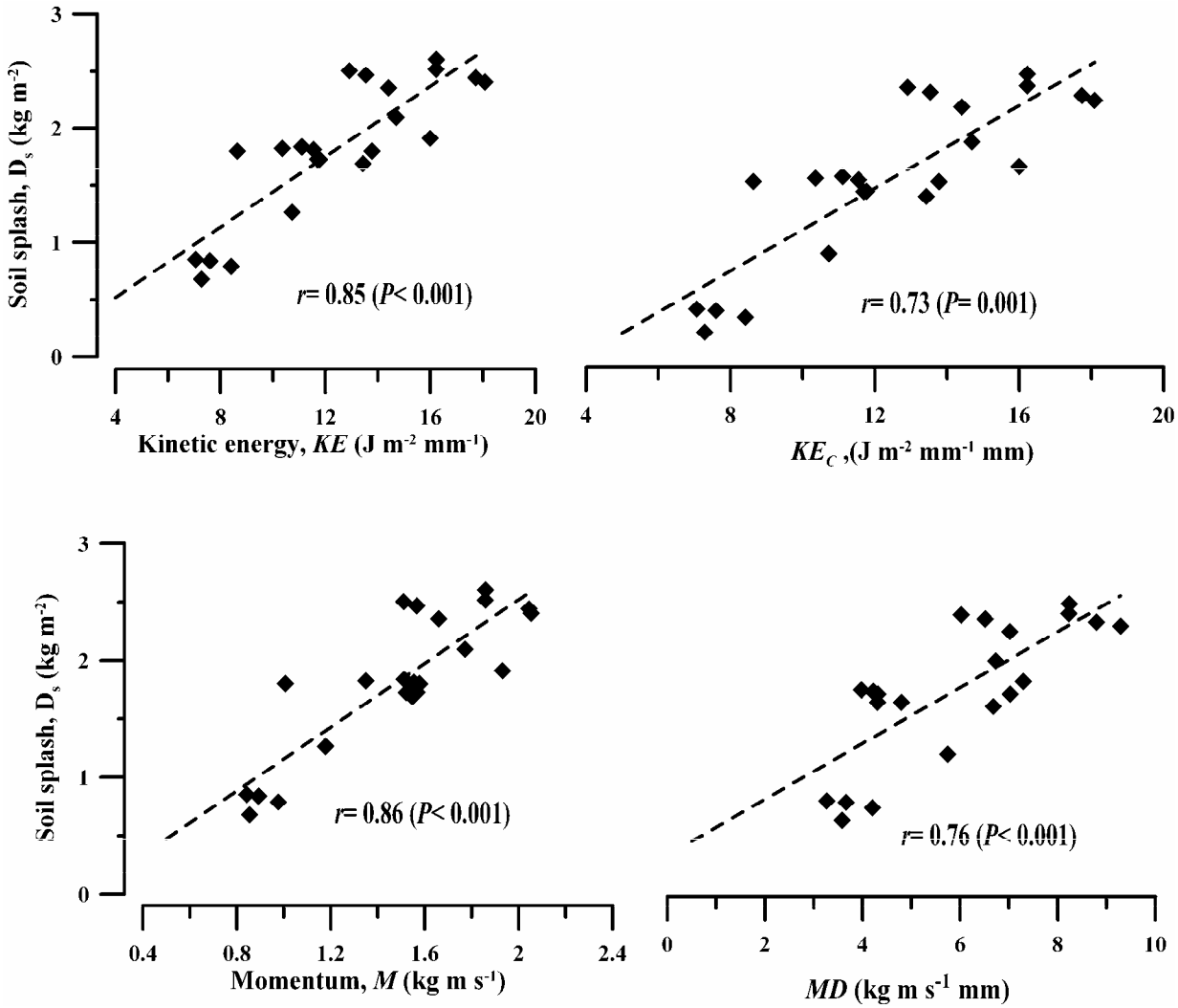

Fig. 3.7. Soil splash generation as function of the raindrop erosivity indices obtained under rainfall intensity ranged from 10 to 100 mm h^{-1}.

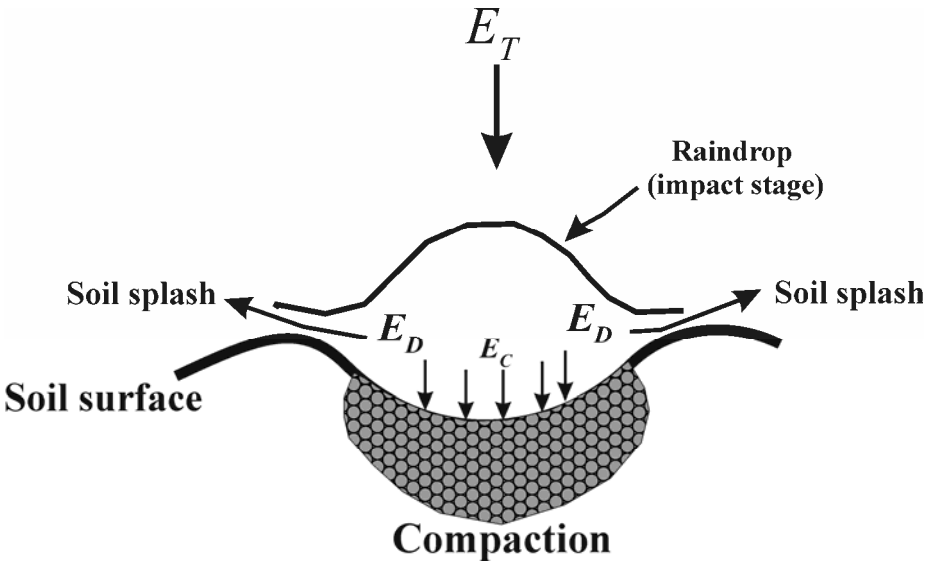

Fig. 3.8. Schematic illustration of raindrop energy dissipation; E_T, E_D, and E_C are total raindrop energy, energy for soil detachment, and energy for soil compaction, respectively.

3.4. Conclusions

This study attempted to characterize the simulated rainfall generated from a dripper-type rainfall simulator by using a piezoelectric transducer and the characteristics impact on soil splash. Two piezoelectric transducers were used to measure the simulated rainfall drop size distribution and kinetic energy at different rainfall intensities ranging between 10-100 mm h^{-1}. Splash cup experiments were also used to investigate the effect of rainfall characteristics on soil splash. The rainfall characteristics displayed that the dripper-type rainfall simulator produced a wide-spectrum of rainfall drop size similar to that found in natural rainfall, and this spectrum is changed with the rainfall intensity. However, the relationship between the erosivity indices and the rainfall intensity was unique and differed from natural rainfall relationships. The kinetic energy tended to increase with the rainfall intensity until 30 mm h^{-1} and started to decrease under the rainfall intensities higher that 30 mm h^{-1}. The phase I exhibited a trend similar to the dominant reported trends of natural rainfall. The results suggested that the dripper-type rainfall simulator has a threshold limit. This threshold must be considered in order to simulate rainfall similar to natural rainfall. Also the D_s-I relationship is highly dependent on the relationship between the rainfall erosivity and the rainfall intensity, which could vary due to rainfall simulator type and generate different results and

sometimes contradicts trends depending on the rainfall characteristics. The soil splash was found to be highly statistically correlated with the erosivity indices, regardless of the rainfall intensity. In this regard, the erosivity indices (Kinetic energy and momentum) can be used effectively as independent soil splash predictors regardless of the rainfall intensity.

CHAPTER 4:

Potential of low cost close-range photogrammetry system in soil microtopography quantification

4.1. Introduction

Soil microtopography or roughness/microrelief is a dynamic soil property which affects most of the soil-surface and water interaction processes. Soil microtopography seems to control many transfer processes on and across the surface boundary (Huange and Bradford, 1990), such as infiltration (Steichen, 1984; Govers et al., 2000), runoff initiation (Darboux and Huang, 2005), soil erosion (Römkens et al., 2001), and modifying flow velocities (Giménez and Gover, 2001). Although the effects of soil microtopography are well recognized, there are a relatively small number of published papers on this subject. Huange and Bradford (1990) have attributed the small number of publications on soil microtopography mainly to laborious field techniques that produced only low-resolution data sets. Soil microtopography at a plot- scale level (≤ 1 m^2) has a direct effect on most of the soil-surface and water interaction processes. Accordingly, it has received increasing attention from researchers with regard to measurement techniques, their accuracy and interpretation. The soil microtopography a sequence of aggregate and voids (pits), and using low-resolution data sets means some these features are ignored, which will affect interpretation and the reliability of these data (Jester and Klik, 2005).

There are several hydrological parameters that can be extracted from the soil microtopography data at the plot-scale, and which have great influence on the water flow on and into the soil. These parameters include soil roughness indices, depressional storage capacity (*DSC*), and rills and micro-rills development.

The soil roughness indices have been used extensively in order to describe the soil surface conditions, and there are numerous roughness indices in the literature. However, Huang and Bradford (1990) argued that roughness cannot be completely described by a single index. Govers *et al*. (2000) reported that a single index is never capable of quantifying the variance (reflecting the absolute variation in height) and the correlation length (describing the distance over which spatial autocorrelation occurs). The same authors also indicated that most existing roughness indices indeed describe either the variance or the correlation length.

The depressional storage capacity (DSC) is an important factor derived from the soil microtopography data, which affects the runoff initiation and water flow (Darboux et al., 2002), and the infiltrated depth of the rain water (Guzha, 2004). On the other hand, rills and micro-rills are important soil surface features due to their activeness in water, sediment, and sediment absorbed materials transportation. Moreover, and particularly in dray areas and agricultural lands, surface sediment transport and associated materials from hillslope to water bodies is channeled mainly through rill networks (Brunton and Bryan, 2000).

Measurement techniques used for soil microtopography were developed in the early 1960s using microrelief meters. In this method a frame consisting of pins standing on the soil surface was compared with a calibrated background to give the relative heights for each pin (Kuipers 1957; Burwell et al., 1963; Allmaras et al., 1966). Another relatively simple method is the chain method, where a chain of a given length (L1) equal to the horizontal distance, is placed on the soil surface (L2). The horizontal distance covered by L2 decreases as the roughness increases (Saleh, 1993; Govers *et al*. 2000). However, the microrelief meter has received increasing attention lately after the introduction of digital image processing for pin measurements (Wanger and Yu, 1991) and data logging for pin heights, by uses a height encoder connected to a rod which lowers 40 aluminum pins until they touch the soil surface. Each pin has a separate switch connected to a channel in a data logger (Donald W. Fryrear, personal communication).

Currently the non-contact techniques such as laser scanning (Huang *et al*., 1988; Helming *et al*., 1998; Arvidsson and Bölenius, 2006) and photogrammetry (Jeschke, 1990; Taconet and Ciarletti, 2007) are preferred by researchers for saving time and labor, and for the ability of these methods to construct a three dimensional (3D) vision of the soil surface. Digital photogrammetry is a modified version of the analog and analytical photogrammetry, which provides and enables non-photogammetrist to use this rapid and inexpensive method compared with laser-scanner and other methods (Chandler, 1999; Lascelles et al., 2002; Rieke-Zapp and Nearing, 2005). Other recent procedures include infrared, ultrasonic and radar. But these need further research and refinement with regard to their applicability and accuracy for soil microtopography measurement (Jester and Klik, 2005).

The main advantage of the digital photogrammetry is the time involved (less than one second) to acquire ready images for DEM generation (stereo images), compared with

the long time required for laser scanning. Digital close range photogrammetry is the part of photogrammetry which deals with high precision measurement at a relatively small distance between the camera and the object. These advantages of the close range photogrammetry qualify it to play important role in the acquisition of the soil DEM at the plot-scale level ($\leq$ 1 m^2) compared with the other techniques. The close range photogrammetry is based on stereo-pair images of the soil surface with relatively short height. In most cases, the camera or cameras are used vertically or obliquely above the soil surface, and then two images or more with sufficient overlap are acquired. The space between the two camera's positions depends on several factors including: the desired DEM resolution, applicable camera height, software capacity, and resolution of the camera sensor. There are two photogrammetric techniques for DEM generation: manual and automated digital photogrammetry (Hancock and Willgoose, 2001). The difference between the two systems is mainly on the method of defining the homologous points on the stereo-pairs images. The consumer market, nowadays, contains various types of digital cameras with high-resolution and reasonable prices that can be used for soil microtopography measurement at plot-scale. However, the reliability of the DEM produced by the consumer-grade camera to quantify the soil microtopography at the plot-scale has not yet been well investigated.

The objectives of this study were: to generate DEM for the simulated soil surface using close range photogrammetry, to quantify the simulated soil surface microtopography using a consumer-grade camera, and to assess the accuracy of the DEM generated by consumer-grade cameras in comparison with the direct measurement method. In order to fulfill these objectives soil surfaces with different roughness were fabricated using cement, gypsum, and gravel materials.

4.2 Materials and Methods

4.2.1 Soil surface simulation

Soil surfaces with different roughness were constructed using fabricated gypsum surfaces with different aggregate conditions. The surfaces were: smooth (SM), low roughness (LR), medium roughness (MR), high roughness (HR), and rilled (RL). The first four were generated using four gravel sizes: 5, 10, 20, and 30 mm; while the fifth was generated using 30 mm gravel size arranged in such a way as to simulate micro-rills formation. A square wooden tray measuring 300 mm x 300 mm x 30 mm (depth) was

used as a frame for each of the five surfaces. The bottom of the wooden tray was covered with a 15 mm cement layer, then the gravels were distributed randomly on the cement layer **(Fig. 4.1)**. The trays were left at room temperature for 24 hours to dry in order to avoid changes in the gravel position. A thin layer of gypsum was then applied to cover the gravels and the cement layer. The advantages of the gypsum are to insure that the surface will not be affected by the contact methods (pin-microrelief meter) measurement, to smooth the gravel surface, and to fill the cavities between the gravel and the cement surface.

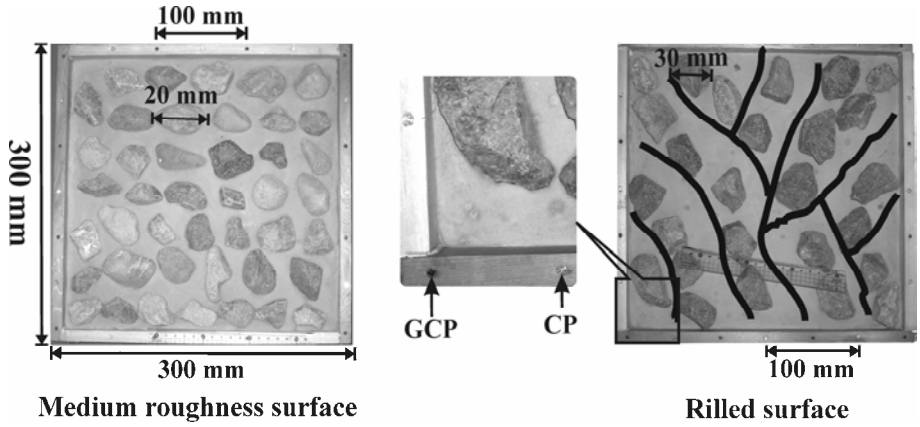

Fig. 4.1. Fabricated gypsum surfaces, the ground control points (GCP), and the check points (CP).

The five surfaces were then sealed with a waxy material to protect the surfaces and to create an impermeable surface. The tray borders were equipped with 12 silver colored screws known as a ground control points (GCP) for DEM generation, and another set of 12 black colored screws known as check points (CP) for DEM quality validation. The distances of GCP and CP were measured from a reference point, defined as the left-bottom corner of each tray with accuracy equal to 0.001 mm using digital caliper. The CPs were used to validate the original accuracy of the DEM before any corrections by comparing the directly measured CPs with the photogrammetricaly estimated CPs. The bottom left corner was set as reference point (zero point) where the gypsum surfaces elevation and spatial coordinates' dimension were based on this point. The value of the x, y, and z coordinates at this point was arbitrarily identified as 1000 mm.

4.2.2 Elevation measurements

The elevation of the gypsum surfaces was measured using two methods:

4.2.2.1 Pin-microrelief meter method (PM)

The pin-microrelief meter **(Fig. 4.2)** was constructed using a wooden frame and metal pins similar to that described by Kuipers (1957). It consisted of a vertical aluminum frame, which was fixed to a wooden vertical frame, which had 30 movable pins for recording the elevation (microrelief) of the gypsum surface **(Fig. 4.2)**. The pins could move up and down through holes constructed on the top and bottom rims of the vertical frame. The vertical frame had a graph paper background marked in mm scale **(Fig. 4.2)**. The distance between the two rims was 60 mm. Each pin had a red mark at the bottom rim, which coincided with zero elevation, if the pin touched a flat surface. The red mark will read a value higher than zero when the pins touch an elevated surface. Another horizontal (300 x 300 mm) quadratic aluminum frame was used to adjust the pins measurements in the x-and y-directions. The quadratic aluminum frame has the same dimensions as the gypsum plots. This frame was divided into 10 mm x 10 mm squares, using thin red strings on the x-direction and yellow strings on the y-direction **(Fig. 4.2)**. The strings were tied to the aluminum frame. The squares could be identified by x and y directions as: $(x_1,y_1),\ldots,(x_{30}, y_{30})$. A total of 900 squares were contained by the horizontal frame. Before we started the measurement on gypsum surface, the pin-microrelief meter was used to take a reading on the reference point and all the measurements on the gypsum surface were based on this reading. Thirty microrelief readings were made with the pins touching the center of each square in the horizontal row (x-direction). The sampling was then shifted to the next row by sliding the wooden frame along the y-direction of the quadratic frame. The process was repeated until all 900 squares were sampled for the gypsum surface. The same procedures were repeated for other the fabricated soil surfaces. The x and y information of each pin measurement (z-direction) were used to construct the DEM using the pin-microrelief meter method. The pin-microrelief meter accuracy is dependent on the accuracy of the graph paper background which was 1.0 mm, while the spacing on the x-and y-directions was 10 mm.

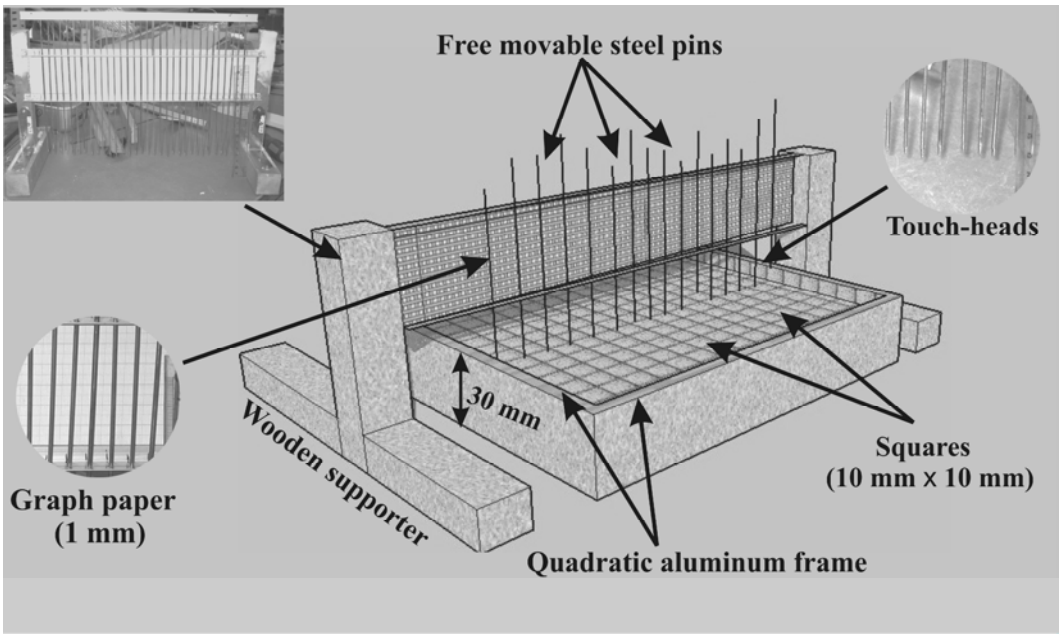

Fig. 4.2. Schematic diagrams showing the pin-microrelief meter.

4.2.2.2 Photogrammetry method (PHM)

The photogrammetry measurement consists of two steps:

i) The five gypsum surfaces were photographed using a Canon® Power-Shot50 digital camera, which is a consumer-grade camera commonly found in electronics shops. The camera is a non-metric camera, the interior properties and lens distortion parameters are unknown, with focal length equal to 7.1 mm and CCD (charge-coupled device) size was equal to 2592x 1944 pixels in x and y directions, respectively. The CCD pixel size was approximately 2.7 μm in x and y directions. Two images were captured; one each from the left and right side **(Fig. 4.3)**. The camera was located vertically above the left side border to achieve the left image and then moved to the right side border of each gypsum plot to achieve the right image. The camera height was modified to capture the entire plot in a single image. The space between the left and right camera positions was adjusted based on the acquirement of full overlap gypsum plot in the left and right images; i.e. the whole image of the gypsum plot is exist on the left and right images. The lighting was provided by 12 fluorescent lamps 120 cm in size located above and beside the plot to provide homogeneous lighting. The plot was adjusted to avoid any shadow resulted from the camera or the camera's metallic supporter.

The same procedure was repeated for each gypsum surface to acquire five image-pairs (stereo-pair) ready for analysis by the photogrammetry software to generate the DEM.

The camera height and location from the reference point was measured to the nearest millimeter using measuring tape.

ii) The images were then imported to the photogrammetry system developed by Asia Air Survey Co., which is a part of the Three Dimension Erosion System located in the Arid Land Research Center, Tottori University, Japan. This system consists of two parts; 1) digital photogrammetry, and 2) erosion measurement (Abd Elbasit et al., 2008). In this study, only the photogrammetry part was used to generate the DEM from the stereo-pair images. There are two common steps in photogrammetric processing for each stereo-pair image: 1) photogrammetric triangulation, and 2) automated DEM generation.

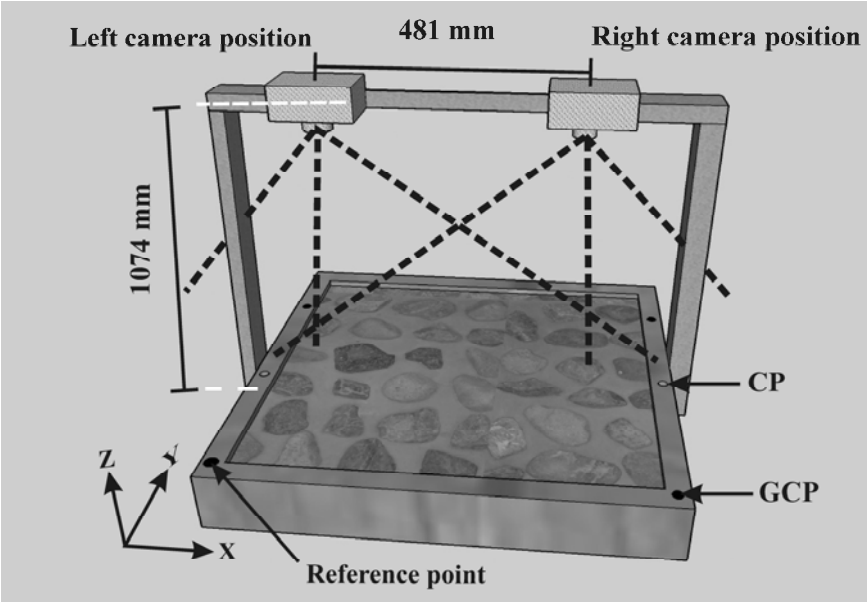

Fig. 4.3. Schematic draw showing the close range photogrammetry system using costumer-grade camera and the ground control point (GCP) and check point (CP) on the gypsum surface frame.

The first step in image processing was the image matching by adjusting the GCPs to the corresponding points of the pair of images (homologous points). The photogrammetric triangulation used a least-squares block bundle adjustment to estimate the exterior orientation parameters of the camera for each stereo-pair, then the resulting exterior and interior orientation parameters. These parameters were then used for automated extraction of elevation values during the DEM processing second phase (Stojic et al., 1998; Chandler, 1999). The output from the photogrammetry software was

scattered elevation points (point clouds) which covering the entire gypsum surface combined with coordinate system information (x-, and y-directions) for each elevation point (z-direction). The dimensions of these points on the x-, y-, and z-direction were based on the x, y and z dimensions of the GCP.

4.2.3 DEM manipulations

4.2.3.1 DEM error detection and elimination

The DEM error elimination is an essential step prior to any DEM manipulations. The errors in the DEM for the five gypsum surfaces were eliminated using the reference surface method (RSM). The (RSM) is a simple method to detect and eliminate errors before the interpolation of the scattered elevation data achieved from the photogrammetry system (Abd Elbasit, 2006). As shown in **Fig. 4.4**, we generated a smooth surface parallel to the original gypsum surface, then defined the maximum and minimum limits of the threshold, and then removed any points greater than the maximum or less than the minimum limits.

The output of RSM was a scattered elevation points for the gypsum surface. These elevation points were then interpolated by the inverse distance weighted method (IDW) in 10, 5, and 2 mm grid size form. This method is based on the assumption that the value at an unsampled point can be approximated by a distance-weighted average of sampled points occurring within a neighborhood (Woolared and Cloby, 2002; Burrough and McDonnell, 1998).

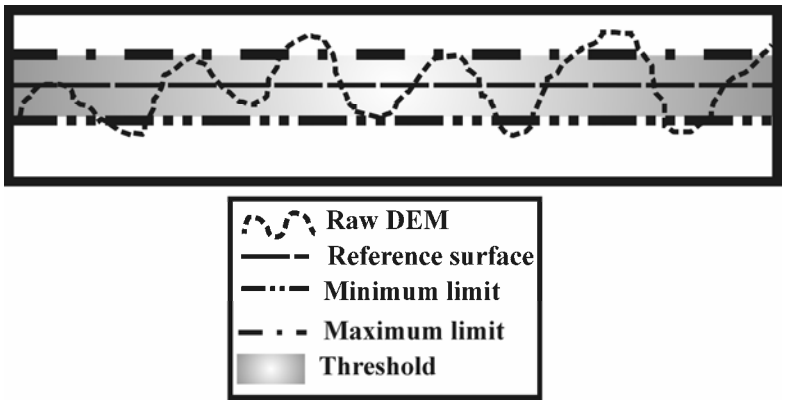

Fig. 4.4. Reference surface method (RSM) used for digital elevation model error elimination before interpolation.

After the DEM interpolation, the parametric statistical method (PSM) was used to detect and rectify the error points from the interpolated DEM (Flicísimo, 1994). This method was mainly developed for large scale DEM correction under geographical information system (GIS) environment. In this study we wrote a FORTRAN code to apply this method (PSM) to microtopography data. It involved using a simple t-test to compare every single point elevation and the mean from the four neighboring points. When the difference above is significant the mean will be used instead of the original elevation point (Flicísimo, 1994). In order to avoid the effect of the surfaces frames, the central 260 mm x 260 mm squares form the corrected DEMs were selected for the subsequent DEM analyses.

The accuracy of the generated DEM was assessed visually by constructing a 3D-vision of the different gypsum surfaces. Also, the accuracy was assessed numerically using the root mean square error (RMSE) between the measured and photogrammetrically estimated check points (CP) on the x-, y-, and z-directions separately using the following equation (Eq. 4.1):

$$RMSE = \sqrt{\frac{\sum_{i=1}^{n} (CP_{PHM(i)} - CP_{Measured(i)})^2}{n}} \qquad (4.1)$$

where:

RMSE is root mean square error in x-, y-, and z-directions;

$CP_{PHM(i)}$ *is* the photogrammetrically estimated value of the *i* check point in x-, y- and z-direction;

$CP_{measured(i)}$ is the measured value of the *i* check point in x-, y-, and z-directions using the digital caliper with 0.001 mm accuracy; and

n is the number of the check points, which was 12 points.

4.2.3.2 Roughness indices

The rectified and the interpolated DEMs by the two methods (RSM and PSM) and the pin-microrelief meter were used for surface visualization, depressions analysis, micro-rills delineation, and to calculate the roughness indices for gypsum surfaces. Three roughness indices were used to describe the gypsum surfaces roughness. These are: random roughness, RR, (Allmaras *et al*., 1966), limiting elevation difference, LD,

and limiting slope, LS, (Linden and Van Doren, 1986). These indices were calculated from the corrected DEMs to describe the surfaces' variations and correlation length. The RR was calculated as standard deviation of the elevation values as in equation (4.1).

$$RR=\left[\frac{1}{k}\sum_{i=1}^{k}(Z_i-\bar{Z})^2\right]^{1/2} \tag{4.2}$$

Where Z_i and $\bar{Z}$ are height reading at i location and the average, respectively. k is the number of elevation readings.

The LS and LD are spatial aspect roughness indices. These are based on the slope or inclination of the surface of soil clods and the average relief (elevation difference), respectively. LS and LD are based on the first–order variance or mean absolute elevation difference (ΔZ_h) as a function of lag (h) (the distance difference between each pair of point in the x-direction) as reported by Kamphorst *et al*. (2000). Linear regression analysis was used to obtain the relationship between ($1/\Delta Z_h$) and the reciprocal form of the lag distance ΔX_h as in equation (4.2) below.

$$\frac{1}{\Delta Z_h}=b\frac{1}{\Delta X_h}+a \tag{4.3}$$

$$LD=\frac{1}{a} \tag{4.4}$$

$$LS=\frac{1}{b} \tag{4.5}$$

The parameters a and b are respectively, the intercept and slope of equation (4.3), and their reciprocals are LD and LS, in equation (4.4) and (4.5) as reported by Linden and Van Doren, (1986) and Hansen et al. (1999).

4.2.3.2 Depressional storage capacity (DSC) and micro-rills delineation

The depressional storage capacity (DSC) and micro-rills are important soil surface features due to their effects on the water and sediment flow on the soil surface (Gover et al., 2000; Darboux et al., 2001; Römkens et al., 2001). The DSC on the DEM generated by PHM and PM for the various generated gypsum surfaces was determined using the Planchon and Darboux (2001) method. This method, briefly, depends on filling the

whole DEM with a thick layer of water and then removing the excess; the remaining water will be equal to the DSC of that DEM. The filled DEM is then compared with the original one to identify the depression and non-depression grids. This procedure was repeated for the DEM achieved from all different gypsum surfaces using the PHM and PM. The micro-rills were delineated using DiGeM software, version 2.0 (Conrad, 1998) combined with TAS, version 2.0.9 (Lindsay, 2005), which are freely available as shareware on the internet. Although several professional and commercial GIS software packages are already available, free download software was used in this study to emphasize the minimal cost of the DEM generation using consumer-grade digital cameras as well as the cost of DEM analysis.

4.3. Results and Discussion

4.3.1. Digital elevation model accuracy

The generated DEMs' accuracy was assessed using visual and numerical indicators. The visual method depended on the visual observation of the surface features on the 2D images of the gypsum surfaces compared with the DEM-generated from the pin-microrelief meter and photogrammetry method, under different roughness conditions. The visual interpretation for the generated DEM is very useful to assess the DEM reality; and also the surface features dislocation and spatial shifting (Butler et al., 1998). The soil surface contains different types of features including mounts, depressions and rills formation (rills can also be considered as connected depressions) **(Fig. 4.5)**. The representation of these features by the different DEM accurately can be considered as indicator for DEM accuracy and reliability **(Fig. 4.5)**. Similar mounts in **Fig. (4.5)** were indicated by a, b, and c in the 2D photos and the DEM produced different methods. The DEMs constructed by the photogrammetry system using a consumer-grade camera show high similarity with the 2D photos and the DEM constructed from the pin-microrelief meter. On the other hand, the manually delineated rills formation is quite similar to that one shown by the 2D images. Although the visual interpretation of the output DEM is very important to assess the reality, it is not comparable and non-graded measure for the DEM accuracy which suggest the needs to combine it with numerical accuracy indicator.

Thus, the DEM accuracy was assessed numerically using the RMSE of the check points **(Table 4.1)**. The RMSE is a useful measure to assess the reliability and also to quantify the accuracy of the DEM (Chandler, 1999). The RMSE was calculated from

the differences between the measured and estimated coordinate dimensions (x-direction and y-direction) and elevation (z-direction) of the check points. The CP error in the x, y and z directions were evaluated under different roughness conditions. The estimation error of the elevation was less than 1 mm for all relatively rough surfaces (LR, MR, HR, and RL). However, under the smooth surface condition the elevation error was 3.22 mm **(Table 4.1)**. The optimum DEM accuracy mainly depends on the application of the acquired DEM (Chandler, 1999). The rough surfaces provided object contrast better than the smooth surface that helped to construct successful image matching, which was also reported by Rieke-Zapp and Nearing (2005) to explain the 20% of the missing matches in each stereo-pair. The error in the x- and y-directions was higher than the error in the z-direction, which indicates a spatial shift of the DEM. The error in x- and y-direction of the surface measurement using close-range photogrammetry reached 10 mm for gravel plots measured by Butler et al. (1998). However, in the present study the error average was approximately 2 mm in the x-direction and 1.5 mm in the y-direction for the rough surfaces **(Fig. 4.6)**. This can be attributed to the developments in camera quality and precise measurement of the GCP.

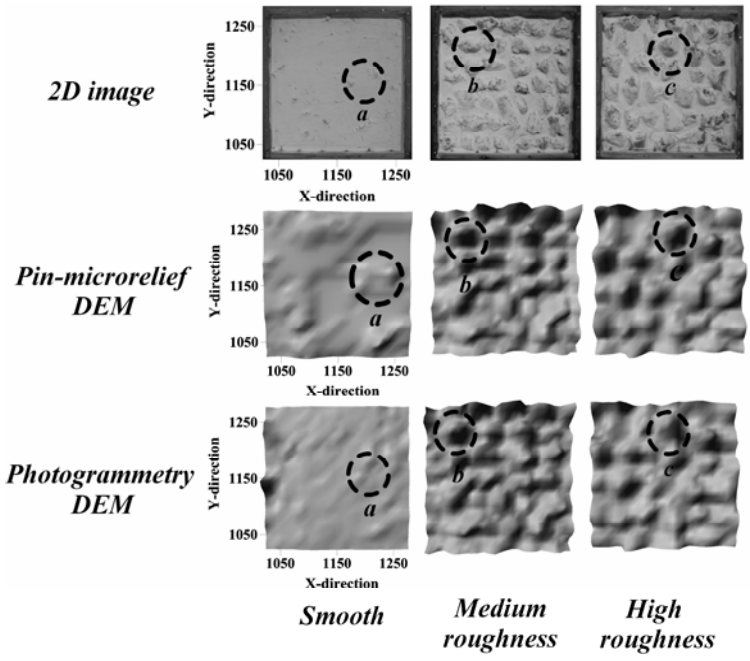

Fig. 4.5. Visual comparison between the 2D images, and the DEM generated using the pin-microrelief meter and photogrammetry methods for smooth, medium roughness and high roughness gypsum surfaces; the dashed circle is spots for comparison.

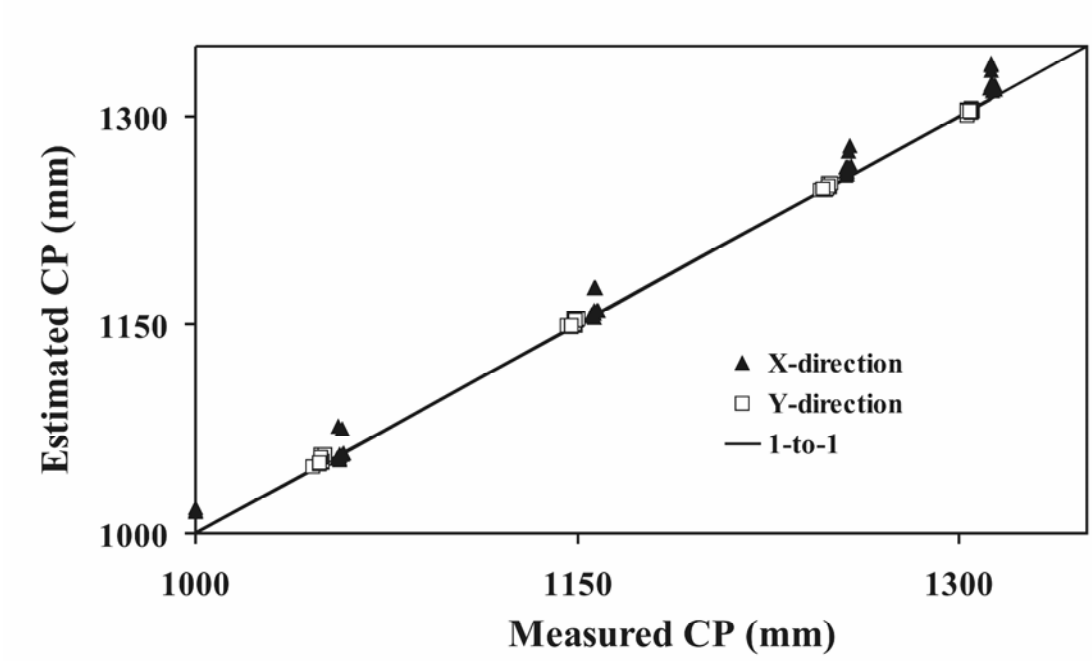

Fig. 4.6. Relationship between the measured and photogrammetricaly estimated check points in the x and y directions.

Table 4.1. Root mean square error (RMSE) for the check points in the x, y and z direction for the different gypsum surfaces.

Surface roughness level	Root Mean Square Error (mm)		
	x-direction[a]	y-direction	z-direction
Smooth	4.42	1.62	3.22
Low roughness	2.07	1.66	0.78
Medium roughness	2.15	1.34	0.86
High roughness	1.96	1.61	0.85
Rilled surface	2.15	1.46	0.80

[a] The camera positions were aligned with x-direction (see Fig. (3)).

4.3.2. Roughness indices

The RR, LS and LD were calculated for the DEM generated from the pin-microrelief meter (PM) using 10 mm grid size and the photogrammetry method using 10, 5, and 2 mm grid size **(Table 4.2)**. The roughness indices calculated from the photogrammetry method were well correlated to the roughness indices calculated from the pin-microrelief meter. However, the photogrammetry method overestimated the low roughness surfaces, and it also underestimated the surface roughness indices of the high

roughness surfaces compared with the pin-microrelief method. This over- and under-estimation can be attributed to the limitations of the pin-microrelief meter to measure surface elevations with less spatial and vertical resolution. On the other hand, the photogrammetry system produced high resolution elevation points (more than 25,000 random points on the selected surface). This dense elevation measurement for the gypsum surface can detect more features that can alter the roughness indices values. Under smooth surface condition there was small mounts constructed by five mm gravels, which can easily be ignored by the pin-microrelief meter measurement (spacing was 10 mm). Where, under rough surface conditions the underestimation can be attributed to the occurrence of depressions less than 10 mm in distance. These two effects were described before by Jester and Klik (2005) as aggregate and void which affect the roughness indices and the elevation distributions. The advantage of the photogrammetry method in assessing the soil roughness is that it can generate a sufficient resolution to derive various statistical and geostatistical indices describing the microtopography (Helming et al., 1993).

Table 4.2. Roughness indices of the gypsum surfaces generated by pin-microrelief meter and photogrammetry

Measurement method	**Pin-microrelief**			**Photogrammetry**								
Grid size (mm)	**10**			**10**			**5**			**2**		
Roughness indices	**RR**	**LD**	**LS**	**RR**	**LD**	**LS**	**RR**	**LD**	**LS**	**RR**	**LD**	**LS**
Surface roughness level[(a)]												
SM	0.79	0.60	0.05	1.34	1.96	0.19	1.43	2.22	0.17	1.39	2.17	0.18
LR	1.51	2.26	0.10	1.68	3.40	0.12	1.72	3.33	0.12	1.70	3.23	0.12
MR	3.80	15.63	4.00	3.04	11.11	1.06	3.05	10.42	0.83	3.03	10.20	0.88
HR	6.43	45.45	7.69	4.22	22.73	1.03	4.22	23.26	0.93	4.21	23.26	0.95
RL	7.45	66.67	7.69	5.58	43.48	1.56	5.59	43.48	1.45	5.58	43.48	1.52

[(a)] SM: smooth; LR, MR, and HR: low, medium, and high roughness, respectively; RR: random roughness index (mm); LD: Limiting elevation difference roughness index; LS: limiting slope roughness index.

4.3.3. Depressional storage capacity (DSC)

The DEM generated from the pin-microrelief meter and the photogrammetry methods were first analyzed to define whether the grid was a depression grid or not **(Fig. 4.7)**. In **Fig. (4.7)**, the depression grid is shown in black and the non-depression grid shown in grey. The depression maps generated from PM and PHM show relative

agreement between each other in some locations, especially under the LR, MR and HR surfaces **(Fig. 4.7)**. However, the defined depressions from the DEM generated from PHM were higher than the PM. This high number of detected depression grids under PHM compared with PM can be attributed also to the sampling resolution of PM, which is unable to detect the entire surface features less than 10 mm in size. These results were confirmed quantitatively and are shown in **Table 4.3**. The depressions area percentage (DA %) increased with the increases of the surface roughness. This is in agreement with other studies (Onsted, 1984; Hansen, 2000). It is worth it to mention here that Jester and Klik (2005) reported the decreasing of depression numbers under high roughness conditions, which can be mainly attributed to experimental plot preparation and can not be generalized to natural conditions. The effect of grid size DA% was clear in SM, LR, HR, and RL, but this effect was minimized in MR surface. The DA% achieved under MR for PHM and PM were quite similar to each other, which indicated the effect of the aggregate minimum size on selection of the optimum spacing under PM method.

The depressional storage capacity (DSC) is a function of depression area and depth. The DSC (mm) was calculated from the depth of each individual depression and then accumulated for the entire surface as shown in **Table 4.3**. The DSC clearly increase with surface roughness, and the SM, LR, MR, and HR surfaces DSC estimated from the PHM is greater than PM. These results indicate that the PHM detected more depressions compared with the PM. The relationship between surface roughness and DSC was similar under different measuring methods. The effect of the grid size and DSC can be defined as a clear inverse relation in SM, LR, and HR. The reason for obtaining high DSC with big grid size is the increase of the single grid horizontal area with grid size, which in agreement with Abedini et al. (2006). The DSC obtained under RL surface was less than the DSC obtained under HR, where as the roughness condition was similar. This result emphasized the effect of micro-rill formations on the DSC.

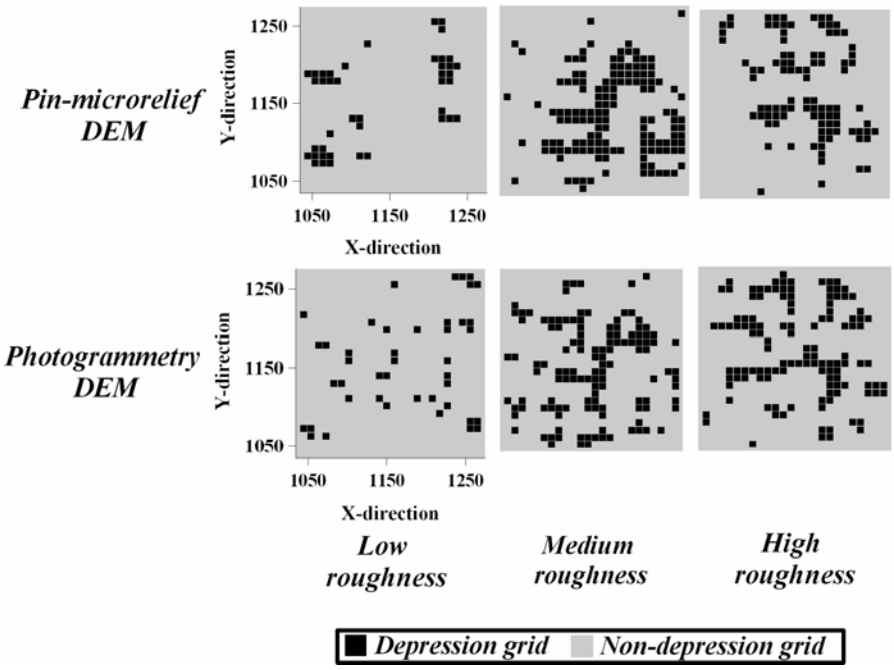

Fig. 4.7. The depressions mapping obtained under the low, medium, and high roughness conditions (Black grids stand for depression and gray grid for non-depression).

Table 4.3. Depression area percentage (DA %) and depressional storage capacity (DSC) for the gypsum surfaces under pin-microrelief meter and photogrammetry methods.

Measurement method	**Pin-microrelief**		**Photogrammetry**					
Grid size (mm)	**10**		**10**		**5**		**2**	
Depression variables	**DA%**	**DSC**	**DA%**	**DSC**	**DA%**	**DSC**	**DA%**	**DSC**
Surface roughness level [(a)]								
SM	5.33	0.06	10.65	0.56	16.05	0.47	18.35	0.42
LR	6.21	0.29	6.36	0.68	10.87	0.49	13.22	0.44
MR	21.15	0.70	18.49	0.84	21.93	0.74	21.88	1.00
HR	14.20	0.78	18.20	1.70	19.86	1.67	20.25	1.56
RL	15.83	0.50	14.64	0.81	16.68	0.80	18.17	0.77

[(a)] SM: smooth; LR, MR, and HR: low, medium, and high roughness, respectively.

4.3.4 Micro-rills delineation

The micro-rills were delineated for the DEM of RL surface obtained by the PM and the PHM with 10, 5, and 2 mm grid size **(Table 4.4)**. The visual interpretation of the two micro-rills network system shows high agreement between the two networks. The

micro-rills networks and the DEM were overlaid to insure that the delineated micro-rills networks fit the actual micro-rills visually. The number of the micro-rills grids and their orders (Strahler, 1957) were calculated for each DEM **(Table 4.4)**. The micro-rills density obtained from the PM was 2.03 mm cm^{-2} where it was 2.43 mm cm^{-2} for the micro-rills obtained from the PHM using the same grid size of the PM (10 mm). The difference in the micro-rills density was less than 20%, which demonstrates good agreement between the two networks. These differences between the two micro-rills can be attributed to the DEM sampling size, which can be shown clearly by observing the micro-rills orders. The PM micro-rills demonstration was four stream orders where the PHM was 6 stream orders. The correlation coefficient of the micro-rills densities for the first four orders was 0.99 (P=0.002). The total number of micro-rills grids located in order 5 and 6 for PHM was only 16 grids, which emphasize that the discrepancy was mainly due to the sampling grid size. The importance of the drainage network density is that it reflects the potential for scoring (changing the soil microtopography) by surface runoff (Römkens et al., 2001). Thus, the drainage network represents an important method to identify the potential of using consumer-grade cameras to quantify the soil microtopography at plot-scale level.

There are a few studies which have dealt with the micro-rills optimum grid size, which greatly affects the micro-rills density and the number of orders **(Table 4.4)**. The micro-rills density was 2.43, 2.77, and 3.39 mm cm^{-2} for 10, 5, and 2 mm grid sizes; respectively. The micro-rills density was increased 14% and 40% under 5 and 2 mm grid sizes, respectively. This result emphasizes that the grid size has a great effect on the micro-rills delineation, and subsequently the soil microtopography quantification. However, from the view point of visual interpretation for the delineated micro-rills network under different grid sizes **(Fig. 4.8)**, the network clearly appeared on the large grid size compared with the small grid size and manually delineated micro-rills shown in **Fig. (4.1)**. On the other hand, the small grids showed high effect on the micro-rills density and low potential in the visualization of the micro-rills compared with the large grid size.

Table 4.4. Micro-rills grid numbers and stream order obtained from the pin-microrelief DEM and the photogrammetry DEM with 10, 5, and 2 mm grid size.

Measurement method	Grid size (mm)	Rill grids (grid)	Rill grids for each stream order (grids)							
			1	2	3	4	5	6	7	8
Pin-microrelief	**10**	137	100	18	10	9	–	–	–	–
Photogrammetry	**10**	164	109	20	14	5	14	2	–	–
Photogrammetry	**5**	375	233	52	27	21	7	23	12	–
Photogrammetry	**2**	1145	722	137	104	48	20	48	23	43

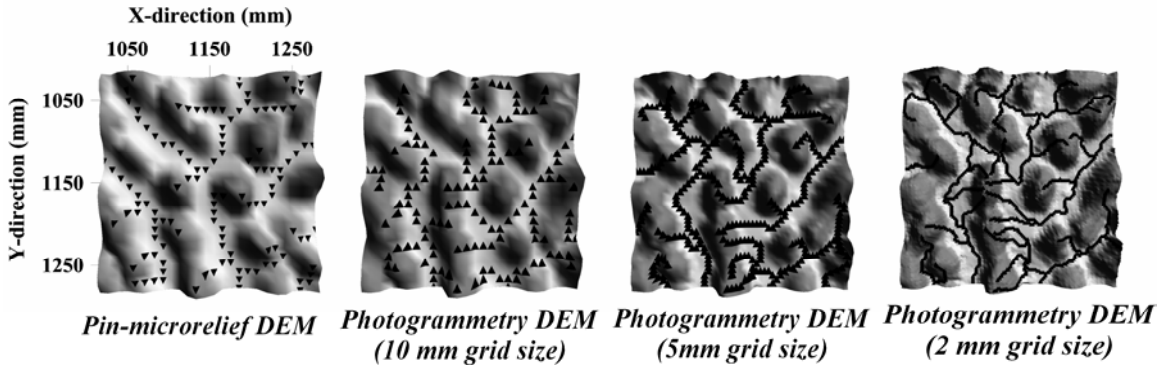

Fig. 4.8. Micro-rills delineation and the shaded-relief map for the DEM obtained from the pin-microrelief meter and photogrammetry with different grid size.

4.4. Conclusions

Soil microtopography is a dynamic soil property, which needs rapid method in order to achieve the temporal variation with acceptable precision. The laser scanner has been used for soil surface quantification for long time, and provides DEM with high accuracy and precision. However, since that time no commercial low-price laser scanner has been developed. Moreover, the laser scanner consumes a great deal of time to acquire the field data.

The recent developments in digital photogrammetry enabled it for the non-specialist. Digital photogrammetry is a rapid method for data acquisition, and takes only a few minutes to acquire data from the field; however, it needs extra time for image analysis. Also, the new developments in automated digital photogrammetry systems have made DEM generation easer and faster with automated homologous points identification.

This study explored the potential of using consumer-grade cameras in order to quantify soil surface effectively. The generated DEMs accuracy was validated visually and numerically. The visual interpretation for the DEMs showed high similarity

between the surfaces generated from the photogrammetry, and the surfaces generated from the pin-microrelief meter and the 2D images. Numerically, the RMSE was used to define the accuracy of the photogrammetry system. The RMSE for the rough surfaces and the rilled surface was less than one mm in the z-direction (elevation accuracy). However, the RMSE on the x- and y- direction (spatial accuracy) was greater than one and less than 2.5 mm, and requires more investigation to define the source of these errors. The soil roughness indices calculated from the DEM generated by the photogrammetry were well correlated to the DEM generated from the pin-microrelief data, and all the differences can be attributed to the high sampling density of the photogrammetry. The two methods' depression grids were mapped and compared, and matched each other sufficiently. However, the depression storage capacity showed high scale dependency. The micro-rills from the two methods were delineated and compared, and showed acceptable agreement. The grid size did not present a great effect on the calculated roughness indices compare with its effect on the DA%, DSC, and the delineated micro-rills. Although the small grid sizes gave results with fine details, the large grid size presented the gypsum micro-rills network much more clearly than the small grid size. The close-range photogrammetry system using a consumer-grade camera showed high potential in quantifying the gypsum surfaces, which were used to simulate soil microtopography with different roughness conditions, compared with direct measurement using pin-microrelief meter.

CHAPTER 5:

Development and application of digital elevation model rectification method in monitoring soil microtopography changes during rainfall

5.1. Introduction

The soil surface variables have a significant impact on sediment generation, sediment transportation, and water flow. Soil microtopography or roughness controls overland flow through surface depressions (Hansen *et al*., 1999; Kamphorst et al., 2000; Darboux and Huang, 2005), modifying flow velocities (Gover, 1992; Gimenez and Gover, 2001), water infiltration and overland flow organization (Gover et al., 2000). Soil microtopography at micro-scale seems to control most of the soil surface-water interaction processes, and has received increasing attention from researchers with regard to the measurement techniques used, their accuracy and interpretation.

The measurement techniques used for soil microtopography were developed early in 1960s employing microrelief meters (Kuipers, 1957; Burwell et al., 1963; Allmaras et al., 1966). Another cheap and simple method is "The chain method", which was developed by Saleh (1993).

To monitor soil microtopography quantitatively, a more precise means of generating the digital elevation model (DEM) is necessary. Currently, the non-contact techniques, laser scanning (Huang et al., 1988; Helming et al., 1998) and photogrammetry (Jeschke, 1990), are preferred by researchers because of time and laborer saving and for the ability of these methods to obtain the DEM of the soil surface. Digital photogrammetry is a modified version of the analog and analytical photogrammetry, which provides and enables even for a non-photogammetrist to use this efficient, rapid and inexpensive tool (Chandler, 1999; Lascelles et al., 2002; Rieke-Zapp and Nearing, 2005).

The major emphasis in the studies on the effect of soil microtopography on soil hydrological responses has focused primarily on the initial soil roughness (Magunda et al., 1997; Römkens et al., 2001). However, the temporal changes in soil surface roughness associated with rain impact and the hydrological properties of the soil during rain events are equally important for their effect on water, sediment, and nutrient flow. Few studies have been reported on the effect of the dynamic changes of the soil microtopography during rainfall and their effect on different hydrological processes

partly because of the lack of a reliable method with which to monitor these changes on the soil surface.

An automated digital photogrammetry can be used to assess and detect the soil surface changes during rainfall events (Rieke-Zapp and Nearing, 2005). Although, there are several unresolved issues with regard to the accuracy and reliability of the digital photogrammetry some authors still consider it a reliable option (Stojic et al., 1998). Yamamoto et al. (2001) reported serious errors appeared in the generated DEM using digital photogrammetry under rainfall and surface flow condition. This requires further investigation in order to generate accurate and reliable soil surface DEM during rainfall.

The soil roughness indices such as the Random roughness "RR"; the Limiting elevation difference "LD", and the Limiting Slope "LS" were used intensively as indicators of changes occurring in the soil microtopography by tillage and rainfall (Taconet and Ciarletti, 2007; Vidal Vâquez et al., 2006; Magunda et al., 1997; Wesemael et al., 1996; Linden and Van Doren, 1986). However, the change in soil microtopography during rainfall has not been well investigated.

The objectives of this study were to: (1) to develop methods to rectify the digital elevation model (DEM) generated by the automated digital photogrammetry system, and (2) apply these methods in monitoring the changes in soil microtopography during rainfall. Rainfall simulator experiments were carried out and soil microtopographic changes were evaluated, from which a 3D vision of soil surface was generated.

5.2. Experimental setup

5.2.1. Soil plot preparation

The experiments were conducted using clay soil collected from the Tohaku area, Tottori prefecture in Japan. The soil was air dried in a glasshouse for two weeks and then crushed and sieved through 2 mm grid size screen **(Table 5.1)**. The soil was packed in 1.0 × 0.5 × 0.16 m steel plots (**Fig. 5.1**, **Fig. 5.2**) over a 0.04 m depth gravel layer which acted as filter. The soil was packed to 0.09 m depth above the gravel filter with 1.01 g cm^{-3} bulk density. The soil was wetted for 24 hours from the bottom of the plot using venial pipes connected to another plot filled by water. The pipes were removed and the plots were left for 12 hours to drain the excess water before the rainfall simulation study.

Table 5.1. Physical and chemical properties of the experimental soil (Tohaku soil).

Parameter	Values
Bulk density (Mg m^{-3})	1010
Clay (g kg^{-1})	440
Saturated hydraulic conductivity (cm sec^{-1})	1.9×10^{-5}
Saturation water content (g kg^{-1})	483.8
Organic Matter (g kg^{-1})	2.88
pH	5.8
Ec (dS m^{-1})	0.06

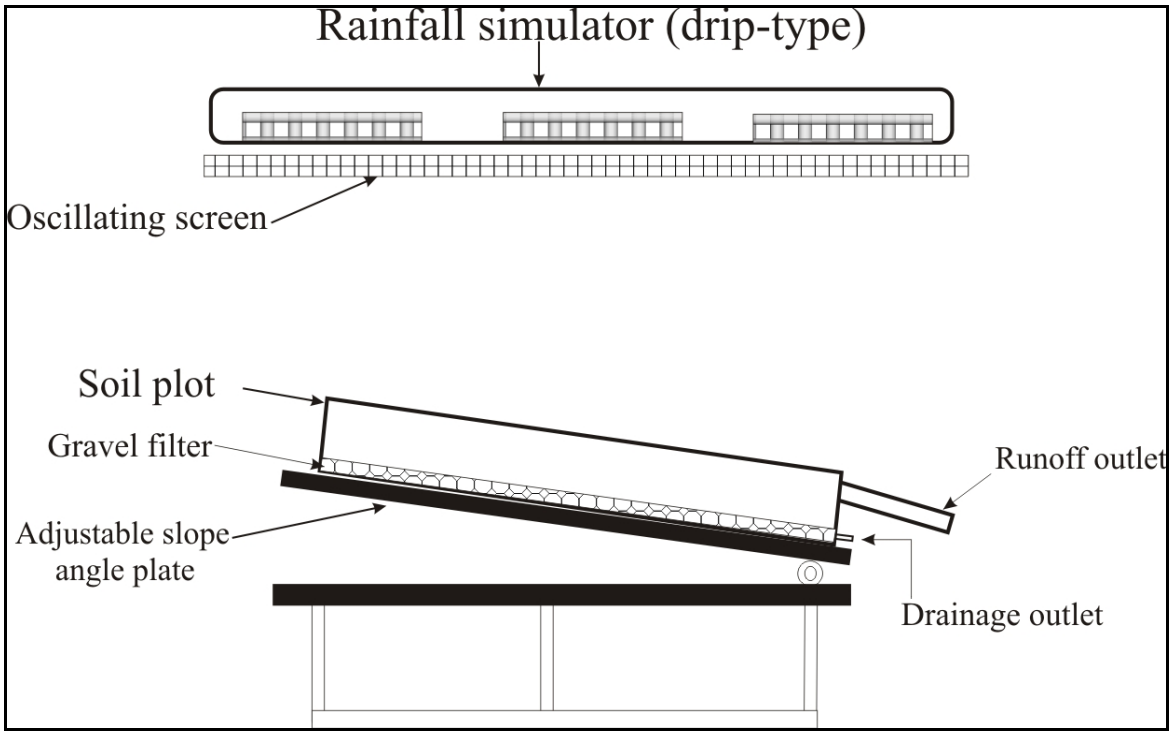

Fig. 5.1. Schematic view of the rainfall simulator.

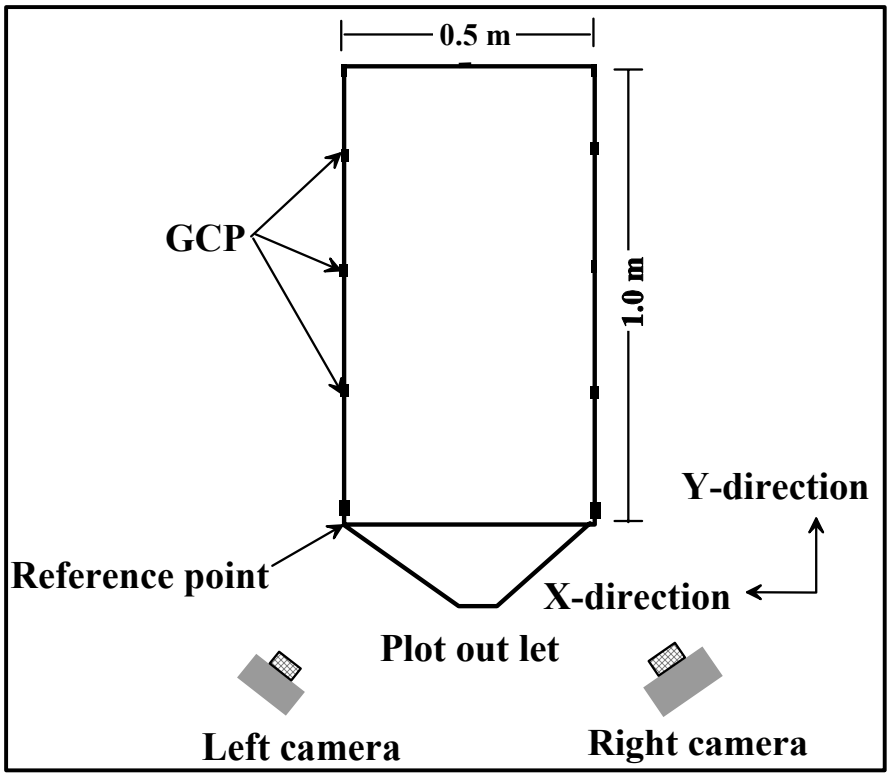

Fig. 5.2. Schematic view of soil plot components, two fixed-cameras photography system, ground control points (GCP) and the reference point.

The rainfall intensity was 35mm.hr^{-1} and the rainfall duration was 60 minutes. The soil plot was located on the steel plate and the slope angle was adjusted to 10 degrees, simulating the interrill hillslope condition. The soil plot edges were marked with red adhesive tape with clear black cross on eleven locations in order to use these marks as a ground control points (GCP). The GCPs were measured to near millimeter accuracy, using a steel ruler, for x-, y- and z-directions from a reference point (Abd Elbasit, 2006), which was the bottom left corner of the soil plot **(Fig. 5.2)**.

5.2.2. Rainfall simulator

A laboratory drip-type, 12 m height rainfall simulator and 3D erosion analysis system available in Arid Land Research Center, Japan was used in all experiments **(Fig. 5.1)** (Yamamoto *et al*., 2002; Moritani et al., 2006). The rainfall simulator was intensively calibrated with respect to the flow rate and rainfall intensity relationship and the rainfall depth spatial distribution. The height was sufficient for the rainfall droplet to

reach its terminal velocity, making the rainfall impact energy similar to the natural rainfall (Abd Elbasit, 2006).

The mean drop size and terminal velocity of the rainfall simulator were approximately 5.4 mm (spherical equivalent) and 9.4 ms^{-1}, respectively (Ravolonantenaia, 2004). The rainfall simulator was equipped with oscillating screen in order to distribute the rainwater uniformly and to avoid dripping at certain points. The experimental area was about 2.3 m^2, occupied by adjustable angle steel plate and protected from any air current.

5.2.3. Camera system

Two calibrated Kodak DCS 460c digital cameras were used for image acquisition **(Table 5.2)**. The cameras were composed of three parts: (i) Kodak camera back including charge coupled device (CCD) sealed, one-piece unit; (ii) Nikon N90 camera body that had its film back removed; and (iii) 50 mm focal length Nikon lenses with ultra-violet (UV) filters attached to the camera body. The UV filters served two purposes; firstly acting as absorber of the light haze generated from light reflectance by simulated rainfall drops and secondly as mechanical protector for the lenses. The two cameras were equipped with PCMCIA (Personal Computer Memory Card International Association).

The finders of the two cameras were equipped with a CCD camera and connected to two color monitors in order to control the direction of the two cameras remotely. The manual mode was used in this experiment, and the f/value (aperture value) was adjusted and fixed to 2.8.

Two motorized platforms were used to hold the left and right cameras. Each platform was equipped with two electrical motors, the first to control the lateral movement (around the x-axis) of the camera and the second motor to control the vertical movement (around the z-axis) of each camera. The speed and direction of the four motors was controlled by PC software (3D water erosion system). Both platforms were mounted on a wheeled aluminum frame, to facilitate the control of the location of the frame anywhere around the rainfall simulator. The two monitors and the PC with software were used together to orient the cameras.

Table 5.2. Specification of Kodak DSC460c camera and the calibration information for left and right camera with Nikon lens 50mm (f/2.8).

Parameter	Left Camera	Right camera
CFL[a] (mm)	49.9858	50.0838
CCD[b] (pixel)	3060×2036	3060×2036
CCDx[c] (mm)	0.009	0.009
CCDy[d] (mm)	0.009	0.009
CCPPx[e] (mm)	- 0.0022	- 0.0029
CCPPy[f] (mm)	0.0007	0.0061
K1[g] (mm)	5.0320363×10^{-6}	3.9182763×10^{-5}
K2[h] (mm)	7.7630741×10^{-11}	-1.2439131×10^{-7}

[a)]Calibrated Focus Length; [b) and c)] Charge-Coupled Device pixel dimension for the x and y direction, respectively; [e)]Corrected Coordinate of Principal Points for the x and y direction, respectively; [g) and h)] Coefficients for Radial Lens distortion (RLD)

5.3. Methodology

5.3.1 Images acquisition

Detecting changes in soil micro-topography through the use of multi-temporal photogrammetric survey requires careful consideration and definition of the cameras location (Stojic *et al*., 1998). In this study, fixed datum was used for all imaging time steps, which ensured that all the differences in soil elevation were due to impact of rainfall drops and sediment generation, transportation and deposition. The oblique-photography system has the advantages of reducing the flying height (camera height above the object) required to capture the image of an object (Lascelles *et al*., 2002) and of locating the camera station outside the rainfall simulation area, which enable the photos to be taken without removing the camera stations every time. However, the oblique photography system has some problem during data processing and DEM generation (Chandler, 1999).

The coordinate systems were measured from a reference point for each camera station **(Table 5.3)**. The rotation angles, which describe the camera angle, around the z-axis, x-axis and y-axis, κ, ω and φ respectively, were measured using photography and protractor methods to the near minute.

The two cameras operated simultaneously. The pair was controlled by the PC using the software for image capturing, time interval programming and image transferring from the cameras to the PC through SCASII connections. Time interval of the imaging was 10 minutes starting from 0 minute (the commencement of rainfall simulation) to 60

minutes. Seven pairs of images were transferred to the computer hard disc as left and right images.

Table 5.3. Left and right Kodak DCS460c cameras location and rotation angles.

Camera	Left Kodak DSC460c	Right Kodak DSC460c
Coordinate/Angle		
x-direction (mm)	740.0	1360.0
y-direction (mm)	- 1951.0	- 1951.0
z-direction (mm)	1865.0	1865.0
$\omega^{a)}$ (°)	0.0	0.0
$\varphi^{b)}$ (°)	11.42	-11.42
$\kappa^{c)}$ (°)	23.87	23.87

a), b) and c) Camera rotation angles around x, y and z axis, respectively.

5.3.2. DEM generation

There are two steps of the photogrammetric processing for each stereo-pair of the image: 1. Photogrammetric triangulation 2. Automated DEM processing **(Fig. 5.3)**. The photogrammetric triangulation used a least-squares block bundle adjustment to estimate the exterior orientation parameters (camera location and angles) (the interior parameters are already provided by the calibration of cameras). The resulting exterior and interior orientation (camera location and camera internal properties) parameters were used for automated DEM extraction (Stojic et al., 1998). A software (non-commercial: Asia Air Survey Co.) was used to generate DEM of the soil surface (distributed x, y and z data). The digital photogrammetry software is a part of the 3D erosion analysis system (Yamamoto et al., 2002; Moritani et al., 2006). This system consists of two parts; 1) digital photogrammetry, which is responsible for the DEM generation from a stereo-pair images (left and right images and was used in this study to generate the DEM during rainfall), 2) DEM analysis to estimate the soil erosion using multi-temporal DEMs differences. The digital photogrammetry part is adopting standard methods to generate the DEM. However, the capability of the software to generate accurate DEM depends on many interactive factors including the cameras specification and user proficiency.

The accuracy of the DEM generated from the software was assessed using 10 checkpoints on the edge of the soil plot. The root mean square error (RMSE) was used to evaluate the differences between the measured and the estimated values at each checkpoint (using digital photogrammetry). The horizontal (x and y-directions) and the elevation (z-direction) accuracy were assessed.

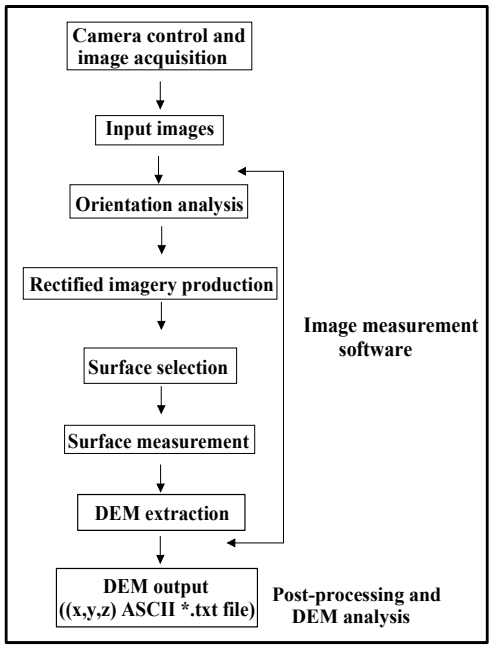

Fig. 5.3. Flowchart of image processing and DEM extraction steps in the Asia Air Survey Co. software.

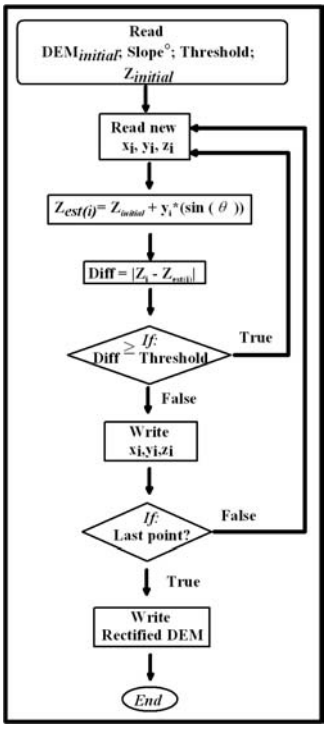

Fig. 5.4. Flowchart illustrating the reference surface method (RSM) used to rectify the DEM prior to the interpolation.

The approach for fitting a three dimensional coordinate system to fixed base stereo-pairs is somewhat different from ordinary vertical system (aerial photogrammetry). Although the interior and exterior orientations are similar to those used for conventional aerial photography, the absolute orientation is modified. The left photograph assumed to be the base-scalar and the distance between the stereo-camera is used to scale the stereo-model (Warner and Reutebuch, 1999).

The first step of image processing was the image matching to adjust the GCPs to the corresponding points of the pair of images.

5.3.3. DEM error detection and rectification

The DEM error rectification is essential step prior to any DEM manipulation processes (e.g., Butler et al., 1998). The 3D data sets were rectified by two methods (the reference surface method and the parametric statistical method):

5.3.3.1. Reference surface method (RSM)

Prior to the DEM interpolation, a certain threshold of the difference between the original DEM and simulated smooth surface (the reference surface) was decided. In this study 20 mm was defined as the threshold value. The general slope (plot slope (θ)) was used to generate the reference surface (Eq. 1). Hereinafter this method is called the reference surface method (RSM).The method assumes that there is no general systematic effect of the slope in x direction on the soil microtopography **(Fig. 5.4)**. Therefore, the DEM errors were detected and eliminated using the following procedures:

i) The raw DEM points were read one-by-one (x, y, z); the slope angle; the initial point elevation (zero point which was defined as the bottom left corner of the plot) and the threshold (maximum level of error in mm).

ii) Generation of estimated elevation for point "*i*", using the following equation:

$$z_{est(i)} = z_{\text{int}} + y \cdot \sin\theta \qquad (5.1)$$

where $z_{est(i)}$ is estimated elevation (mm), z_{int} is the initial point (mm) (zero point), y is the y-direction value (mm) and θ is plot slope (10 degrees);

iii) Calculate the difference between the estimated elevation and the actual elevation for the point i;

iv) If the difference between the two elevations is greater than the threshold then this point is considered an error point and deleted from the output DEM file. If the difference is less than the threshold then it is considered as correct point and registered in the output DEM file **(Fig. 5.4)**.

The output of these procedures will result in scattered elevation points for the soil surface. The scattered elevation points were then interpolated using the inverse distance weighted (IDW) method. The inverse distance weighted (IDW) method was used to interpolate the 3D data in 2 mm grid size form. This method is based on the assumption that the value at an unsampled point can be approximated by a distance weighted average of sampled points occurring within a neighborhood (Woolared and Cloby, 2002; Burrough and McDonnell, 1998).

5.3.3.2. Parametric statistical method (PSM)

The interpolated data were manipulated for error rectification using the parametric statistical method (Flicísimo, 1994). This method is based on the t-test comparison between two elevation values on each point, the first one is (original point) collected by the DEM, the second (estimated point) obtained as an average of the 4 neighboring points (Flicísimo, 1994). If the difference between the two points (original and estimated) is significant the estimated point will be used instead of the original point. The method was originally developed for large scale DEM rectification using geographical information system (GIS). In this study, a FORTRAN program was composed to manipulate the error of the DEMs in the micro-scale using the PSM.

5.3.4. Roughness indices

The rectified DEMs by the two methods (RSM and PSM) were used to calculate indices for surface roughness at different time steps during the rainfall event. There are numerous roughness indices in literature. However, Huang and Bradford (1990) argued that the roughness cannot be completely described by a single index. Govers et al. (2000) reported that the single index is never capable of quantifying the variance (reflecting the absolute variation in height) and the correlation length (describing the distance over which spatial autocorrelation occurs). The same authors also indicated that

most existing roughness indices indeed describe either the variance (RR and LD) or the correlation length: Fractal Dimension, (FD); Tortuosity, (T) and LS.

Many researchers observed the decrease in RR as a function of accumulated rainfall depth (Magunda et al., 1997; Linden and Van Doren, 1986; Onstad et al., 1984). However, increase in roughness could occur under smooth soil conditions. Smooth surface contributes to generation of microrills and depressions resulting from raindrop impact.

In this study three roughness indices were calculated from temporal data of DEMs for the experiment. These indices gave the temporal soil surface changes with time. Random Roughness, RR, (Allmaras *et al*., 1966) was calculated as standard deviation of the elevation values as in equation (2).

$$RR = \left[\frac{1}{k} \sum_{i=1}^{k} (Z_i - \bar{Z})^2 \right]^{1/2} \qquad (5.2)$$

Where Z_i and $\bar{Z}$ are height reading at i location and the average, respectively. k is the number of elevation readings.

The limiting slope (LS) and limiting elevation difference (LD) developed by Linden and Van Doren, (1986) are spatial aspect roughness indices. These are based on the slope or inclination of the surface of soil clods and the average relief (elevation difference), respectively. LS and LD are based on the first –order variance or mean absolute elevation difference (ΔZ_h) as a function of lag (h) (the distance difference between each pair of point in the x-direction) as reported by Kamphorst et al. (2000). The linear regression analysis was used to obtain the relationship between ($1/\Delta Z_h$) and the reciprocal form of the lag distance ΔX_h as in equation (5.3) below.

$$\frac{1}{\Delta Z_h} = b \frac{1}{\Delta X_h} + a \qquad (5.3)$$

$$LD = \frac{1}{a} \qquad (5.4)$$

$$LS = \frac{1}{b} \qquad (5.5)$$

The parameters *a* and *b* are respectively, the intercept and slope of equation (3), and their reciprocals are LD and LS, in equation (5.4) and (5.5) as reported by Linden and Van Doren, (1986) and Hansen et al. (1999).

5.4. Results and Discussion

5.4.1. DEM accuracy

The accuracy of the DEMs was assessed by difference between directly measured and photogrammetrically estimated values at checkpoints located on the edges of the soil plot **(Fig. 5.5)**. The RMSE is a useful measure to assess the reliability and also for quantifying the accuracy of a DEM (Chandler, 1999). The RMSE was calculated from the differences between the measured and estimated coordinate dimensions and elevation of the checkpoints at different time steps during the rainfall event **(Table 5.4)**. The accuracy of the DEMs generated during the rainfall event in this study was similar to the previous studies for surface microtopography of small scale, which was generated for the soil surface before and after rainfall (Taconet and Ciarletti, 2007; Rieke-Zapp and Nearing, 2005; Stojic et al., 1998, Butler et al., 1998). The present DEMs were generated during the rainfall event, suggesting the possibilities of obtaining the same result reported by previous authors. This emphasizes the reliability of the photogrammetric method to monitor the soil surface during rainfall event.

Table 5.4. Root mean square error of the digital elevation models checkpoints.

Axis/Time (minute)	0	10	20	30	40	50	60
x-direction (mm)	1.61	3.04	1.96	1.87	1.67	1.53	2.35
y-direction (mm)	2.38	3.20	2.59	2.10	2.40	2.12	2.98
z-direction (mm)	1.67	2.91	1.92	1.56	1.75	1.53	1.94

The average RMSE of checkpoints at different time steps for the x-, y- and z-direction were 2.08, 2.59 and 1.96 mm, respectively. There is no common standard to evaluate the quality of the DEM at the laboratory scale. The optimum accuracy basically depends on the desired accuracy in which the DEM will be applied. The accuracy of the DEM for roughness changes mainly depends on the size of surface individual components size. Rieke-Zapp and Nearing (2005) stated that precision of 1.26 mm on the vertical direction satisfied the measurement requirement of soil erosion in the plot scale. Accuracy of the surface roughness measurement using close range

photogrammetry reached to ±10 mm for gravel plot (300 x 300 mm) surfaces (Butler et al., 1998). In this study, the soil was sieved using 2mm mesh and the photogrammetrical system was able to detect the changes in microtopography to the range of 2 mm due to movement, destruction and accumulation of those aggregates. The overall accuracy on the vertical direction was ranging from 1.56 to 2.91 mm, which satisfies the needs of surface microtopography monitoring during rainfall event. The average RMSE for z-direction under rainfall condition was 1.93 mm, which is quite similar to the RMSE under no-rainfall condition (1.80 mm). The difference between the DEM accuracy under simulated rainfall and dry condition (the initial and final time steps) was less than 0.2 mm for the x-, y- and z-directions.

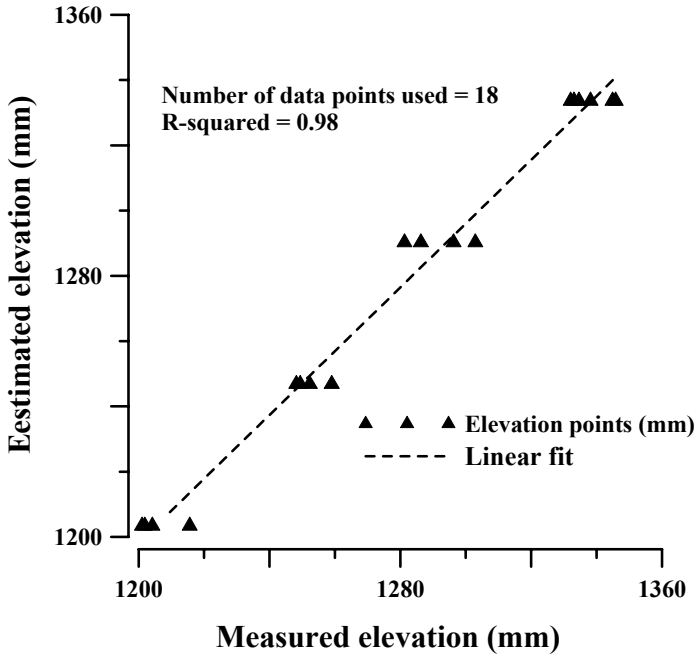

Fig. 5.5. Assessments of elevation accuracy using measured and photogrammetrically estimated checkpoints.

5.4.2. DEM error detection and rectification

The rectification of DEM is an essential step prior to any DEM manipulation processes (Butler et al., 1998). In this study, two rectification methods were used to detect and rectify the DEMs error. The first is using the RSM and the second is the PSM. The main difference between the two rectification methods was the input data format. The RSM has the advantage of eliminating errors prior to interpolation; and it is very sensitive to threshold value. Threshold value decreases the variation in the surface

topography. It will be removed until the surface is completely smooth. The effect of the two rectification methods is shown in **Fig. 5.6.** The overlapping contour lines (black area, **Fig. 5.6**) are suggesting inconsistency due to extreme values in the DEM. The RSM rectification method removed these extreme values. The extreme values can be recognized at the top left corner (around x=1200, y=1700 mm).

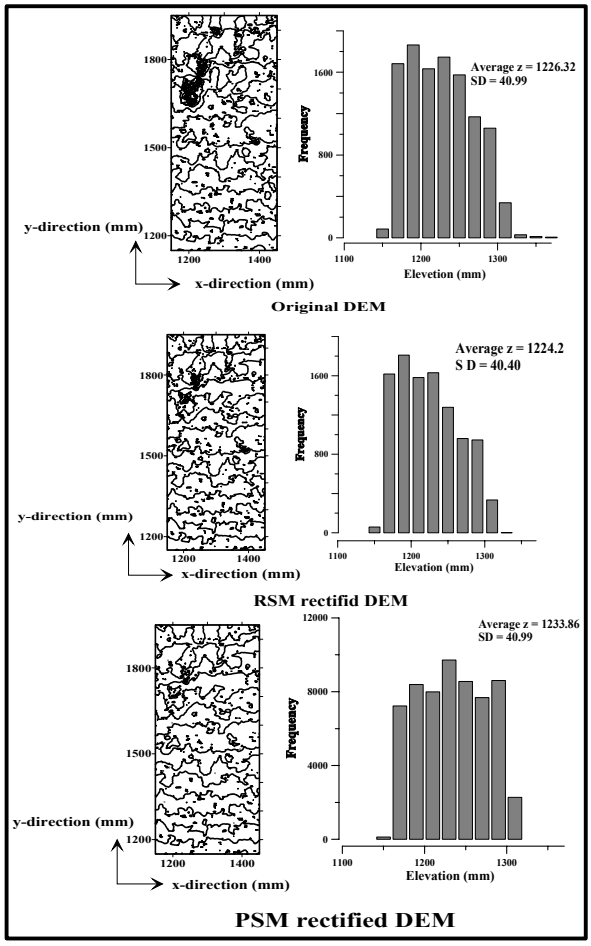

Fig. 5.6. Effect of the RSM and PSM on the DEM , contour lines consistency, and elevation frequencies (SD: Standard Deviation).

The procedure of excluding the 10% lower and upper extreme values is used to eliminate the errors in a DEM before the calculations of roughness indices (Hansen et al., 1999). However, this method could remove most of the micro-variations in the DEM. The present study removed the extreme values only from the DEM without affecting the micro variations in the DEM. The two methods employed resulted in no significant differences in the standard deviations (SD was 40.40 and 40.99 mm for RSM and PSM, respectively).

The statistical parameters of the rectified surfaces were calculated **(Table 5.5)**. Although there was no difference in the statistical parameters between time steps, the standard deviation showed a trend of decrease with time steps. The initial soil surface can be recognized as a peak point for all calculated statistical parameters.

Table 5.5. Statistical parameters of the soil surface elevations at different time steps.

Time Step (minute) / Parameters	0/Initial	10	20	30	40	50	60/Final
Range (mm)	38.58	22.15	26.31	34.63	22.92	23.08	23.42
Mean (mm)	78.37	79.03	80.73	83.04	78.39	77.93	78.11
SD[a] (mm)	4.05	3.69	3.79	2.52	3.84	3.56	3.93
Median (mm)	77.89	79.09	80.75	82.56	78.03	77.53	77.71
25%-tile (mm)	75.38	76.30	78.06	81.83	75.22	75.22	74.71
75%-tile (mm)	75.60	81.69	83.36	83.47	80.90	80.19	80.83

[a]Standard Deviation

5.4.3. Soil surface evolution

The shaded relief surfaces of the DEM at different time steps were generated during the rainfall **(Fig. 5.7)**. The surface was smoothed by rainfall with time and the depressions were also developed with time (dark areas in **Fig. 5.7**).

The roughness of the soil surface, generally, increases with tillage and decreases with cumulated rainfall depth. The decrease due to the rainfall can be attributed to the breakdown of the aggregates and surface sealing due to the rainfall impact energy, which represents the most important factor affecting the soil microtopographical changes (Wesemael et al., 1996).

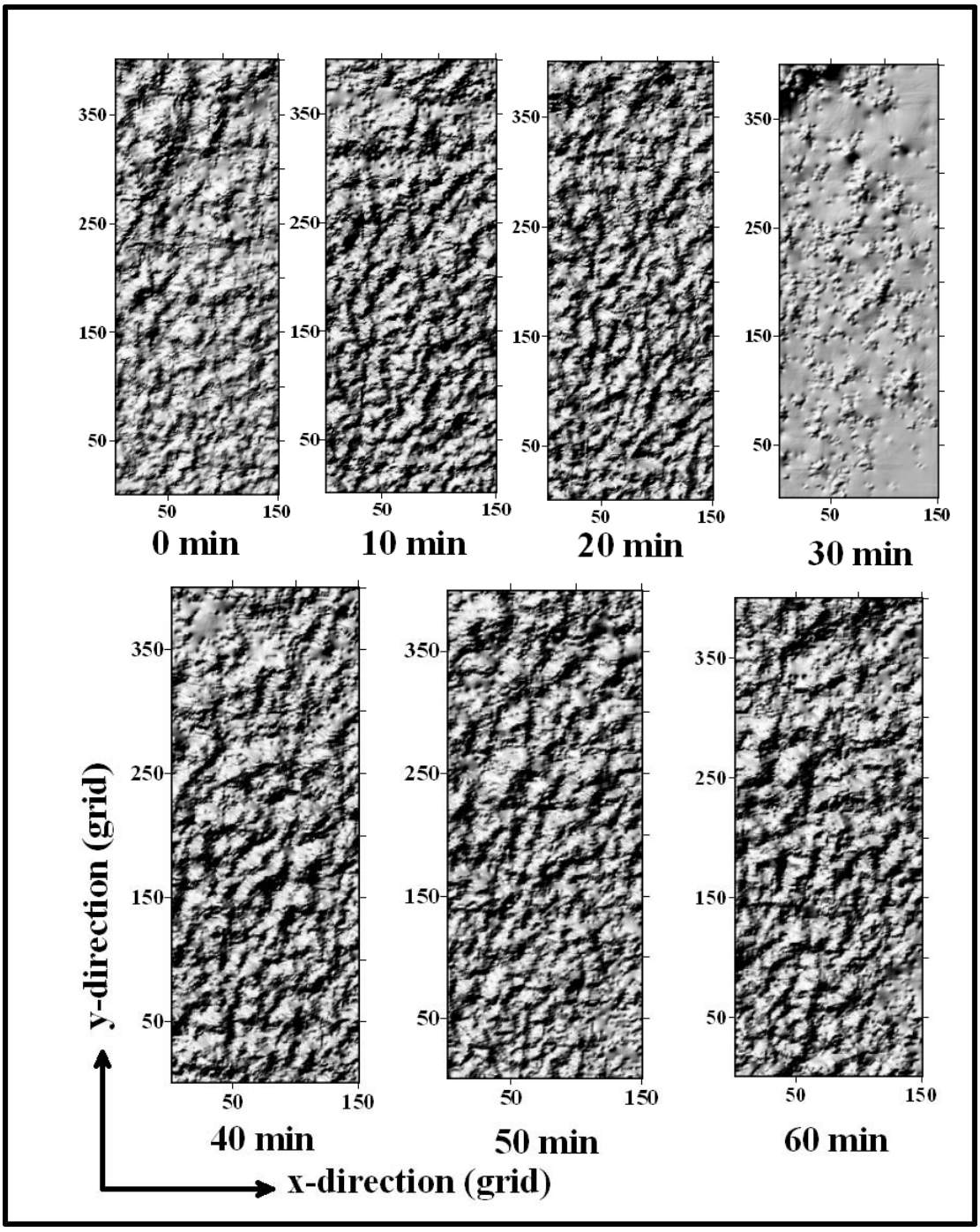

Fig. 5.7. Shaded relief maps of soil surface at time steps 0, 10, 20, 30, 40, 50 and 60 minutes (the grid size is 2 mm). The DEM extraction error can be noticed at time step 30 minutes.

5.4.4. Roughness indices

The soil roughness evolution was assessed using three roughness indices, RR, LD and LS **(Table 5.6)**. The RR was calculated directly from the rectified elevation data.

The RR, LD and LS indices showed a trend to decrease with time. In other words, the soil roughness indices decreased as the simulated rainfall depth increased **(Fig. 5.8)**. However, slight increases in RR and LD at the final time steps were observed and this could be attributed mainly to the development of pitch and micro-rills. On the other hand, the LS index decreased 42% at the beginning of the rainfall event and remained without much change with the advanced time steps. The present result did not agree with the function recommended by Onstad et al. (1984), regarding the relation between the RR and cumulative rainfall. This could be attributed to: the soil plot size, differences in the rainfall duration and rainfall depth together with the initial moisture content of the soil surface. The smoothing of the initially moist surface is very slow, which is in agreement with result of Wesemael et al., (1996).

Table 5.6. Roughness indices calculated form the corrected DEM at different time steps.

Roughness Indices (mm)	**RR[a)]**	**LD[b)]**	**LS[c)]**
Time steps (minute)			
0/Initial	4.05	18.87	0.85
10	3.69	12.77	0.49
20	3.79	16.18	0.52
30[d)]	2.52	58.93	0.11
40	3.84	16.17	0.49
50	3.56	15.17	0.35
60/Final	3.93	20.08	0.35

[a)]Random roughness; [b)]Limiting Elevation Difference; [c)]Limiting Slope;

[d)] The DEM extraction at step 30 minute was poor

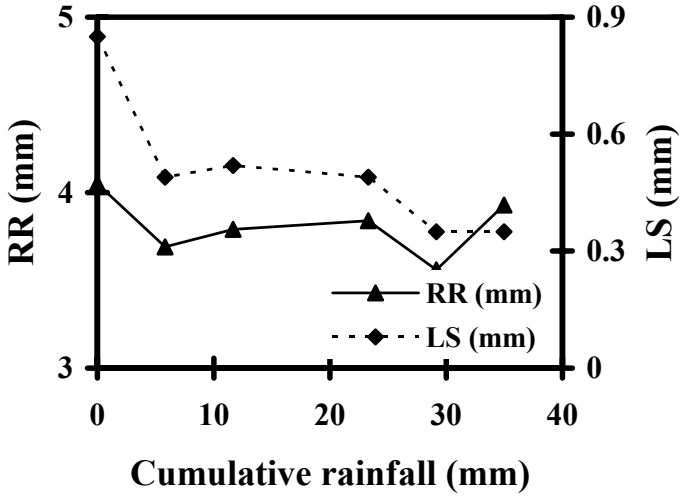

Fig. 5.8. Relationship between cumulative rainfall depth and random roughness (RR) and limiting slope (LS) roughness indices (DEM at 30 min was neglected).

5.5. Conclusions

In this study, the soil microtopography changes were monitored during the rainfall event using photogrammetrical method. Completely automated fixed cameras-base photogrammetry system was used in order to acquire the temporal microtopography images. The average root mean square error (RMSE) of the DEMs was 1.96 mm in the z-direction, which satisfied the research objective of monitoring the soil microtopographic change during rainfall event. The soil microtopography was smoothed as described by the roughness indices, (decreased with rainfall duration)

This study presented advanced tools for the generation of rectified DEM to monitor the soil microtopography changes under rainfall. Prior to interpolation, the DEM errors were eliminated using the reference surface method, which was developed as a part of this study. The parametric statistical method was used to rectify the DEM errors after interpolation using small FORTRAN program.

The proposed two methods in this study can help to generate rectified DEM provided that the raw DEM has acceptable accuracy. The methods can be used for further studies related to clod breakdown by rainfall or by the effect of tillage implements, rill initiation and sediment quantification.

CHAPTER 6:

Simulation of hillslope interrill sediment generation using two modeling approaches and simulated rainfall experimental data

6.1. Introduction

Soil degradation due to water erosion is a serious threat to the quality of soil, land, and water. Soil water erosion is estimated to account for about 55% of the total degraded lands worldwide (El-Swaify, 1994). Particularly, upland interrill soil erosion is the main source of sediments discharged to water bodies and streams. The notion of spatial demarcation of rill and interrill erosion started with the necessity to model the erosion process by mass balance equations (Meyer and Wischmeier, 1969). Soil erosion is a complex phenomenon, which involves detachment and transport of soil particles, storage and runoff of rainwater, and infiltration (Romkens et al., 2001). Raindrop impact provides the primary force needed to initiate detachment of soil particles from the soil mass (Jayawardena and Bhuyan, 1999).

The dominant process of soil erosion in an interrill area includes: (1) soil detachment by raindrop impact and/or surface flow, (2) transport by raindrop impact and/or surface flow, and (3) deposit of soil particles (Sharma, 1996: 125-152). However, according to Dimoyiannis *et al.* (2006) the dominant processes in the interrill area are: (1) detachment by rainfall impact, and (2) transport of sediment by surface flow. Since according to these researchers the interrill areas are the main source of sediments, the estimation of interrill sediment generation is a prerequisite for the evaluation of soil losses in the whole watershed. In this context, several soil erosion modeling approaches have been developed to estimate sediment yield in different scales. Soil erosion models fall into three main categories; (1) empirical or statistical models, which are based on the analysis of the observed soil erosion factors such as rainfall sediment and runoff, (2) conceptual models that represent the soil erosion processes as a series of internal storages and incorporating some transfer mechanisms of the runoff and sediments, and (3) physically-based models which are based on the solution of the fundamental physical equations describing the water and sediments transport. This categorization depends on the physical processes simulated by the model, the model algorithms describing these processes, and the input data required by the model (Merritt et al., 2003). However, all these types can be combined in a single

model simulating complex interactive processes. Recently developed physically-based erosion prediction models such as the Water Erosion Prediction Project (WEPP) by Nearing *et al*. (1989) still involve empirical equations for detachment and transport (Sharma, 1996: 125-152).

The interrill erosion rate is generally determined based on the following empirical equation:

$$D_i = K_i I^p S_f \qquad (6.1)$$

where D_i is the interrill erosion rate (mass per unit area per unit time), K_i is the interrill erodibility (mass time per unit area), I is the intensity of rainfall (volume per unit area per unit time), p is the regression coefficient, and S_f is slope factor (Liebenow et al, 1990). This equation adequately describes the effect of rain, soil, and slope gradient on the interrill erosion rate (Kinnell, 1993). The most commonly used empirical erosion equation is the multiplication-of-factors type model proposed by Neal (1938) as follows:

$$Soil\ Loss = (SoilFactor) * (RainFactor) * (SlopeFactor) \qquad (6.2)$$

The concept of Equation (6.2) formed the basis for the development of the Universal Soil Loss equation (USLE) (Wischmeier and Smith, 1978) and is currently used in the WEPP model (Nearing et al., 1989) to calculate interrill erosion (Huange, 1995). The same function had been used by the empirical and physically-based model to determine the interrill erosion rate.

On the other hand, physically-based models are based on the process-based equations, describing stream flow and sediment generation in a catchment area (Merritt et al., 2003). Standard equations used in such models are the equations of mass and momentum conservation.

Both modeling approaches, empirical and physically-based, are used in the interrill soil erosion estimation. Most of these models were developed mainly to estimate the soil erosion in agricultural field conditions (gentle slope). However, the performance of the two approaches for hillslope interrill soil erosion estimation was rarely compared. In the present study the objectives were: (1) to estimate the hillslope interrill soil erosion using empirical and physically-based modeling approaches; (2) to evaluate the ability of the two approaches in predicting the sediment yield.

6.2. Materials and Methods

6.2.1. Experiment

6.2.1.1. Rainfall simulator

A laboratory dripper-type rainfall simulator (12 m height) at the Arid Land Research Center, Tottori University, Japan was used **(Fig. 6.1)**. The rainfall simulator was calibrated at various rainfall intensities, regarding the flow rate, rainfall intensity relationship and the rainfall depth spatial distribution. The height was sufficient for the rainfall droplet to reach its terminal velocity, making the rainfall impact energy similar to that of natural rainfall.

The median drop size and terminal velocity of the rainfall simulator were approximately 5.4 mm (spherical equivalent) and 9.4 m s^{-1}, respectively. The rainfall simulator was equipped with an oscillating screen in order to distribute the rainwater uniformly. The experimental area (2.3 m^2) was equipped with an adjustable-angle steel plate and protected from air currents.

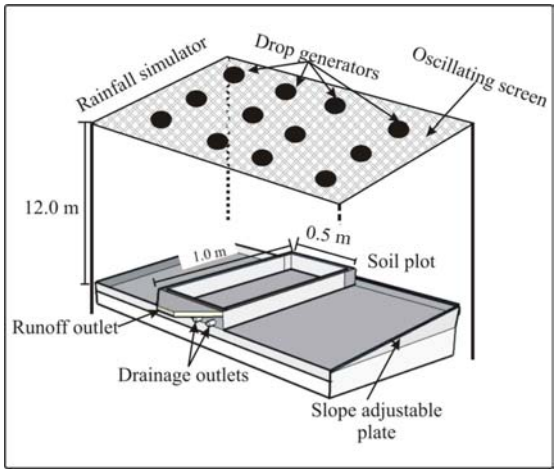

Fig. 6.1. Schematic view of the rainfall simulator.

6.2.1.2. Experimental setup

Two rainfall intensities (38 and 55 mm h^{-1}) were used under three slope angles (10, 15, and 20 degrees). Each combination was replicated three times. The rainfall depth was 38 mm. The slope angles were selected to simulate a wide range of natural hillslope conditions. The two rainfall intensities (38 and 55 mm h^{-1}) are greater than the 25 mm h^{-}

[1] defined by Hudson (1957) as the erosion threshold. The experiments were conducted using clay soil collected from the Tohaku area, Tottori Prefecture **(Table 6.1)**. The particle size distribution was determined using the pipette method (Gee and Bauder, 1986). The soil was air-dried in a glasshouse for two weeks and then crushed and sieved through a 2 mm grid size screen. The soil was packed in 1.0 × 0.5 × 0.16 m soil plots **(Fig. 6.1)** over a 0.04 m depth gravel filter. The soil was packed to 0.09 m depth above the gravel filter. The bulk density of the soil for all experiments was approximately 1.19 g cm^{-3}. The soil was wetted, from the bottom, to 70% saturation using a similar plot filled with water and connected with pipes to the experimental soil plot through drainage outlets for 24 hours. The pipes were removed and the plots were left for 12 hours to drain excess water before the rainfall simulation.

6.2.1.3. Data collection

The plot runoff (Q) was collected every five minutes using plastic bottles. The bottles were weighed before and after sample collection to determine the runoff volume. The bottles were then placed in an oven at 105ºC until all water evaporated. After the evaporation of the entire sample's water, the bottles were weighed to determine the sediment yield (D_i).

The soil plot drainage (DR) through the bottom outlets was collected using plastic bottles every five minutes and then measured using a measuring cylinder (accuracy ± 1 mL).

6.2.2. Analysis

6.2.2.1. Statistical analysis

Single factor analysis of variance and correlation analysis were carried out using statistical software for sediment yield (D_i) (kg m^{-2} h^{-1}), sediment concentration (Cs) (g L^{-1}), runoff (Q) (L m^{-1} h^{-1}), rainfall intensity (I) (mm h^{-1}), slope (S) (degree) and drainage (DR) (L h^{-1}).

Table 6.1. Physical and chemical properties of the experimental soil (Tohaku soil).

Parameter	Values
Bulk density (g cm^{-3})	1.19
Clay (g kg^{-1})*	440
Sand (g kg^{-1})*	240
Silt (g kg^{-1})*	320
Saturated hydraulic conductivity (mm h^{-1})	22
Saturation water content (g kg^{-1})	483.8
Organic Matter (g kg^{-1})	2.88
pH	5.8
EC (dS m^{-1})	0.06

*The particle size distribution was measured using the pipette method (Gee and Bauder, 1986: 383-411).

6.2.2.2. Empirical modeling approach

Empirical relationships between D_i, *Cs, Q, I, and S* were developed using non-linear regression analysis, and based on the Neal (1938) model structure. The Jayawardena and Rezaur (1998) model was used to validate the models developed in this study. Their model was developed under simulated rainfall intensities ranging from 30-245 mm h^{-1} and slope gradients ranged from 6-26 percent. The model was validated using field experimental data conducted by Wainwrite (1996). Empirical models developed by Jayawardena and Rezaur (1998), Huang (1995) and Kinnell (1993) were used for sediment yield estimation using the fitted soil-erodibility parameter and the current experimental data; models formula and parameters definitions are shown in **Table 6.2**.

6.2.2.3. Physically-based modeling approach

Kinematic runoff and erosion model (KINEROS2), an event physically-based runoff and erosion model (Smith et al., 1995), was used in order to estimate the interrill soil erosion. The model was used to estimate the interrill sediment generated during the rainfall simulator experiments.

The parameters were optimized for runoff and sediment yield simulation using an inverse method, where the model was executed several times with different parameters

and after each model-execution the outputs were compared with the observed data and accordingly the parameters were adjusted manually. One replicate from each experiment was used for the model calibration **(Table 6.3)**. The model was then executed using the parameters obtained in the calibration for runoff and sediment yield estimation. KINEROS2 adopts the kinematic wave method for the Hortonian overland flow simulation. The overland flow is simulated by combining the dynamic water balance equation and a simple power relation between discharge and unit area storage as follows:

$$\frac{\partial h}{\partial t} + \frac{\partial Q}{\partial x} = q(x,t) \qquad (6.3)$$

$$Q = \alpha h^{m} \qquad (6.4)$$

where h is water storage per unit area, Q is the discharge per unit width and it is a function of space and time (x,t), and $q(x,t)$ is net lateral inflow rate, which can be calculated by the subtraction of rainfall and infiltration.

Simulation of soil erosion involves solving the dynamic sediment mass balance equation (Bennett, 1974):

$$\frac{\partial (ACs)}{\partial t} + \frac{\partial (QCs)}{\partial x} - e(x,t) = q_s(x,t) \qquad (6.5)$$

where A is cross sectional area of flow, Cs is sediment concentration, $q_s(x,t)$ is rate of lateral sediment inflow for channels, and $e(x,t)$ rate of erosion of the soil bed.

KINEROS2 does not separate rill and interrill erosion processes explicitly; rather it divides the rate of erosion of the soil bed ($e(x,t)$) term into rain splash erosion (e_s) and hydraulic erosion (e_h). The net erosion is a sum of the splash erosion rate (e_s) and the hydraulic erosion rate (e_h) as follow:

$$e(x,t) = e_s + e_h \qquad (6.6)$$

The splash erosion rate (e_h) is approximated by the KINEROS2 model as a function of the square of the rainfall rate (Meyer and Wischmeier, 1969). The hydraulic erosion

rate (e_h) is estimated as being linearly dependent on the difference between the equilibrium concentration and the current sediment concentration as follows:

$$e_h = c_g (C_m - C_s) A \qquad (6.7)$$

where C_m is the concentration at the equilibrium transport capacity, $C_s = C_s(x,t)$ is the current local sediment concentration, and c_g is a transfer rate coefficient.

6.2.2.4 Model comparison

The results of the empirical models and KINEROS2 model were compared for sediment estimation using three indices:

6.2.2.4.1 Coefficient of determination (R^2) of the linear regression with zero intercept;

6.2.2.4.2 Root mean square errors (*RMSE*), which was calculated using the following equation as a percentage form:

$$RMSE\% = \sqrt{\frac{1}{n}\sum_{i-1}^{n}(E_i - O_i)^2}\ \frac{100}{\overline{O}} \qquad (6.8)$$

where E_i and O_i are the estimated and observed sediment yield, respectively, and $\overline{O}$ is the average of observed sediment yield;

2.2.4.3. Model efficiency (*ME*) developed by Nash and Sutcliffe (1970), which calculated as follow:

$$ME = 1 - \left[\frac{\sum_{i=1}^{n}(E_i - O_i)^2}{\sum_{i=1}^{n}(O_i - \overline{O})^2}\right] \qquad (6.8)$$

where E_i and O_i are the estimated and observed sediment yield, respectively and $\overline{O}$ is the average observed sediment yield.

Table 6.2. Empirical model forms used for soil loss estimation.

Type	Model	Factors	Fitted Parameters	Reference
Power	$D_i = K_i I^P S_f q$	Rainfall, slope and runoff	Soil erodibility and P	Sharma (1996)
Power	$D_i = K_i I S^{2/3} q^{5/3}$	Rainfall, Unit discharge and slope	Soil erodibility	Jayawardana and Rezaur (1998)
Polynomial	1. $q_s = A_1 q_w^2 + A_2 q_w + A_3$ 2. $q_s = B_1 S^2 + B_2 S + B_3$ 3. $q_s/q_w = D_1 q_w^2 S^2 + D^2 q_w S + D_3$	Runoff rate, Slope and sediment concentration	A_1, A_2, A_3, B1, B2, B_3, D_1, D_2 and D_3 soil dependent coefficient	Huange (1995)
Power	$q_{si} = K_1 q_w I f(S)$	Runoff rate, Slope and rainfall intensity	K_1 coefficient varied between soils.	Kinnell (1993)

D_i: sediment yield; I: rainfall intensity; q: unit discharge, S , S_f, and $f(S)$: slope factor; qs: sediment delivery; qw: runoff rate, qsi: sediment yield, K_i: soil erodibility.

Table 6.3. Optimized Input data used in KINEROS2 model simulation.

Parameter	Value*
Average soil particle diameter (mm)	2.0
Bulk Density (g cm^{-3})	1.23
Plot length (m)	1.0
Plot width (m)	0.5
Slope (m m^{-1})	0.176, 0.268, and 0.364
Manning coefficient	0.04
Soil layer thickness (mm)	90
Saturated Hydraulic conductivity (mm h^{-1})	33.88
Porosity	0.49
Average topographic Relief (mm)	2.0
Saturation water content (m^3 m^{-3})	0.48

*The mean value for the optimized parameters of the calibration experiments

6.3. Results and Discussion

6.3.1. Runoff, sediment yield and drainage

Figure 6.2 shows the runoff, sediment yield, and drainage for the soil plot under 38 mm h^{-1} rainfall intensity and 10 degrees slope angle. The total values from the observed runoff, sediment yield and drainage at different runs were used in empirical and physically-based modeling.

Analysis of variance showed that the differences in D_i under different I and S was highly significant, $P<0.001$ and $P=0.003$; respectively. The interaction effect between I and S on D_i was also significant ($P=0.017$). The paired multiple comparison procedures showed that under low rainfall intensity there was no significant difference for D_i at different slopes angles. The effects of rainfall intensity were significant at all slope angles. The major processes on the interrill soil erosion are detachment due to raindrop impact and runoff transport. Therefore these processes are affected to a large extent by the magnitude of the rainfall intensity and slope gradient. The effect of rainfall intensity on the total runoff at different slope angles was significant ($P<0.001$), whereas the effect of slope on the sediment generation was not significant ($P=0.189$). The interaction effect between rainfall intensity and slope angles on the total runoff was also not significant ($P=0.055$). No significant effects of the I and S on the total drainage were observed.

The effect of rainfall intensity on sediment yield and runoff was significant at different slope angles, which is in agreement with one meter plot length results reported by Chaplot and Le Bissonnais (2003). The rainfall impact energy is an essential factor for soil detachment whereas the slope gradient seems to act as a detachment enhancer as demonstrated by the significant results achieved under the interaction between rainfall and slope angle. These results are in agreement with Sharma (1996). Under the Hortonian runoff conditions, the higher rainfall usually produces a higher amount of runoff, which is shown here as a significant effect of rainfall under different slope angles. However, the effect of the slope angle was not significant. This could be attributed to the great impact of the slope length under hillslope conditions in agreement with Chaplot and Le Bissonnais (2003) findings. The relationship of the infiltration rate with the slope angle and the rainfall intensities remains unclear although it has been studied by many researchers (Fox et. al., 1997).

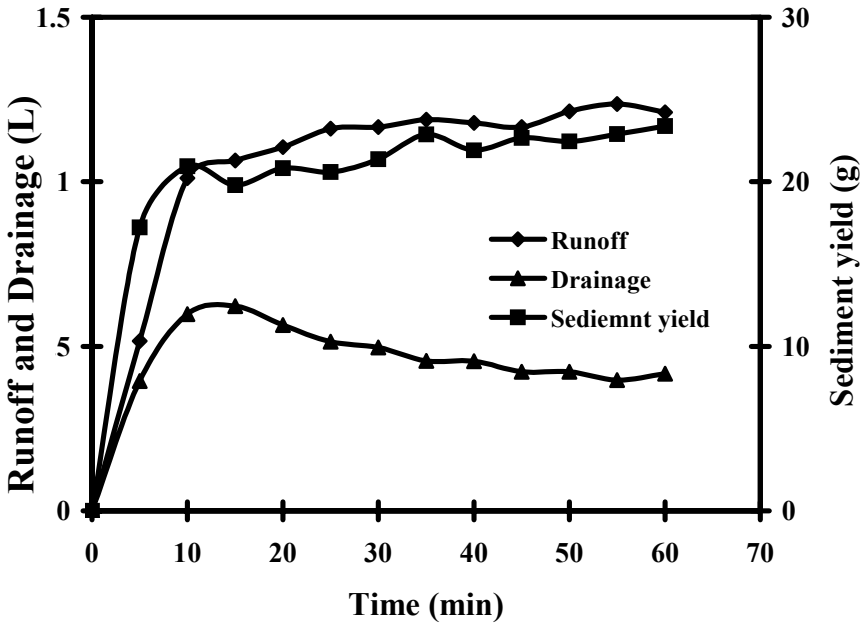

Fig. 6.2. Runoff, sediment yield, and drainage volume under: 38 mmh^{-1} rainfall intensity and 10 degrees slope angle.

6.3.2. Correlation analyses

Table 6.4 shows the correlation matrix between different hydrological components. A significant positive correlation exists between *I* and *Q* (r=0.87, P<0.001), D_i (r=0.75, P<0.001), and *Cs* (r=0.67, P=0.002). On the other hand, the total drainage was negatively correlated to *I* (r=-0.58, P=0.013).

No significant correlation existed between the *S* and *Q*, D_i, and *DR*. However, significant positive correlation existed between *S* and *Cs* (r=0.57, P=0.01).

The correlation between *Q* and D_i was significant (r=0.78, P<0.001), which indicated the high impact of surface runoff on sediment delivery **(Fig. 6.3)**. However, negative significant correlation existed between *Q* and *DR* (r=-0.59, P=0.009), and no significant correlation existed between *DR*, D_i, and *Cs*.

The rainfall intensity has a great influence on sediment generation, runoff and drainage. The sediment is mainly generated by raindrop impact and then transported by surface runoff, and hence the effect of rainfall intensity is stronger on soil loss than slope steepness (Zartl et al., 2001). The significant negative correlation between the rainfall intensity and drainage was also reported by Assouline and Ben-Hur (2006).

However, under wet soils the decrease in drainage could be attributed to the rainfall intensity and soil intake rate relationship rather than the soil sealing (crust) due to raindrop impact. This was statistically confirmed by the significant negative correlation between runoff and drainage.

The slope angle was insignificantly correlated to the sediment yield and the runoff, however, the sediment transport is usually enhanced by slope, which was emphasized by the significant correlation between slope angle and sediment concentration. This is in agreement with Sharma (1996: 125-152) and Chaplot and Le Bissonnais (2000).

6.3.3. Empirical modeling approach

6.3.3.1. Model development

Based on Neal (1938) and Sharma (1996: 125-152) models, a non-linear regression analysis was carried out to estimate the best parameters which fit the equation [1]. Equation [1] was fitted under two conditions: 1) linear effect of the rainfall factor (I) where the rainfall exponent (p) equal one (Kinnell, 1993); and 2) squared effect of the rainfall factor (I^2) where the rainfall exponent (p) equal two (Meyer, 1981).

Table 6.5 shows the models together with the different fitted parameters, R^2 and the significance level. The models from (1) to (6) were dependent on the rainfall factor and slope to determine the interrill sediment yield. The model with I^2 factor results had the better R^2 (0.77) for D_i prediction compared to the model using linear I factor, when I was used. However, the effective rainfall intensity (I_{eff}) predicted sediment yield better than I (R^2= 0.85). The exponent of I and S in model (5) and I_{eff} and S in model (6) were determined using non-linear regression **(Table 6.5)**. The R^2 at different rainfall conditions was higher in models (5) and (6), where the rainfall intensity exponent was fitted, compared to models 1-4. However in model (5), the rainfall intensity (I) exponent was greater than two, which is acceptable according to Kinnell (1993) who indicated that I^2 is entirely empirical.

The sediment yield varied directly with the I-linear where the model depends mainly on I and S. However, in cases where the runoff factor was considered the I-linear presented better R^2 (0.96), which is in agreement with the results of Kinnell (1993). Moreover, fitting all exponents gave better R^2 and I exponent was less than one whereas S exponent for all models was about 1.2.

Table 6.4. Correlation coefficients and the *P*-values for the main hydrological components

	Intensity (*I*)	**Slope (*S*)**	**Runoff (*Q*)**	**Drainage (*DR*)**	**Sediment yield (D_i)**	**Sediment concentration (*Cs*)**
(*I*)	1.0	-	$0.87^{(<0.001)}$	$-0.58^{(0.013)}$	$0.75^{(<0.001)}$	$0.67^{(0.002)}$
(*S*)		1.0	$0.08^{(ns)}$	$-0.21^{(ns)}$	$0.44^{(ns)}$	$0.57^{(0.01)}$
(*Q*)			1.0	$-0.59^{(<0.009)}$	$0.78^{(<0.001)}$	$0.72^{(<0.001)}$
(*DR*)				1.0	$-0.37^{(ns)}$	$-0.41^{(ns)}$
(D_i)					1.0	$0.98^{(<0.001)}$
(*Cs*)						1.0

ns: not significant.

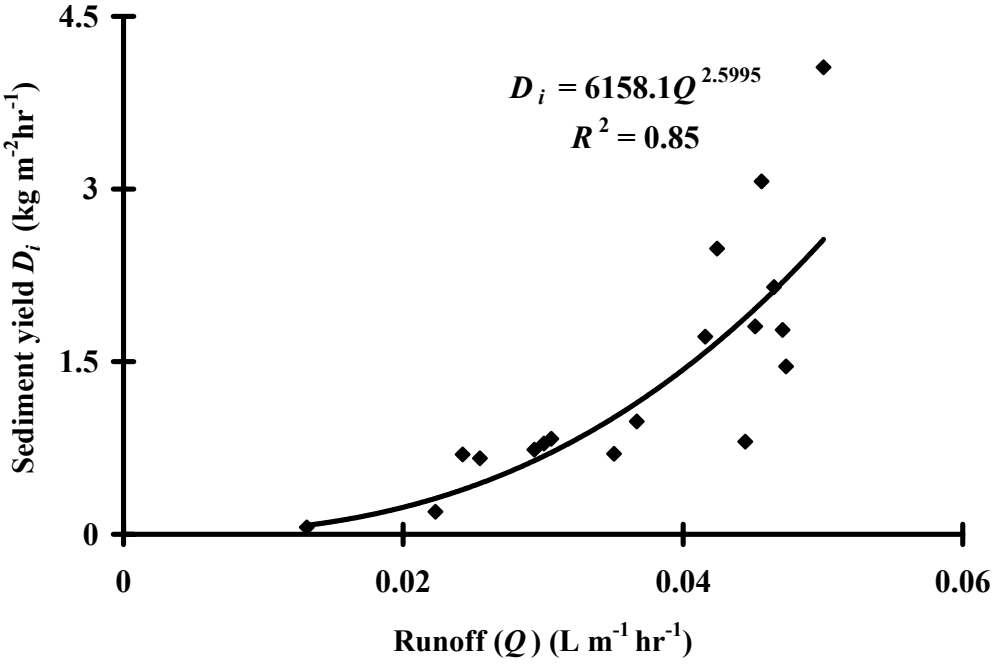

Fig. 6.3. Relationship between Sediment yield (D_i) and runoff (Q).

Table 6.5. Fitted empirical models for soil loss estimation.

	Model	Fitted Parameters	R^2	P-value	Remarks
(1)	$D_i = K_i I^a S^b$	b=1.19	0.53	<0.001	I-Linear
(2)	$D_i = K_i I^a S^b$	b=1.22	0.77	<0.001	I^2
(3)	$D_i = K_i I_{eff}^a S^b$	b=1.20	0.85	<0.001	I-linear
(4)	$D_i = K_i I_{eff}^a S^b$	b=1.28	0.84	<0.001	I^2
(5)	$D_i = K_i I^a S^b$	a= 3.45 b=1.26	0.85	<0.001	Fit I exponent
(6)	$D_i = K_i I_{eff}^a S^b$	a= 1.39 b=1.24	0.87	<0.001	Fit I exponent
(7)	$D_i = K_i I S^b q^c$	b=1.22 c= 2.21	0.96	<0.001	Linear I
(8)	$D_i = K_i I^2 S^b q^c$	b= 1.23 c= 1.67	0.94	<0.001	I^2
(9)	$D_i = K_i I^a S^b q^c$	a= 0.28 b= 1.21 c= 2.68	0.96	<0.001	Fit a, b and c

I_{eff} effective rainfall for the surface runoff (rainfall volume-drainage volume); a, b, and c exponents of the rainfall, slope, and runoff; respectively; K_i: soil erodibility.

6.3.3.2. Models validation

The models (2), (5) and (7) were validated by comparing the scaling factor of these models with data generated from similar laboratory experiments and model developed by Jayawardena and Rezaur (1998). **Figures 6.4**, **6.5**, and **6.6** show the validation of model (2), (5) and (7), where R^2 were 0.80, 0.89 and 0.96; respectively. Model (7) shows significant estimation for the sediment yield compared to models developed by Jayawardena and Rezaur (1998).

The runoff factor has a great impact on the prediction of sediment yield in interrill area. This could be attributed to the role of the surface runoff in sediment transportation rather than soil detachment in interrill areas. The linear rainfall factor was better at estimating the sediment generation than I^2 factor when the runoff factor in the model was considered which is in agreement with Kinnell (1993) and Jayawardena and Rezaur (1998).

The models described in **Table (6.2)** were used to simulate the sediment yield in the interrill area and compare it with measured sediment yield. **Figure 6.7** shows the relationship between the measured sediment yield and simulated sediment yield using the Jayawardena and Rezaur (1998) empirical model, which was estimated the sediment yield significantly (R^2= 0.90). **Figure 6.8** shows the relationship between the measured

and simulated sediment concentrations by the Huange (1995) quadratic model **(Table 6.2)**. These models significantly estimated the sediment yield and concentration from the interrill area; the runoff factor improved the accuracy of the estimate of these models which is in agreement with Huange (1995).

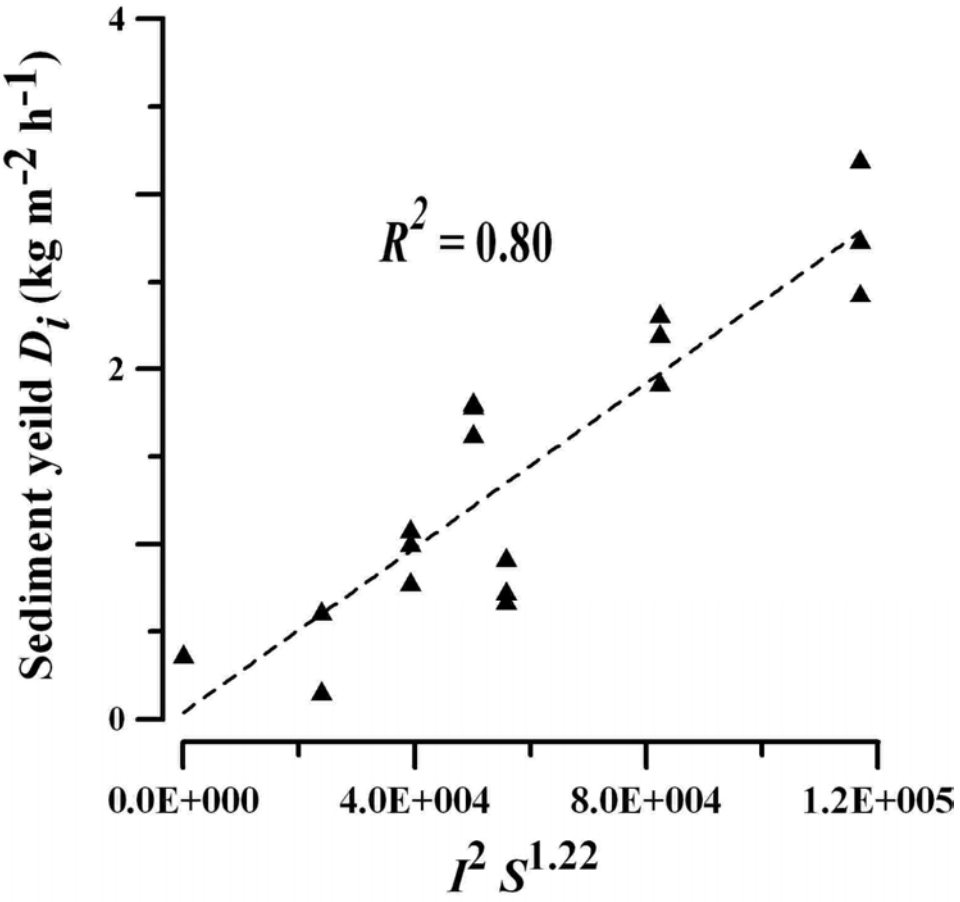

Fig. 6.4. Validation of Model (2) scaling factor using Jayawardena and Rezaur (1998) model.

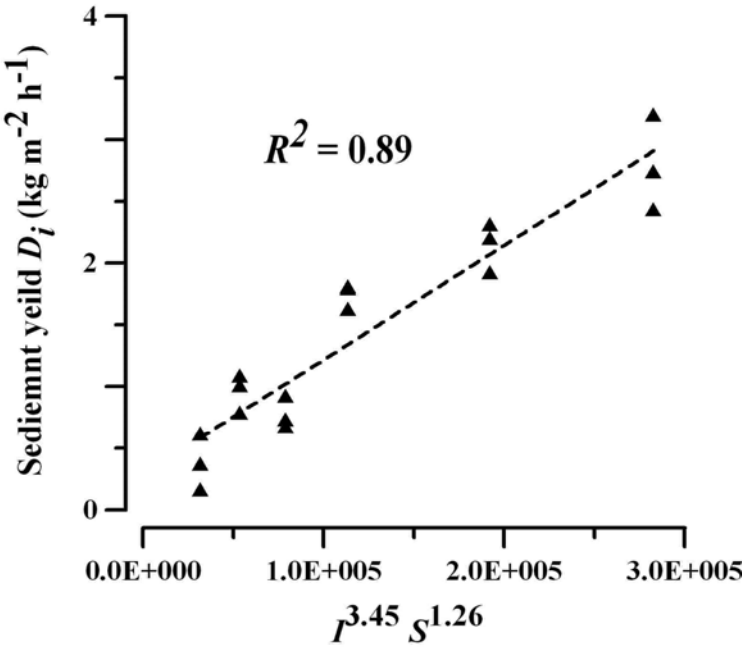

Fig. 6.5. Validation of Model (5) scaling factor using Jayawardena and Rezaur (1998) model.

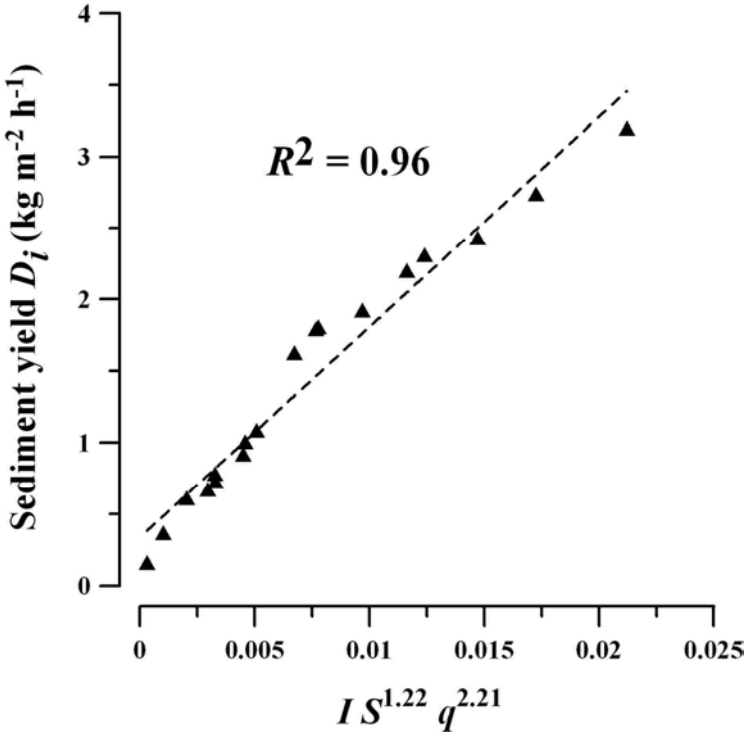

Fig. 6.6. Validation of Model (7) scaling factor using Jayawardena and Rezaur (1998) model.

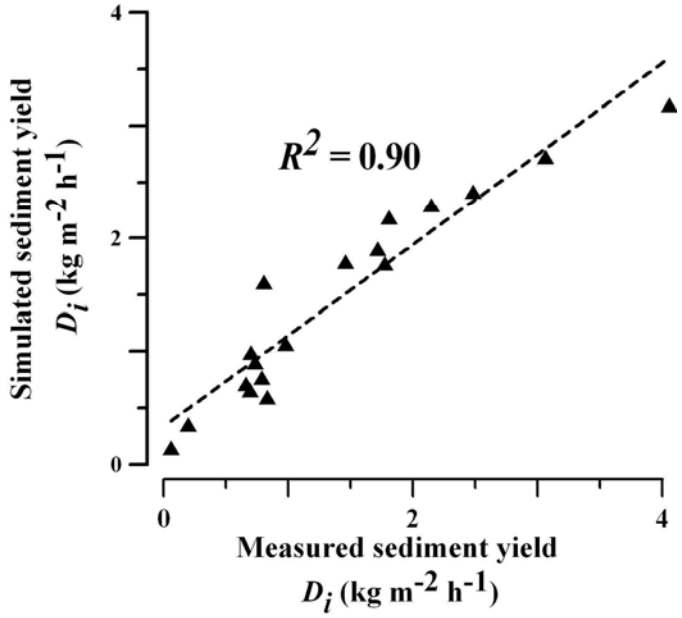

Fig. 6.7. Estimation of the sediment yield using Jayawardena and Rezaur (1998) model.

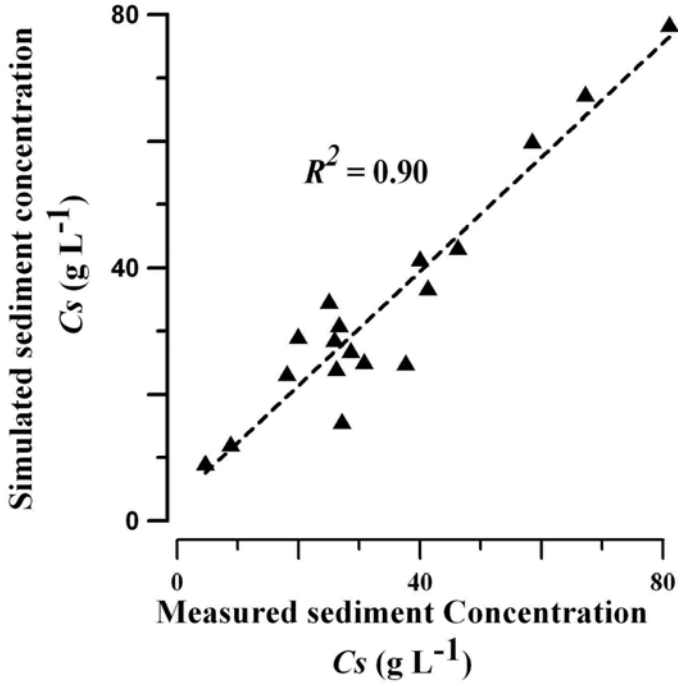

Fig. 6.8. Estimation of sediment concentration using quadratic polynomial model by Huange (1995).

6.3.4. Physically-based modeling

Table 6.6 shows the total sediment yield and runoff simulated using the plane module in KINEROS2 model compared with the measured components. There were no significant differences between the simulated and observed total runoff pairs at different rainfall intensity and slope angle combinations. The simulated runoff and sediment yield were highly correlated to the observed components; r=094 (P<0.001), whereas for the sediment yield the correlation coefficient was 0.89 (P<0.001). **Figure 6.9** shows the simulated and the observed sediment yields at different rainfall intensities and slope angles. The parameters for one replicate of each treatment were optimized in order to achieve the best-fit results and the same parameters were used in the other replicates. The optimization procedure showed that the simulated sediment yields were affected highly by changes in the soil bulk density and the saturated hydraulic conductivity. The average values of the optimized bulk density and hydraulic conductivity were 1.23 g cm^{-3} and 33.88 mm h^{-1}, respectively **(Table 6.7)**.

There was a high variation in the optimized parameters under different experimental conditions. These variations can be attributed to two reasons: first, the temporal changes of these parameters during rainfall simulation, and second, the difficulties in describing the entire interrill sediment generation processes physically, as reported by Jayawardena and Bhuyan (1999).

6.3.5. Comparison between the two approaches

The empirical models developed in this study significantly estimated the sediment yield. In these models, rainfall intensity, slope angle and runoff were used as the prediction factors (physically measured), whereas the soil erodibility was statistically generated from the non-linear regression analysis. Models developed by statistical methods are generally reliable, simple and easy to calibrate (Jayawardena and Rezaur, 1998). However, the parameters of the empirical modeling approach do not describe any physical properties of the soil, unlike the physically-based model.

The physically-based models have been developed to describe processes of detachment, deposition, and transportation by raindrop impact and runoff in mathematical formulas. Huange (1995) criticized the complex and sophisticated equations used in the physically-based models and the lack of data required to validate the growth of parameters used in those models. However, the advantage of physically-based models is that most of the input parameters are measurable soil properties **(Table**

6.3). Admittedly, these models require large amounts of input related to climatic, topographic, hydraulic, and soil properties data.

The soil erodibility used in the empirical modeling approach is still an undefined quantity, and all the trials to link the soil erodibility to some measures of soil properties failed (Kinnell, 1993). However, some parameters required by the physically-based models are difficult to collect from the field and also include some non-physical formulations (Aksoy and Kavas, 2005). Empirical analysis in erosion prediction is important, particularly for hillslope areas where information suitable for physically-based modeling is not readily available.

Huange (1995) stated that in order to insure reasonable prediction for soil erosion using the empirical model or the physically-based model there is a need for analytical validation of the former model and revision of the latter.

Table 6.6. Simulated interrill sediment yield and runoff using KINEROS2 and empirical models compared with the total observed runoff and sediment yield.

	$Q_{(obs)}$ (L $m^{-1}h^{-1}$)	$D_{i(obs)}$ (kg m^{-2} h^{-1})	$Q_{(KINEROS2)}$ (L m^{-1} h^{-1})	$D_{i(KINEROS2)}$ (kg $m^{-2}h^{-1}$)	$D_{i(KINNELL)}$ (kg m^{-2} h^{-1})	$D_{i(JAYA)}$ (kg m^{-2} h^{-1})	$D_{i(HUANGE)}$ (kg$m^{-2}h^{-1}$)
38/10[(a)]	0.026	0.514	0.023	0.058	0.560	0.481	0.484
38/15	0.036	0.841	0.029	0.820	1.139	1.033	1.110
38/20	0.027	0.698	0.023	0.695	1.161	0.802	0.876
55/10	0.046	1.291	0.051	1.508	1.403	1.714	1.187
55/15	0.046	1.979	0.051	1.743	2.106	2.248	1.970
55/20	0.046	3.271	0.051	3.069	2.833	2.774	3.271
R^2			0.86	0.95	0.84	0.86	0.92
RMSE%			12.9	16.9	20.07	21.07	9.71
ME			0.67	0.94	0.90	0.90	0.97

[(a)] The first 2 digits stand for rainfall intensity (mm h^{-1}) and the second 2 digits stand for slope angle.
$Q_{(obs)}$: observed runoff; $D_{i(obs)}$: observed sediment yield; $Q_{(KINEROS2)}$ and $D_{i(KINEROS2)}$: runoff and sediment simulated by KINEROS2 model, respectively; $D_{i(KINNELL)}$; $D_{i(JAYA)}$, $D_{i(HUANGE)}$: sediment yield simulated by Kinnell, Jayawardena and Rezaur, and Huange model, respectively

The empirical models were compared with KINEROS2 **(Table 6.6)**. The models performance was measured using three indices; the coefficient of determination (R^2), the root mean square errors (*RMSE*), and the model efficiency (*ME*). The empirical models do not estimate the total runoff explicitly, although there are several empirical relations developed to estimate the total runoff. The *RMSE* for estimated sediment yield by KINEROS2 (physically-based model) was 16.9%. Corresponding values for RMSE in Kinnell, and Jayawardena and Rezaur models (empirical models) were 20.1% and

21.1%, respectively. The *ME* values for the above models were 0.94, 0.90, and 0.90, respectively.

These results show that the physically-based model performed better than the empirical model when a single parameter (K_i) was used to estimate the sediment yield. However, Huange (1995) used three fitted parameters to estimate the sediment yield, which indicated R^2 (adjusted) equal to 0.92 (P<0.001), *RMSE* equal to 9.71%, *ME* equal to 0.97. In our study, the empirical models overestimated the total sediment yield compared with the physically-based model **(Fig. 6.9)**.

Table 6.7 shows the soil erodibility (K_i) used in the empirical models compared with the optimized soil hydraulic conductivity (K_s) and bulk density (ρ_b). However, no relationships were found between the K_i, K_s, and ρ_b, which emphasizes that no single parameter can describe lumped parameters of K_i.

Table 6.7. Soil erodibility, hydraulic conductivity, and bulk density optimized under different rainfall intensities and slope angles.

		K_i (Kinnell model)	K_i (Jayawardena and Rezaur model)	K_s (mm h^{-1})	ρ_b (g cm^{-3})
Total		0.06	1.16	33.88	1.23
Rainfall (mm h^{-1})	38	0.04	1.04	33.75	1.24
	55	0.06	1.16	34.00	1.21
Slope (degree)	10	0.05	0.91	37.00	1.19
	15	0.05	1.01	31.50	1.24
	20	0.06	1.33	33.13	1.25
Mean		0.05	1.10	33.88	1.23
SD		0.01	0.15	1.79	0.02

K_i (Kinnell model) *and* K_i (Jayawardena and Rezaur model)*:* soil erodibility estimated from Kinnell model, and Jayawardana and Razaur model, respectively*;* K_s*:* hydraulic conductivity*;* ρ_b: soil bulk density *SD*: standard deviation

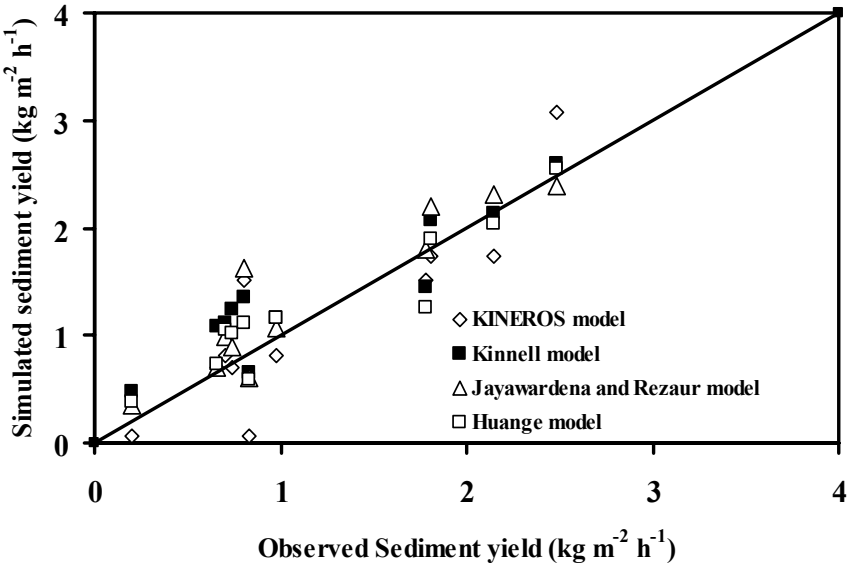

Fig. 6.9. Observed and simulated interrill sediment yields using empirical models and physically-based KINEROS2 model.

6.4. Conclusions

In this study two modeling approaches were evaluated to simulate the hillslope interrill sediment generation. Both the empirical and physically-based modeling approaches were capable, of simulating to simulate the interrill sediment generation significantly with some advantages and disadvantages for each approach. The empirical modeling approach is a simple and reliable method for interrill sediment prediction. However, the erodibility parameters (K_i) in these models are not measurable, and vary in space and time, which increases the model uncertainty. On the other hand, physically-based models require high number of input data sets related to climate and soil, which can be one of the barriers for the application of such models.

The physically-based model performed better than the empirical models in the total sediment yield estimation; R^2 was 0.95 compared with 0.84 and 0.86 for Kinnell, and Jayawardena and Rezaur models, respectively.

The presented results emphasize the capability of two different approaches, empirical and physically-based, to estimate the sediment generation from hillslope interrill areas. These models can be applied to the bare field soil under steep slopes ranging from 17% to 36%. However, certain consideration must be given to soil parameters. These include soil erodibility in the empirical model. It is still a question how it should be linked with the soil physical properties, such as soil bulk density and hydraulic conductivity.

CHAPTER 7:
General Conclusions

The rainfall impact energy represents the major cause of sediment detachment and soil microtopography changes occurred under interrill areas. A laboratory rainfall simulator was used to generate rainfall with different rainfall intensities. The simulated rainfall produced by dripper-type rainfall simulator was characterized using piezoelectric transducers. The rainfall kinetic energy (*KE*) showed significant association with the rainfall drop size distribution (*DSD*). The direct measured *KE* was significantly correlated with the estimated *KE* using the *DSD* and empirical fall velocity relationships. This result emphasizes the potential use of piezoelectric sensor to measure the rainfall characteristics and evaluate the rainfall impact energy. The rainfall characteristics showed that the dripper-type rainfall simulator produced a wide-spectrum of rainfall drop size similar to that found in natural rainfall, and this spectrum was changed with the rainfall intensity. However, the relationship between the erosivity indices and the rainfall intensity was unique and differed from natural rainfall relationships. The kinetic energy tended to increase with the rainfall intensity until 30 mm h^{-1} and started to decrease under the rainfall intensities higher than 30 mm h^{-1}. The phase-I exhibited a trend similar to the dominant reported trends of natural rainfall. The results suggested that the dripper-type rainfall simulator has a threshold limit. This threshold must be considered in order to simulate rainfall similar to natural rainfall. Also the D_s-I relationship was highly dependent on the relationship between the rainfall erosivity and the rainfall intensity, which could vary due to rainfall simulator type and generate different results which sometimes contradict trends depending on the rainfall characteristics. Regardless the rainfall intensity, the soil splash was found to be highly correlated with the erosivity indices, regardless of the rainfall intensity. In this regard, the erosivity indices (Kinetic energy and momentum) can be used effectively as independent soil splash predictors regardless of the rainfall intensity.

Most of the previous studies defined the soil microtopography as a constant factor. The photogrammetry was suggested as a tool to quantify the soil microtopography. The potential use of close-range photogrammetry and consumer-grade cameras in soil microtopography quantification were assessed. The first study explored the potential of using consumer-grade cameras in order to quantify a gypsum surfaces simulating the

soil surface under different roughness conditions. The generated DEMs accuracy was validated visually and numerically. The visual interpretation for the DEMs showed high similarity between the surfaces generated from the photogrammetry, and the surfaces generated from the pin-microrelief meter and the 2D images. Numerically, the elevation root mean square error was less than 1.0 mm. Also, the soil roughness indices, depression area percentage, depression storage capacity, micro-rills delineation obtained from the DEM generated by the photogrammetry were well correlated to the DEM generated from the pin-microrelief. However, all the differences could be attributed to the high sampling density of the photogrammetry. The close-range photogrammetry system using a consumer-grade camera showed high potential in quantifying the gypsum surfaces, which were used to simulate soil microtopography with different roughness conditions, compared with direct measurement using pin-microrelief meter.

The changes during the rainfall are also important for the runoff initiation and sediment flow. A completely automated fixed cameras-base photogrammetry system was used in order to acquire the temporal microtopography images. In this study advanced tools for the generation of rectified DEM were tackled to monitor the soil microtopography changes under rainfall. Prior to interpolation, the DEM errors were eliminated using the reference surface method, which was developed as a part of this study. The parametric statistical method was used to rectify the DEM errors after interpolation using a short FORTRAN program. The proposed two methods in this study can help to generate rectified DEM provided that the raw DEM has acceptable accuracy. The methods can be used for further studies related to clod breakdown by rainfall or by the effect of tillage implements, rill initiation and sediment quantification.

The modeling of sediment generation under various rainfall intensities and hillsope conditions are important. In this regard, the performance of two major modeling approaches was investigated using data generated from rainfall simulator experiments. In this study, two modeling approaches were evaluated to simulate the hillslope interrill sediment generation; the empirical and physically-based modeling. The two approaches were capable to simulate the interrill sediment generation significantly with some advantages and disadvantages for each approach. The empirical modeling approach is a simple and reliable method for interrill sediment prediction. However, the erodibility parameters (K_i) in these models are not measurable, and vary in space and time, which increases the model uncertainty. The physically-based model performed better than the

empirical models in the total sediment yield estimation; R^2 was 0.95 compared to 0.84 obtained by the empirical modeling approaches.

The presented results emphasize the capability of two different approaches, empirical and physically-based models, to estimate the sediment generation from hillslope interrill areas. These models can be applied to bare field soil under steep slopes ranging from 17 to 36 percent. However, a certain consideration should be applied to soil parameters. These include soil erodibility in the empirical model. It is still a question how it should be linked with the soil physical properties, such as soil bulk density and hydraulic conductivity?

REFERENCES

Abd Elbasit, Mohamed A. M., 2006. Assessment of spatiotemporal dynamics of sediment generation process using digital elevation model, Master Thesis, Tottori University; 115.

Abendini MJ, Dickinson WT, Rudra RP. 2006. On depressional storage: The effect of DEM spatial resolution. *Journal of Hydrology* **318**: 138–150

Aksoy H, Kavvas ML. 2005. A review of hillslope and watershed scale erosion and sediment transport models. *Catena,* **64**: 247-271.

Al-Durrah MM, Bradford JM. 1982. The mechanism of raindrop splash on soil surfaces. *Soil Science Society of America Journal* **46**: 1086-1090.

Allmaras RR, Burwell RE, Larson WE, Holt RF. 1966. *Total porosity and random roughness of the interrow zone as influenced by tillage. In* USDA, Conservation Research Report no. 7. US Government Printing Office, Washington, Dc. pp. 1-22.

Andrew PM, Mosher PN. 1968. Detachment of soil particles in simulated rainfall. *Soil Science Society of America Journal* **32**: 716-719.

Arvidsson J, Bölenius E. 2006. Effect of soil water content during primary tillage- laser measurements of soil surface changes. *Soil and Tillage Research* **90**: 222-229.

Assouline S. Ben-Hur M. 2006. Effect of rainfall intensity and slope gradient on dynamics of interrill erosion during soil surface sealing. *Catena,* **66**: 211-220.

Atlas D, Ulbrich CW. 1977. Path-and area integrated rainfall measurement by microwave attenuation in the 1–3 cm band. *Journal of Applied Meteorology* **16**: 1322–1331.

Beard KV, Pruppacher HR. 1969. A determination of the terminal velocity and drag of small water drops by means of wind tunnel. *Journal of the Atmospheric Sciences* **26**: 1066-1072.

Beard KV. 1976. Terminal velocity and shape of cloud and precipitation drops aloft. *Journal of Atmospheric Science* **33**: 851-864.

Bennett J.P. 1974. Concepts of mathematical modeling of sediment yield. *Water Resources Research,* **10**:485-492.

Bentley, Wilson A. 1904. Studies of raindrops and raindrop phenomena. *Monthly Weather Review* **32**: 450-456.

Bradford JM, Huange C. 1993. Comparison of interrill soil loss for laboratory and field procedures. *Soil Technology* **6**: 145-156.

Burrough PA, McDonnell RA. 1998. Principles of Geographical Information Systems. Oxford University Press: Oxford; 356.

Burwell RE, Allmaras RR, Amemiya M. 1963. A field measurements of total porosity and surface microrelief of soils. *Soil Science Society of America Proceeding* **33**: 697-700.

Butler, JB, Lane SN, Chandler JH. 1998. Assessment of DEM quality for characterizing surface roughness using close range digital photogrammetry. *The Photogrammetric Record* **16**(92): 271-291.

Campos E. 1999. On measurements of drop size distributions. *Tropical Meteorology and Oceanography* **6**(1): 24-30.

Chandler J. 1999. Effective application of automated digital photogrammetry for geomorphological research. *Earth Surface Processes and Land Form* **24**: 51-63.

Chaplot VAM, Le Bissonnais Y. 2003. Runoff features for interrill erosion at different rainfall intensities, slope lengths and gradient in an agricultural loessial hillslope. *Soil Science Society of America Journal,* **67**: 844-851.

Clarke MA, Walsh RPD. 2007. A portable rainfall simulator for field assessment of splash and slopewash in remote locations. *Earth Surface Processes and Landforms* **32**: 2052-2069.

Conrad O. 1998. GiGeM-software for digital elevation model. PhD thesis (in Germany), University of Göttingen: Germany.

Cressie N. 1993. Statistic for Spatial Data. Wiley: New York; 900.

Darboux F, Gasuel-Odoux C, Davy P. 2002. Effect of surface water storage by soil roughness on overland-flow generation. *Earth Surface Processes and Landform* **27**, 223-233.

Darboux F, Huang C. 2005. Does soil surface roughness increase or decrease water and particle transfer? *Soil Science Society of America Journal* **69**: 748-756.

Dimoyiannis D, Valmis S, Danalatos NG. 2006. Interrill erosion on cultivated Greek soils: modeling sediment delivery. *Earth Surface Processes and Landforms,* **31**: 940-949.

Ellison WD. 1947. Soil erosion studies. Part I. Agricultural Engineering **28**: 145-146.

El-Swaify SA. 1994. State-of-the-art for assessing soil and water conservation needs. P 13-27, *In*: TL. Napeir, SM. Camboni, SA. El-Swaify eds., *Adopting Conservation on the farm*. Soil and Water Conservation Society, Ankeny, IA.

FAO 1994. Land degradation in south Asia: Its severity, causes and effects upon the people. World soil resources reports, Rome.

Flicísimo AM. 1994. Parametric statistical method for error detection in digital elevation model. *ISPRS Journal of Photogrammetry and Remote Sensing* **49** (4): 29-33

Förster J, Gust G, Stolte S. 2004. A piezoelectrical rain gauge for application on buoys. *Journal of Atmospheric and Oceanic Technology* **21**: 179-193.

Foster GR. 1982. Modeling the erosion process. In *Hydrologic Modeling of Small Watershed*, CT Haan (ed). ASAE Monograph No. 5, Michigan; 297-379.

Foster IDL, Fullen MA, Brandsma RT, Chapman AS. 2000. Drip-screen rainfall simulators for hydro-and pedo-geomorphologyical research: The Coventry experience. *Earth Surface Processes and Landforms* **25**: 691-707.

Fox NI. 2004. The presentation of rainfall drop-size distribution and kinetic energy. *Hydrology and Earth System Sciences* **8**(5): 1001-1007.

Fox DM, Bryan RB, Price AG. 1997. The influence of slope angle on final infiltration rate for interrill conditions. *Geoderma,* **80**: 181-194.

Gantzer CJ, Alberts EE, Benntt WH. 1985. An electronic discriminator to eliminate the problem of horizontal raindrop drift. *Soil Science Society American Journal* **49**: 211-215.

Gee GW, Bauder JW. 1986. Particle-size analysis. *In* Klute A. ed., *Methods of soil analysis: Part 1 physical and mineralogical method*. American Society of Agronomy and Soil Science Society of America. Madison, Wisconsin, USA.

Ghadiri H, Payne D. 1977. Raindrop impact stress and the breakdown of soil crumbs. *Journal of Soil Science* **28**: 247-258.

Ghadiri H, Rose CW. 1992. Modeling chemical transportation in soil: Natural and applied contaminants. Lewis Publisher, Florida: 217.

Gilley JE, Finkner SC. 1985. Estimating soil detachment caused by raindrop impact. *Transaction of the ASAE* **28**: 140-146.

Giménez R, Gover G. 2001. Interaction between bed roughness and flow hydraulics in eroding rills. *Water Resources Research* **37**(3): 791-799.

Giménez R, Gover G. 2001. Interaction between bed roughness and flow hydraulics in eroding rills. *Water Resources Research* **37**(3): 791-799.

Govers G, Takken I, Helming K. 2000. Soil roughness and overland flow. *Agronomei* **20**: 131-146.

Govers G. 1992. Relationship between discharge velocity and flow area for rills eroding loose, non-layered materials. *Earth Surface Processes and Landforms* **17**: 515-528.

Gunn R, Kinzer GD. 1949. Terminal velocity of water droplets in stagnant air. *Journal of Meteorology* **6**: 243-248.

Guzha AC. 2004. Effect of tillage on soil microrelief, surface depression storage and soil water storage. *Soil and Tillage Research* **76**: 105-114.

Hancock G, Willgoose G. 2001. The production of digital elevation models for experimental model landscapes. *Earth Surface Processes and Landform* **26**, 475-490.

Hansen B, Schjønning P, Sibbesen E. 1999. Roughness indices for estimation of depression storage capacity of tilled soil surfaces. *Soil and Tillage Research* **52**: 103-111.

Hansen B. 2000. Estimation of surface runoff and water-covered area during filling of surface microrelief depressions, *Hydrological Processes* **14**: 1235–1243

Helming K, Römkens MJM, Prasad SN. 1998. Surface roughness related processes of runoff and soil loss: a flume study. *Soil Science Society of America Journal* **62**: 243-250.

Helming K, Römkens MJM, Prasad SN. 1998. Surface roughness related processes of runoff and soil loss: a flume study. *Soil Science Society of America Journal* **62**: 243-250.

Helming K, Roth ChH, Wolf R, Diestel H. 1993. Characterization of rainfall–microrelief interactions with runoff using parameters derived from digital elevation models (DEM's). *Soil Technology* **6**: 273–286

Huang C, Bradford JM. 1990. Depressional storage for Markov-Gaussian surfaces. *Water Resources Research* **26**(9): 2235-2242.

Huang C, White EG, Thwaite EG, Bendeli A. 1988. A noncontact laser system for measuring soil surface topography. *Soil Science Society of America Journal* **52**: 350-355.

Huange C. 1995. Empirical analysis of slope and runoff for sediment delivery from interrill areas. *Soil Science Society of America Journal* **59**: 982-990.

Hudson NW. 1957. Erosion control research. Progress report on Henderson Research station. *Rhodesia Agricultural Journal* **54**: 297-323.

Hudson NW. 1963. Raindrop size distribution in high intensity storms. *Rhodesian Journal of Agricultural Research* **1**: 6-11.

Hudson NW. 1965. The influence of rainfall mechanics on soil erosion. MSc Thesis: Cape Town University, South Africa.

Jayawardena AW, Bhuyan RR. 1999. Evaluation of an interrill soil erosion model using laboratory catchment data. *Hydrological Processes* **13**: 89-100.

Jayawardena AW, Rezaur RB. 1998. Modeling interrill sediment delivery. Proceeding of the Seventh International Symposium on River Sedimentation. 16-18 December. Hong Kong.

Jayawardena AW, Rezaur RB. 2000. Measuring drop size distribution and kinetic energy of rainfall using a force transducer. *Hydrological Processes* **14**: 37-49.

Jeschke W. 1990. Digital close-range photogrammetry for surface measurement. *International Archive of Photogrammetry and Remote Sensing* **28**: 1058-1065.

Jester W, Klik A. 2005. Soil surface roughness measurement-methods, applicability, and surface representation. *Catena* **64**: 174-192.

Kamphorst EC, Jetten V, Guérif J, Pitkänen J, Iversen BV, Douglas JT, Paz A. 2000. Predicting depretional storage from soil surface roughness. *Soil Science Society of America Journal* **64**:1749-1758.

Kinnel PIA. 1993. Interrill erodibilities based on the rainfall intensity-flow discharge erosivity factor. *Australian Journal of Soil Research* **31**:319-332.

Kinnell PIA. 1974. Splash erosion; some observations on the splash cup technique. *Soil Science Society of American Journal* **45**: 153–155.

Kinnell PIA. 1987. Rainfall Energy in Eastern Australia: Intensity-kinetic energy relationship for Canberra, A.C.T. *Australian Journal of Soil Research* **25**: 547-553.

Kinnell PIA. 1988. The influence of flow discharge on sediment concentrations in raindrop induced flow transport. *Australian Journal of Soil Research* **26**: 575-582.

Kinnell PIA. 2005. Sediment transport by Medium to large drops impacting flows at subterminal velocity. *Soil Science Society of America Journal* **69**: 902-905.

Kuipers H. 1957. A reliefmeter for soil cultivation studies. *Netherlands Journal of Agricultural Sciences* **5**: 255-262.

Laflen JM, Roose EJ. 1998. Methodologies for assessment of soil degradation due to water erosion. In: Methods for assessment of soil degradation. Lal R, Blum W. H, Valentine C, Stewart BA. (eds.). CRC, Boca Raton, Florida.

Lascelles B, Favis-Mortlock D, Parsons T, Boardman J. 2002. Automated digital photogrammetry: A valuable tool for small-scale geomorphological research for the non-photogrammetrist? *Transaction in GIS* **6**(1): 5-15.

Laws JO, Parsons DA. 1943. Relation of raindrop size to intensity. *Transaction of American Geophysics Union* **24**: 452-460.

Laws JO, Parsons DA. 1943. The relation of raindrop size to intensity. *Transaction of American Geophysics Union* **24**: 452-460.

Liebenow, A.M., Elliot, W. J., Laflen, J. M and Kohl, K.D. 1990. Interrill erodibility: Collection and analysis of data from crop land soils. *Transaction of the ASABE,* **33**: 1882-1888.

Linden DR, Van Doren JrJ. 1986. Parameters for characterizing tillage-induced soil surface roughness. *Soil Science Society of America Journal* **50**: 1560-1565.

Lindsay JB, 2005. The Terrain Analysis System: a tool for hydro-geomorphic application. *Hydrological Processes* **19**: 1123–1130.

Madden LV, Wilson LL, Ntahimpera N. 1998. Calibration and evaluation of an electronic sensor for rainfall kinetic energy. *Phytopathology* **88**: 950-959.

Magunda MK, Larson WE, Linden DR, Nater EA. 1997. Changes in microrelief and their effects on infiltration and erosion during simulated rainfall. *Soil Technology.* 10: 57-67.

Marshall JS, Palmer WMcK. 1948. The distribution of raindrops with size. *Journal of Meteorology* **5**: 165-166.

Mayer LD, Wischmeier WH. 1969. Mathematical simulation of the process of soil erosion by water. *Transaction of the ASABE,* **12**: 754-758.

Mayer LD. 1981. How rainfall intensity affects interrill erosion. *Transaction of the ASABE,* **34**: 161-168.

Merritt WS, Letcher RA, Jakeman AJ. 2003. A review of erosion and sediment transport models. *Environmental Modeling & Software,* **18**: 761-799.

Moritani S, Yamamoto T, Andry H, Muraki H. 2006. Monitoring of soil erosion using digital camera under simulated rainfall. *Transactions of the Japanese Society of Irrigation, Drainage and Reclamation Engineering* **244**: 143-149. (in Japanese).

Moss AJ. 1988. Effect of flow velocity variation on rain-driven transportation and the role of rain impact in the movement of solids. *Australian Journal of Soil Research* **26**: 443-450.

Mouzai L, Bouhadef M. 2003. Water drop erosivity: effect on soil splash. *Journal of Hydraulic Research* **41**: 61-68.

Nanko K, Hotta N, Suzuki M. 2004. Assessing raindrop impact energy at the forest floor in a mature Japanese cypress plantation using continuous raindrop-sizing instruments. *Journal of Forest Research* **9**:157-164.

Nanko K, Mizugaki S, Onda Y. 2007. Estimation of soil detachment rates on the forest floor of an unmanaged Japanese cypress plantation based on field measurement of the throughfall drop sizes and velocities. *Catena* **72**: 348-361.

Nash JE, Sutcliffe JV. 1970. River flow forecasting through conceptual models. Part 1-A discussion of Principles. *Journal of Hydrology*, **10**(3): 282-290.

Neal JH. 1938. Effect of degree of slope and rainfall characteristics on runoff and soil erosion. *Journal of Agricultural Engineering Research,* **19**: 213-217.

Nearing MA, Bradford JM, Holtz RD. 1986. Measurement of force vs. time relations for waterdrop impact. *Soil Science Society of America Journal* **50**: 1532-1536.

Nearing MA, Foster GR, Lane LJ, Finkner SC. 1989. A process-based soil erosion model for UDA-water Erosion Prediction Project technology. *Transaction of the ASABE,* **32**: 1587-1593.

Onstad CA, Wolf ML, Larson, CL, Slack DC. 1984. Tilled soil subsidence during repeated wetting. *Transaction of ASAE* **27**: 733-736.

Park SW, Mitchell JK, Bubenzer GD. 1982. Splash erosion modeling: Physical analysis. *Transaction of ASAE* **25**: 357-361.

Pidwirny M, Draggan S. 2008. Soil erosion and deposition. In Encyclopedia of Earth, CJ Cleveland (Ed). http://www.oearth.org/article/soil_erosion_and_deposition (Access: Nov. 19. 2008).

Planchon O, Darboux F. 2001. A fast, simple and versatile algorithm to fill the depressions of digital elevation models. *Catena* **46**: 159–176.

Poesen J, Torri D. 1988. The effect of cup size on splash detachment and transport measurement. I: Field measurements. Catena Supplement **12**: 113-126.

Pohjola H, Konkola L, Hoikkanen M, Schultz DM. 2008. Adjusting radar-derived QPE with measured drop-size distribution at the surface. *The fifth European conference on radar in meteorology and hydrology*. Helsinki, Finland.

Ravolonantenaia A H. 2004. Soil Erosion by Water Using Photogrammetry-Monitoring Systems, Master abstracts, Tottori University; 4.

Rieke-Zapp D, Nearing MA. 2005. Digital close range photogrammetry for measurement of soil erosion. *The Photogrammetric Record* **20** (109): 69-87.

Riezebos HTH, Epema GF. 1985. Drop shape and erosivity part Π: Splash detachment, transport and erosivity indices. *Earth Surface Processes and Landforms* **10**: 69-74.

Römkens MJM, Helming K, Prasad SN. 2001. Soil erosion under different rainfall intensities, surface roughness, and soil water regimes. *Catena* **46**: 103-123.

Saleh A. 1993. Soil roughness measurement: chain method. *Journal of Soil and Water Conservation* **48**: 527-529.

Salles C, Poesen J, Borselli L. 1999. Measurement of simulated drop size distribution with an optical spectro pluviometer: Sample size consideration. Earth Surface Processes and Landforms **24**: 545-556.

Salles C, Poesen J, Govers G. 2000. Statistical and physical analysis of soil detachment by raindrop impact: rain erosivity indices and threshold energy. *Water Resources Research* **36**: 2721-2729.

Salles C, Poesen J, Sempere-Torres D. 2002. Kinetic energy of rain and its functional relationship with intensity. *Journal of Hydrology* **257**: 256-270.

Salles C, Poesen J. 2000. Rain properties controlling soil splash detachment. *Hydrological Processes* **14**: 271-282.

Salmi A, Elomaa L. 2007. Measurement of the terminal velocity and shape of falling raindrops at Vaisala rain laboratory. *Eighth European conference on application of meteorology (ECAM)*, San Lorenzo de El Escorial, Spain.

Salmi A, Ikonen J. 2005. Piezoelectric precipitation sensor from Vaisala. *World Meteorology Organization technical conference on meteorological and environmental instruments and methods of observation (TECO 2005)*, Bucharest, Romania.

Sharifah Mastura SA, Sabry MA, Othman J. 2003. Rainsplash erosion: A case study in Tekala river catchment, East Selangor Malaysia. *Geografia* **1**: 44-59.

Sharma PP, Gupta SC. 1989. Sand detachment by single raindrops and varying kinetic energy and momentum. *Soil Science Society of America Journal* **55**: 1005-1010.

Sharma PP. 1996. Interrill erosion. *In*: Agassi M. ed., *Soil Erosion Conservation and Rehabilitation*, Marcel Dekker, New York.

Smith RE, Goodrich DC, Quinton JN. 1995. Dynamic distributed simulation of watershed erosion: The KINEROS2 and EUROSEM models. *Journal of Soil and Water Conservation*, **50**(5):517-520.

Steichen JM. 1984. Infiltration and random roughness of tilled and untilled claypan soil. *Soil and Tillage Research* **4**: 251-262.

Stojic M, Chandler P, Luce J. 1998. The assessment of sediment transport rates by automated digital photogrammetry. *Photogrammetry Engineering and Remote Sensing* **64**(5): 387-395.

Strahler AN. 1957. Quantitative analysis of watershed geomorphology. *Transaction of the American Geophysical Union* **38**: 913-920

Styczen M, Hogh-Schmidt M. 2002. Comment on "Statistical and physical analysis of soil detachment by raindrop impact: Rain erosivity indices and threshold energy" by C. Salles, J. Poesen, and G. Govers. *Water Resources Research* **38**: 1266.

Taconet O, Ciarletti V. 2007. Estimating soil roughness indices on ridge-and-furrow surface using stereo photogrammetry. *Soil and Tillage Research* **93**: 64-76.

UNEP 1992. Desertification, land degradation [definitions]. Desertification Control Bulletin 21.

United Nation Population Division (UNPD). 2004. World population 2300. United Nation, New York, 254.

Van Dijk AIJM, Bruijnzeel LA, Rosewell CJ. 2002. Rainfall intensity-kinetic energy relationship: a critical literature appraisal. *Journal of Hydrology* **261**: 1-23.

Vidal Vázquez E, Miranda JGV, Alves MC, Paz González A. 2006. Effect of tillage on fractal indices describing soil surface microrelief of Brazilian Alfisol. *Geoderma* **134**: 3006-317.

Wanger LE, Yu Y. 1991. Digitization of profile meter photographs. *Transaction of ASAE* **34**(2): 412-416.

Wesemael BV, Poesen J, Figueiredo TD, Govers G. 1996. Surface roughness evolution of soils containing rock fragments. *Earth Surface Processes and Landforms* **21**: 399-411.

Wischmeier WH, Smith DD. 1958. Rainfall energy and its relationship to soil loss. *Transaction of American Geophysics Union*. **39**: 285-291.

Wischmeier WH, Smith DD. 1965. Predicting rainfall-erosion losses from cropland east of the Rocky Mountains. Agricultural Handbook No. 282, US Department of Agriculture, Washington, DC.

Wischmeier WH, Smith DD. 1978. *Predicting rainfall erosion losses- A guide to conservation planning.* USDA Agricultural Hand Book 537. U.S. Government Printing Office, Washington, DC.

Woolard JW, Colby JD. 2002. Spatial characterization, resolution, and volumetric change of costal dune using airborne LIDAR: Cape Hatteras, North Carolina. *Geomorphology* **48**: 269-287

Yamamoto T, Otoshi M, Hikami H, Wen G, Inoue M, Uchida O. 2002. Use of Photogrammetry in monitoring soil erosion. *ASAE annual meeting*, paper No. 022089, Chicago, Illinois, USA.

Young RA, Wiersma JL. 1973. The role of raindrop impact in soil detachment and transport. *Water Resources Research* **9**: 1629-1636.

Zanchi C, Torri D. 1980. Evaluation of rainfall energy in central Italy. In *Assessment of Erosion*, De Boodt M, Gabriels D (eds). Wiley: Toronto; 133-142.

Zartl AS, Klik A, Huang C. 2001. Soil Detachment and transport processes from interrill and rill area. *Physics and Chemistry of the Earth (B),* **26** (1): 25-26.

Zingg AW. 1940. Degree and length of land slope as it affects soil loss in runoff. *Agricultural Engineering* **21**: 59-64.

JAPANESE ABSTRACT

論文要旨

雨滴による地面の変形は幾つかの過程を経過するが、それらの過程は十分には解明されていない。この研究では、2 つの重要な過程を観測し、評価して、モデル化を試みた。それらは、雨滴による微地形の動態と土粒子の剥離である。それらの過程に関与する要因を定量的に明確にするためには、幾つかの手法が必要になる。

最初に、人口降雨の雨滴エネルギーを測定するため、圧電性の変換器の使用可能性を調べた。圧電性の変換器を用いて、人口降雨の動的エネルギー（KE）と雨滴の粒径分布を測定した。この変換器は、バイサラ社の RAINCAP 降雨センサーの一部に手を加えたものである。KE の測定値と、雨滴の粒径分布と雨滴の落下速度の測定値に基づいた KE の推定値とは高い相関関係にあった。また、人口降雨装置による降雨特性と雨滴による土壌侵食（Ds）の関係を解明にした。とくに、降雨強度（I）と KE の関係は、自然降雨とは異なっていた。しかし、I-Ds の関係は、自然降雨と類似した傾向にあった。このことは、I-Ds の関係を決めるためには、I-KE の関係が重要であることを示唆している。なお、それらの関係は降雨によって異なる。人口降雨の雨滴による土壌侵食をより正確に推定するためには、人口降雨の降雨特性を考慮しなければならないことが明確になった。

次に、表面積が $1m^2$ 以下の人口土層を用いて、微地形を定量的に評価するため、一般的なカメラと近写写真測量手法の精度を確認した。まず、写真測量システム（PHM）を用いて地表面の数値標高モデル（DEM）を作成した。PHM で作成した DEM について、再現精度、地表面の粗度、窪地の面積割合、窪地の容積、微少なリルの再現性を評価した。それらには、一般的なカメラと微地形の直接測定器も用いた。その結果、一般的なカメラも近写写真測量手法も、高い精度で微地形を定量的に測定できることが明らかとなった。また、降雨による微地形の動態の定量的な測定の可能性も明らかとなった。また、内挿前に DEM の誤差を探して、少なくするため、参照修正手法を開発した。さらに、内挿後の DEM の誤差を探して、修正するため、変数統計手法を開発した。そこ結果、修正機能を持たせた自動数値写真測量手法によって、降雨中の三次元の微地形の動態を高い精度で再現できるようになった。

最後に、丘陵地の土壌堆積を推定するため、実験に基づいたモデルと物理モデルの可能性を評価した。実験に基づいたモデルには、土壌堆積に関与する要因の降雨強度、勾配および流出を用いた。物理モデルでは、流出を推定するため動的波形手法を用いた。また、堆積を推定するため物質収支式を用いた。これらの 2 つのモデルを比較した結果、土壌の仮比重と透水係数に基づいた物理モデルによって、流出と土壌堆積を効果的に推定できることが明らかとなった。

LIST OF RELATED PEER-REVIEWED PUBLICATIONS

1. Mohamed A. M. Abd Elbasit, Hiroshi Yasuda, Hisao Anyoji. Development and application of digital elevation model rectification method in monitoring soil microtopography changes during rainfall. *Journal of Japan Society of Hydrology and Water Resources* Vol. **21,** No. 1, 2008, P 114-125.

This paper partly covers **Chapter 5** in the thesis.

2. Mohamed A. M. Abd Elbasit, Hisao Anyoji, Hiroshi Yasuda, and Tadaomi Saito. Simulation of hillslope interrill sediment generation using two modeling approaches and simulated rainfall experimental data. *Journal of Arid Land Studies* Vol. **18, No.** 3, 2008, P 91-102.

This paper partly covers **Chapter 6** in the thesis.

3. Mohamed A. M. Abd Elbasit, Hisao Anyoji, Hiroshi Yasuda, Shunichi Yamamoto. Potential of low cost close-range photogrammetry in soil microtopography quantification. *Hydrological Processes* Vol. **23**, 2009, in press

This paper partly covers **Chapter 4 and 5** in the thesis.

4. Mohamed A. M. Abd Elbasit, Hiroshi Yasuda, Atte Salmi, Hisao Anyoji. Characterization of rainfall generated by dripper-type rainfall simulator using piezoelectric transducer and its impact on splash soil erosion. *Journal of Earth Surface Processes and Landforms.* (2008, under review).

This paper partly covers **Chapter 2 and 3** in the thesis.

LIST OF RELATED CONFERENCE PAPERS

1. Mohamed A. M. Abd Elbasit, H. Yasuda, A. Salmi, P. Kopsala, H. Anyoji. 2007. Characterization of rainfall generated by dripper-type rainfall simulator using piezoelectric transducer. Proceeding of the annual conference of Japan Society of Hydrology and Water Resources, Nagoya, Japan: July, 25th-27th.

2. Mohamed A. M. Abd Elbasit, H. Anyoji, H. Yasuda, T. Saito. 2007. Estimation of hillslope interrill soil erosion using empirical modeling approach. Annual meeting of The Japanese Society of Irrigation, Drainage and Reclamation Engineering. Matsue, Japan: August, 28th-30th.

3. Mohamed A. M. Abd Elbasit, H. Anyoji, H. Yasuda. 2008. Discrimination of intra-rainfall event soil microtopography changes using digital close-range photogrammetry. 5th annual meeting of Asia Oceania Geosciences Society. Busan, Korea: June, 16th -20th.

4. Mohamed A. M. Abd Elbasit, H. Yasuda, A. Salmi, H. Anyoji. 2008. Assessment of sediment generation and rainfall erosivity indices under dripper-type rainfall simulator using piezoelectric transducers. 5th annual meeting of Asia Oceania Geosciences Society. Busan, Korea: June, 16th -20th.

5. Mohamed A. M. Abd Elbasit, H. Yasuda, S. Yamamoto, H. Anyoji. 2008. Quantification of soil microtopography using customer-grade camera and digital close-range photogrammetry techniques. The 21st Congress, The International Society for Photogrammetry and Remote Sensing. Beijing, China: July, 3-11.

APPENDICES

The rainfall simulator

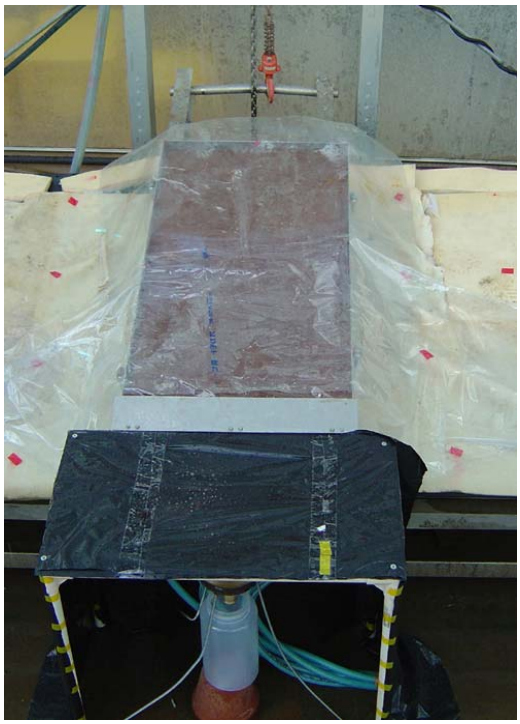

Soil plot before the rainfall simulation.

Runoff and drainage measurements.

Soil plot under rainfall simulation, kinetic energy and drop size distribution sensors, tipping-bucket rain gauge, and oblique-fixed camera photogrammetry system.

Natural rainfall characterization using piezoelectric transducers (Data under processing).